TECHNISCHE UNIVERSITÄT DRESDEN
INSTITUT FÜR WISSENSCHAFTLICHES RECHNEN

DISSERTATION

MULTI - PHASEFIELD MODELS FOR ACTIVE CELLULAR STRUCTURES

A thesis submitted in fulfillment of the requirements for the degree of

DOKTOR RERUM NATURALIUM (DR. RER. NAT.)

by

DENNIS WENZEL

born the 8th of February 1994 in Nordhausen.

Submission Date:	17th August 2021
Disputation Date:	29th October 2021
First Reviewer:	Professor Axel Voigt
Second Reviewer:	Assistant Professor Amin Doostmohammadi

Für meinen Großvater.

Danksagung

Mein gesamtes Leben und insbesondere die Erstellung dieser Arbeit, ist geprägt von einer Vielzahl wundervoller Menschen, die das alles überhaupt erst ermöglicht haben. Jedem einzelnen bin ich sehr dankbar und auch wenn ich nur einige wenige nennen kann an dieser Stelle, ließe sich diese Liste um ein Vielfaches erweitern.
Zu allererst möchte ich meiner wundervollen Partnerin Jessi danken, die in jeder Lebenslage meinen Fixpunkt darstellt und mein Leben mehr bereichert als ich es von einem einzelnen Menschen je für möglich gehalten hätte. Ich danke dir, dass du immer an meiner Seite stehst und mit mir durch jede kleine und große Frustration, auch während der Arbeit an dieser Dissertation, gegangen bist.
Meiner Familie bin ich dankbar, dass sie mich auf diesen Weg gebracht und mich immer unterstützt haben. Meine Eltern, Sabine und Fazlı, haben mir überhaupt erst ermöglicht, diesen einzuschlagen indem sie mich stets ermutigt haben, nach den Sternen zu greifen. Meine Schwester Lara Emilia, die mich immer auf den Boden zurückholt und mir zeigt, dass Familie wichtiger ist als alles andere. Und schließlich meine Großeltern, Inge und Karl-Heinz, die in jeder Sekunde meines Lebens so sehr an mich geglaubt haben, dass ich gar keine Wahl hatte als selbst ebenfalls an mich zu glauben. Weil du, Opa, die Abgabe dieser Arbeit nicht mehr erleben kannst, obwohl du stets einer meiner größten Fürsprecher warst, ist alles, was noch folgt, dir gewidmet.
Sozusagen meine zweite Familie sind all die anderen großartigen Menschen, die mir im Laufe des Lebens begegnet sind und die mich seitdem begleiten. Besonderen Dank schulde ich Joachim, denn einen wie dich gibt es kein zweites Mal auf dieser Welt. Um jedoch das Risiko, jemanden zu vergessen, zu vermeiden, möchte ich auf die vollständige Aufzählung an dieser Stelle verzichten und mich stattdessen darauf verlassen, dass ihr alle wisst, wie wichtig ihr für mich seid.
Natürlich ist dies eine wissenschaftliche Arbeit und so ist ganz klar, dass ich auch in diesem Bereich vielen Menschen Dank schulde. Vor allen anderen möchte ich meinem Betreuer und angehenden Doktorvater, Prof. Dr. Axel Voigt, danken, der diese Arbeit erst ermöglicht hat. Ich danke dir, dass du mich in dieses unglaublich spannende Feld eingeführt sowie mich dazu gebracht, aus jeder einzelnen Simulation das Beste herauszuholen und einen großen Beitrag zu meiner Entwicklung geleistet hast. Ein weiteres riesiges Danke gilt meinen beiden großartigen Masteranden. Harish, du hast mir als erstes klar gemacht, wie viel man gemeinsam erreichen kann, das allein nicht möglich wäre und mit deiner Hingabe etwas wundervolles geschaffen. Lea, du wirst immer die bessere Mathematikerin sein, wofür ich sehr dankbar bin, ebenso wie für jede Kaffeepause und jedes Gespräch. Außerdem möchte ich auch Cindy und Christine danken, denn ohne euch hätte ich vor lauter Papierkram und organisatorischen Hürden so wenig Zeit für die Forschung gehabt, dass diese Arbeit wohl noch Jahre brauchen würde. Auch hier möchte ich, wie schon zuvor, auf die weitere Auflistung verzichten, um niemanden zu vergessen und stattdessen ein riesiges Danke aussprechen an alle Mitglieder des Institutes für Wissenschaftliches Rechnen, denn die Zeit bei euch und mit euch war und ist eine großartige Erfahrung für mich.

Dresden, 11. August 2021

Acknowledgements

During my whole life and in particular the creation of this thesis, countless amazing people have accompanied me. None of this would have been possible without all of you. Please know that I am incredibly grateful to each and everyone of you, even though there is no way I can name you all at this point, otherwise the list would probably be longer than my thesis.
At first I want to thank my amazing girlfriend Jessi, who is my fixed point in every moment of my life. Never have I thought that a single person could improve every aspect of life this much. Thank you for always standing by my side and for being with me through every every bump in the road.
I a thankful to my family for bringing me on this way and supporting me at every step. My parents, Sabine and Fazlı, have made it possible for me to take this path by always encouraging me to reach for the stars. My sister, Lara Emilia, has consistently brought me back on the ground and shown me how family is the most important thing in life. Finally my grandparents, Inge and Karl-Heinz, had so much faith in me for every second of my life that I had no choice but to have faith in myself, too. Because you, grandfather, can not be with me for the end of this thesis, even though you were always one of my biggest supporters, everything that follows is dedicated to you.
My second family are all the amazing people I have met throughout my life and that keep me company ever since. Special gratitude is owed to Joachim because he is second to none. To avoid the risk of forgetting anyone, I will skip the full list at this point and rely on the fact that you all know how much you mean to me!
Of course this is a scientific work and so I owe gratitude to many people in this field, too. At first I want to thank my Ph.D. supervisor, Prof. Dr. Axel Voigt, who made this work possible in the first place. Thank you for introducing me to this exciting field, for encouraging me to make the best out out every single simulation and for your significant contribution to my personal development. Another big thanks goes to my amazing master students. Harish, you have shown me how much can be achieved together that would not be possible alone and you have created something beautiful with your devotion to our research. Lea, you will always be the better Mathematician than me, something I am very grateful for as much as I am grateful for every coffee break and every conversation. Furthermore, I want to thank Cindy and Christine, because without you the organization and paperwork would have taken so much of my research time that this thesis would have taken many years longer. At this point again, I want to skip the full list in order to avoid forgetting someone and instead say a huge thank you to all members of the Institute of Scientific Computing because the time with you was and still is a great experience.

Dresden, 11th of August 2021

Contents

TECHNISCHE UNIVERSITÄT DRESDEN
INSTITUT FÜR WISSENSCHAFTLICHES RECHNEN

ABSTRACT

MULTI - PHASEFIELD MODELS FOR ACTIVE CELLULAR STRUCTURES

by DENNIS WENZEL

After decades of experimental investigation, the dynamics how individual cells move or deform - perfectly orchestrated for the creation and proliferation of tissue - remain partly unknown. In most recent years, the use of computational models, also called *in silico* experiments, has become a focus of interest. Due to their flexible scaling, compared to classical *in vivo* and *in vitro* studies, simulations can give important insights in the dynamics of cellular structures.
We investigate Multi-Phasefield models for cellular structures, a versatile approach, capable of capturing complex changes in cell shape. Furthermore, it gives large flexibility in the modeling of cell-cell interactions and subcellular details like the propulsion machinery. The dynamics how these motility mechanisms create complex movement patterns on the tissue scale, will be a particular focus of this thesis. We compare four essentially different ways to introduce activity in Multi-Phasefield models, from movement driven by a random walk or the macroscopic shape of each cell towards a description of the subcellular machinery using either a polar or a nematic approach.
For the different propulsion models, we investigate a variety of phenomena. Starting from the observation that the polar model creates collective motion, we observe that the resulting alignments resemble those of passive systems, expressed in Lewis' and Aboav-Weaire's law. Furthermore, we study a transition between solid and liquid state of the tissue, known to be important for many developmental processes. Additionally, we analyze the occurring patterns in the cellular alignment and flow, for systems in both confluence and confinement. Afterwards, we investigate the alignment of cell deformations with methods known from nematic structures. This reveals how the different propulsion mechanisms cause contractile or extensile behavior, classified by the movement of topological defects and the distribution of strain in their vicinity.
At the end of this thesis, we show two extensions of the models, capable of including growth and division of cells and generalizations towards curved manifolds as computational domains. Furthermore, we give an outlook on a possible roadmap for the future of Multi-Phasefield models in the description of cellular structures and their potential for a better understanding of the dynamics in the creation of life.

List of Figures

1 | INTRODUCTION

> *It would mean bringing coals to Newcastle were I to describe here the immeasurable progress which biology in all its branches owes to the introduction of this concept of the cell concept. For this concept is the axis around which the whole of the modern science of life revolves.*
>
> PAUL EHRLICH
> NOBEL LECTURE 1908

The creation of life, from simple molecules to highly complex organisms like the human body, is a miraculous story and cells are some of the most crucial protagonists. Despite the enormous progress in the understanding of cellular creation and dynamics over the last decades, many questions are still open. The behavior of multicellular structures, for example the emergence of collective motion and the formation of highly complex alignments, resulting from the dynamics of individual cells, is a key to understanding some of the most important processes in modern biology and medicine, including embryogenesis, wound healing and cancer spreading.
In recent years, aside of experimental observations *in vivo* and *in vitro*, the concept of *in silico* studies has grown huge interest. A variety of mathematical models has been proposed, based on experimental observations, in order to improve the understanding of the physical processes at play. Due to the rapidly increasing computational resources available, the *in silico* models provide an easily scalable experimental approach, which is likely to gain even more importance in the future.
We focus on a specific class of models, the Multi-Phasefield description, which features a high level of detail and allows for complex shape changes on the cellular level. In particular, we investigate how certain features of the model affect the emerging behavior, in order to derive a deeper understanding on the dynamics in living tissue. One important aspect is the mechanism of activity, moving the individual cells in the structure as this is still not fully understood in experimental studies.

1.1 | THESIS STRUCTURE

The formulation of any mathematical model requires a solid groundwork. In Chapter 2, we will give a short recap of the required preliminaries for our models. In particular, we will review how evolution equations can be derived from energy descriptions and their desire to minimize. Furthermore, we introduce some fundamentals about Q-tensors and their applications in *liquid crystals* or other systems with nematic alignment structure.
Chapter 3 is purely devoted to the modeling aspect of the thesis. We will give a short review on other existing models and their up- and downsides and then assemble the Multi-Phasefield models piece by piece. In particular, we create a set of

modular 'components' - for example in the description of cell movement - that can be combined in different ways, depending on the particular setup.
Based on the modeling groundwork, we perform studies on the topological and geometrical arrangement of cells in Chapter 4. We investigate, for example, how it is possible to create coordinated movements in the simulated tissue, a phenomenon that is commonly known, for example in wound healing, and yet still not fully understood. Furthermore, we measure arrangements using Lewis' law and Aboav-Weaire's law, known to be fulfilled in passive systems and observed also in tissue structures.
Afterwards, in Chapter 5, we focus on different mechanisms of activity and how they lead to the generation of shape and flow. In particular, we investigate a transition between solid and liquid state which has been observed in different cellular structures, for example during body axis elongation in zebrafish embryos. Furthermore, we examine the occurrence of vortices in the flow of cells and even global oscillatory behavior, depending on the geometry.
Furthermore, we investigate the spatial ordering of cellular structures, resembling the behavior of nematic systems in Chapter 6. The groundwork for this is the derivation of a robust set of methods for detection and tracking of topological defects in these nematic alignments. Afterwards, we use these methods to investigate the creation and movement of these topological defects and analyze occurring patterns of the strain rate in their vicinity. The combination of these observations will classify the overall behavior of some of the models as contractile or extensile.
Finally, in Chapter 7, we draw conclusions and give a short review on two extensions, including colony growth and curved domains, that have been investigated in student research projects. We give an extensive outlook on the rich possibilities for this highly promising and yet still very new modeling approach.

1.2 | LITERATURE LIST

Most of the results in this thesis are published in international journals. We use this section to give an overview, which publications form the foundation of each chapter.

Chapter 3 - Model Derivation and Implementation

D. WENZEL, S. PRAETORIUS, and A. VOIGT. Topological and geometrical quantities in active cellular structures. In: *The Journal of Chemical Physics* 150 (2019), p. 164108

D. WENZEL and A. VOIGT. *Multiphase field models for collective cell migration*. 2021. arXiv: 2106.10552

Chapter 4 - Topological and Geometrical Quantities in Cellular Structures

D. WENZEL, S. PRAETORIUS, and A. VOIGT. Topological and geometrical quantities in active cellular structures. In: *The Journal of Chemical Physics* 150 (2019), p. 164108

Chapter 5 - Cellular Shape and Flow Driven by Activity

D. WENZEL and A. VOIGT. *Multiphase field models for collective cell migration*. 2021. arXiv: 2106.10552

Chapter 6 - Cellular Structures as Active Nematics

D. WENZEL et al. Defects in Active Nematics – Algorithms for Identification and Tracking. In: *Computational Methods in Applied Mathematics* 21 (2020), pp. 683 –692

D. WENZEL and A. VOIGT. *Multiphase field models for collective cell migration*. 2021. arXiv: 2106.10552

Furthermore we also give a short outlook on the methods and results that have been developed during two different student research projects that are closely related to the topics of this thesis.

Part 7.2.1 - Growth and Division of Cells

H. P JAIN. "Phase Field Modelling of Active Interacting Cells that Grow and Divide". Masters Thesis. Technische Universität Dresden, 2021

H. P JAIN, D. WENZEL, and A. VOIGT. *The impact of contact inhibition on collective cell migration and proliferation*. 2021. arXiv: 2108.04743

Part 7.2.2 - Cellular Structures on Curved Manifolds

L. HAPPEL. "Multi Phase Field Models for Cellular Structures on the Sphere". Masters Thesis. Technische Universität Dresden, 2021

2 | PRELIMINARIES

The models considered in this thesis are given as evolution equations, derived from energy formulations. This versatile approach allows for physically motivated descriptions of complex systems, solely based on the fundamental tendency of nature trying to attain states of minimal energy. Furthermore, we will investigate the alignments in cellular structures with descriptions known from liquid crystal systems, using so-called Q-tensors.

We start by giving the general mathematical framework in terms of differential operators and introduce the notation used throughout the rest of the thesis in Section 2.1. Using this knowledge, we shortly review energy based formulations for the description of physical systems and the definition of evolution equations based on gradient flow approaches in Section 2.2. Afterwards, we address the topic of Q-tensor fields in Section 2.3 and nematic structure in Section 2.4, as required for the used methods in analyzing cell alignment.

2.1 | DIFFERENTIAL OPERATORS AND NOTATION

The considered problems are defined on a spatial domain $\Omega \subset \mathbb{R}^d$. In particular we will construct most methods in two dimensions, i.e. $d = 2$, and only in Chapter 7 give an outlook towards two-dimensional manifolds $\Gamma \subset \mathbb{R}^3$. In general, we assume the domain Ω to be bounded and sufficiently smooth. Furthermore, due to the dynamical nature of real-world phenomena, all models are defined depending on time with time horizon assumed to be the finite interval $[0, T]$.
Whenever not explicitly stated otherwise, both scalar valued $f : \Omega \times [0, T] \to \mathbb{R}$, vector valued $\mathbf{v} : \Omega \times [0, T] \to \mathbb{R}^d$ and tensor valued functions $\mathbf{Q} : \Omega \times [0, T] \to \mathbb{R}^{d\times d}$ are assumed to depend on both time and space. However, for the sake of readability, we use the Landau notation exclusively for derivatives with respect to spatial variables and, as a consequence, define the following operators:

- Gradient of f : $\nabla f = \left[\frac{\partial f}{\partial x_1}, \ldots, \frac{\partial f}{\partial x_d}\right]^T$
- Divergence of $\mathbf{v}$: $\nabla \cdot \mathbf{v} = \sum_{i=1}^{d} \frac{\partial v_i}{\partial x_i}$

- Laplacian of f : $\Delta f = \nabla \cdot \nabla f = \sum_{i=1}^{d} \frac{\partial f^2}{\partial x_i^2}$

Furthermore, vectors in $\mathbb{R}^d$ are multiplied using the standard scalar product defined by

$$\mathbf{u} \cdot \mathbf{v} = \sum_{i=1}^{d} u_i v_i$$

which naturally extends to vector valued functions.
Additionally, we want to introduce the differential operators for tensor fields which are less commonly known. Consider a tensor in matrix representation, given by

$$\mathbf{Q} = \begin{bmatrix} Q_{00} & Q_{01} \\ Q_{10} & Q_{11} \end{bmatrix}$$

without any additional properties. Then we define (in Cartesian representation) the following operators:

- Trace of $\mathbf{Q}$: $\mathrm{tr}\mathbf{Q} = Q_{00} + Q_{11}$
- Divergence of $\mathbf{Q}$: $\nabla \cdot \mathbf{Q} = \begin{bmatrix} \partial_x Q_{00} + \partial_y Q_{01} \\ \partial_x Q_{10} + \partial_y Q_{11} \end{bmatrix}$
- Gradient of $\mathbf{Q}$: $\nabla \mathbf{Q} = \frac{\partial \mathbf{Q}}{\partial_x} \otimes e_1 + \frac{\partial \mathbf{Q}}{\partial_y} \otimes e_2$

Here, we have used the basis vectors e_1 and e_2 of the Cartesian coordinate system and the outer product $\otimes$. For more detailed insights we refer to the widely available literature on the topic, for example [AMR88].

2.2 | VARIATIONAL DERIVATIVES AND GRADIENT FLOW

The mathematical formulation of all models introduced in this thesis starts with an energy description of the system. Given the assumption that processes in nature always aim towards the minimization of some energy, this results in an optimization problem. The huge advantage of this approach is the flexibility of usage - from simple, stationary two-phase substances to highly complex descriptions of active multicellular systems, the essence of the model is preserved.
Given this concept, the modeling process follows always the same steps:

(i) Find an appropriate energy, describing the phenomena of interest in the considered system.

(ii) Compute a suitable type of derivative of this energy, depending on the underlying space.

(iii) Simulate a time-dependent energy minimization process of the given energy, guided by the derivative computed before.

Assume that the current state of the system is described by a function $\phi : \Omega \to \mathbb{R}$, which could for example represent the concentration of some chemical or, in our cases, implicitly describe position and shape of a cell. Assume furthermore $\phi \in H$ for some Hilbert Space of sufficient smoothness, usually a Sobolev Space of a certain order. The energy of the system can be described by a functional $\mathcal{E} : H \to \mathbb{R}$, i.e. an

element of the dual space H^*. While the choice of the $\mathcal{E}$ is motivated from the specific application and will be postponed to Chapters 4, 5 and 6, the computation of some suitable derivative on the infinite dimensional space H^* requires the mathematical concept of variational derivatives which shall be introduced here.

2.2.1 | VARIATIONAL DERIVATIVES

We want to briefly introduce the definition of variational derivatives, a common generalization of classical differentiation towards spaces of functionals. Note that the name functional derivative is also widely used. The details and full theory can be found in a broad range of literature, for example the original work of Richard Courant and David Hilbert in [CH89]. While it is possible to define the following concepts in a much more general setting, we will restrict all considerations to the case of relevance for this thesis.

Definition 1 (Variational Derivative)**.**
*Let H be a Hilbert space and $\mathcal{E} \in H^*$. Then we call $\mathcal{E}' \in H^*$ the **variational derivative** of $\mathcal{E}$ if*

$$\left[\mathcal{E}'(\phi), h\right]_{H^* \times H} = \lim_{\tilde{\xi} \to 0} \frac{1}{\tilde{\xi}} \left(\mathcal{E}(\phi + \tilde{\xi} h) - \mathcal{E}(\phi)\right) \tag{2.1}$$

holds for all for all $h \in H$.

The definition of the variational derivative can be seen as a straight forward generalization of the classical derivative towards more complex spaces. For the practical use, it can, however, be convenient to choose a different representation.

Remark 1.
If the limit in (2.1) *exists, the Riesz Representation Theorem guarantees the existence of an element $\nabla \mathcal{E} \in H$ that fulfills*

$$\langle \nabla \mathcal{E}, h \rangle_H = \left[\mathcal{E}'(\phi), h\right]_{H^* \times H}$$

for all $h \in H$ and the intrinsic scalar product $\langle \cdot, \cdot \rangle_H$ of the space H.

The choice of H, which is in practical examples not always uniquely given, has a huge influence on the definition of $\nabla \mathcal{E}$. We will thus, in the following, use the additional subscript $\nabla_H \mathcal{E}$ to clarify the underlying space.
A common case for the usage of variational derivatives is the space $H = L_2(\Omega)$. In this case, a slightly different notation is frequently used, which is additionally helpful in case of multivariate functionals. Consider now

$$\mathcal{E} : L_2(\Omega) \times L_2(\Omega) \to \mathbb{R}, (\phi, \psi) \mapsto \mathcal{E}(\phi, \psi),$$

with two arguments, which occurs for example in the description of coupled physical systems. Let $\nabla_{L_2} \mathcal{E} \in L_2(\Omega)$ be the representative of $\mathcal{E}' \in L_2(\Omega)^*$ with respect to the first variable. Then we usually write

$$\frac{\delta \mathcal{E}}{\delta \phi} := \nabla_{L_2} \mathcal{E},$$

while accordingly the respresentative of the variational derivative with respect to the second variable is denoted by $\frac{\delta \mathcal{E}}{\delta \psi}$.
Frequently used in this thesis, is also the variational derivative in $H^{-1}(\Omega)$, i.e. the dual space of $H_0^1(\Omega)$ with respect to the L_2 scalar product $\langle \cdot, \cdot \rangle_{L_2}$.

Remark 2.
Let

$$\mathcal{E} : H^{-1}(\Omega) \to \mathbb{R}$$

be a functional. Then the variational derivative in $H^{-1}(\Omega)$ is given by

$$\nabla_{H^{-1}}\mathcal{E} = -\Delta\frac{\delta\mathcal{E}}{\delta\phi} = -\Delta(\nabla_{L_2}\mathcal{E}),$$

i.e. there is a close connection between variational derivatives in $L_2(\Omega)$ and $H^{-1}(\Omega)$.

For the sake of simplicity, we will in the following mostly use notations of the form $\frac{\delta\mathcal{E}}{\delta\phi}$, when using variational derivatives and distinguish between L_2 and H^{-1} derivatives with the observation in Remark 2.
The systems considered in this thesis usually involve time-dependent descriptions of the state. As a consequence a change from ϕ to $\phi + \xi h$ is caused by changing the time. The time derivative of the energy can then be transformed to the standard form of a variational derivative, according to equation (2.1), using a simple Taylor expansion and is given by

$$\begin{aligned}\frac{\partial}{\partial t}\mathcal{E}(\phi(t)) &= \lim_{\epsilon\to 0}\frac{1}{\epsilon}\Big[\mathcal{E}(\phi(t+\epsilon)) - \mathcal{E}(\phi(t))\Big] \\ &= \lim_{\epsilon\to 0}\frac{1}{\epsilon}\Big[\mathcal{E}(\phi(t) + \epsilon\partial_t\phi(t) + \mathcal{O}(\epsilon^2)) - \mathcal{E}(\phi(t))\Big] \\ &= \lim_{\epsilon\to 0}\frac{1}{\epsilon}\Big[\mathcal{E}(\phi(t) + \epsilon\partial_t\phi(t)) - \mathcal{E}(\phi(t))\Big] \\ &= \langle\nabla_H\mathcal{E}, \partial_t\phi(t)\rangle_H.\end{aligned} \tag{2.2}$$

2.2.2 | Energy Minimization and Gradient Flow

Having introduced a suitable concept for derivatives in the setting of energy functionals, we now use this to define a corresponding evolution equation. Following the general rule that nature always tries to minimize certain energies - a special form of the *Second Law of Thermodynamics* - a simple dynamical system can be defined by assuming the system variable ϕ changes according to the direction of the steepest descent in the energy.
As a direct transfer of the concepts in Subsection 2.2.1, the choice of the underlying Hilbert Space determines the definition of the energy gradient and thus also the resulting evolution equation. At this point, we want to name the two famous approaches that will play a crucial role in the model derivation later in this thesis.
Using $H = L_2$ as underlying space, the resulting L_2 *gradient flow* of $\mathcal{E}$ is given by

$$\partial_t\phi = -\nabla_{L_2}\mathcal{E} = -\frac{\delta\mathcal{E}}{\delta\phi},$$

which is the basis for many famous differential equations.

Example 1.
Consider the space $L_2(\Omega)$ for some bounded domain Ω and the energy

$$\mathcal{E} : \phi \mapsto \frac{1}{2}\int_\Omega |\nabla\phi|^2.$$

Then it holds

$$\begin{aligned}\int_\Omega \frac{\delta \mathcal{E}}{\delta \phi} h &= \lim_{\xi \to 0} \frac{1}{2\xi} \left(\mathcal{E}(\phi + \xi h) - \mathcal{E}(\phi)\right) \\ &= \lim_{\xi \to 0} \frac{1}{2\xi} \left(\int_\Omega |\nabla \phi + \xi \nabla h|^2 - \int_\Omega |\nabla \phi|^2 \right) \\ &= \lim_{\xi \to 0} \frac{1}{2\xi} \left(\int_\Omega \left(|\nabla \phi|^2 + 2\xi \nabla \phi \cdot \nabla h + \xi^2 |\nabla h|^2\right) - \int_\Omega |\nabla \phi|^2 \right) \\ &= \int_\Omega \nabla \phi \cdot \nabla h \\ &= \int_\Omega -\Delta \phi h \quad (\textit{ + boundary terms})\end{aligned}$$

and so we can conclude that the variational derivative of $\mathcal{E}$ is given by

$$\frac{\delta \mathcal{E}}{\delta \phi} = -\Delta \phi.$$

From this computation, we observe that the famous heat equation, given by

$$\partial_t \phi(t) - \Delta \phi(t) = 0,$$

can be derived as the L_2 gradient flow of the energy $\mathcal{E}$.

On the other hand, if the underlying space is chosen to be H^{-1}, the situation is slightly different. We use the gradient descent approach

$$\partial_t \phi(t) = -\nabla_{H^{-1}} \mathcal{E}$$

and make use of the observation in Remark 2 to get

$$\partial_t \phi(t) = \Delta \frac{\delta \mathcal{E}}{\delta \phi},$$

which is called the H^{-1} gradient flow and has entirely different dynamics, as we will see in the following chapters.

Example 2.
Consider again

$$\mathcal{E} : \phi \mapsto \frac{1}{2} \int_\Omega |\nabla \phi|^2$$

and remember the computation

$$\frac{\delta \mathcal{E}}{\delta \phi} = -\Delta \phi$$

that was done in example 1. The H^{-1} gradient flow is given by

$$\partial_t \phi(t) = \Delta \frac{\delta \mathcal{E}}{\delta \phi} = -\Delta \Delta \phi(t),$$

which is a fourth-order diffusion equation.

While the general concept of a gradient flow, regardless of the underlying space, is intuitive, it is not obvious that this approach actually leads to an energy minimization procedure.

Lemma 1.
Let H be a Hilbert Space and $\mathcal{E} \in H^*$. Consider the gradient flow $\partial_t \phi(t) = -\nabla_H \mathcal{E}$. Then we have

$$\frac{\partial}{\partial t}\mathcal{E}(\phi(t)) \leq 0,$$

so the energy of the system decays over time.

Proof. With the computation in (2.2) we have

$$\frac{\partial}{\partial t}\mathcal{E}(\phi(t)) = \langle \nabla_H \mathcal{E}, \partial_t \phi(t) \rangle_H$$

and then the definition of the gradient flow yields

$$\langle \nabla_H \mathcal{E}, \partial_t \phi(t) \rangle_H = -\langle \partial_t \phi(t), \partial_t \phi(t) \rangle_H = -||\partial_t \phi(t)||_H^2 \leq 0.$$

□

With the concept of energy formulations, variational derivatives and gradient flows, we have introduced a versatile and powerful setup, applicable in a wide range of areas. We will devote chapter 3 largely to the derivation of appropriate energies for the description of multicellular structures and then use their respective variational derivatives in the following chapters for the definition of evolution equations.

2.3 | Q-Tensor Fields

After introducing only the basic differential operators for tensor fields in Section 2.1, we now want to focus on a special class of tensors and go into more details. Due to their relevance for a variety of applications, especially in our case for the description of nematic alignment structure, we introduce the Q-tensors.

Definition 2 (Q-Tensor)**.**
Let $\mathbf{Q}$ be a second-order tensor with components

$$\mathbf{Q} = \begin{bmatrix} Q_{00} & Q_{01} \\ Q_{10} & Q_{11} \end{bmatrix}.$$

*If both $\mathbf{Q} = \mathbf{Q}^T$ and $tr\mathbf{Q} = 0$ hold, we call this symmetric, tracefree tensor a **Q-tensor**.*

From Definition 2 we can conclude that for every Q-tensor both $Q_{00} = -Q_{11}$ (tracefree) and $Q_{10} = Q_{01}$ (symmetric) hold. Thus, we will usually reduce the notation for the components of Q-tensors to

$$\mathbf{Q} = \begin{bmatrix} Q_0 & Q_1 \\ Q_1 & -Q_0 \end{bmatrix},$$

underlining that there are in fact only two independent components. Given this very particular structure of the Q-tensors, additional observations can be made. The most

relevant one for this thesis, regarding the eigenstructure, is given in the following result.

Lemma 2.
Let $\mathbf{Q}$ *be a Q-tensor according to Definition 2 with* $Q_1 \neq 0$.
Then the two distinct eigenvalues of $\mathbf{Q}$ *are given by*

$$\lambda^{\pm} = \pm\sqrt{Q_0^2 + Q_1^2}$$

with corresponding eigenvectors

$$\eta^{\pm} = \begin{bmatrix} \dfrac{Q_0 + \lambda^{\pm}}{Q_1} & 1 \end{bmatrix}^T.$$

Proof. Let η^+ and λ^+ as before. Then

$$\begin{aligned} \begin{bmatrix} Q_0 & Q_1 \\ Q_1 & -Q_0 \end{bmatrix} \begin{bmatrix} \dfrac{Q_0 + \lambda^+}{Q_1} & 1 \end{bmatrix}^T &= \begin{bmatrix} \dfrac{Q_0^2 + Q_0\lambda^+ + Q_1^2}{Q_1} & \lambda^+ \end{bmatrix}^T \\ &= \lambda^+ \begin{bmatrix} \dfrac{Q_0 + \lambda^+}{Q_1} & \lambda^+ \end{bmatrix}^T. \end{aligned}$$

The computation for η^- and λ^- can be done analogously. □

There is a variety of lessons we learn from Lemma 2. Aside of the comfortable situation of having an analytic description of the whole eigensystem, it even has some helpful properties.

Remark 3.
For any Q-tensor $\mathbf{Q} \in \mathbb{R}^{2\times 2}$ *with* $Q_1 \neq 0$ *the eigenvectors form an orthogonal basis of* $\mathbb{R}^2$.
This can be verified from the computation

$$\begin{aligned} \eta^+ \cdot \eta^- &= \begin{bmatrix} \dfrac{Q_0 + \lambda^+}{Q_1} & 1 \end{bmatrix}^T \cdot \begin{bmatrix} \dfrac{Q_0 + \lambda^-}{Q_1} & 1 \end{bmatrix}^T \\ &= \left(\frac{Q_0 + \lambda^+}{Q_1}\right)\left(\frac{Q_0 + \lambda^-}{Q_1}\right) + 1 \\ &= \frac{Q_0^2 - Q_0\sqrt{Q_0^2 + Q_1^2} + Q_0\sqrt{Q_0^2 + Q_1^2} - Q_0^2 - Q_1^2}{Q_1^2} + 1 = 0. \end{aligned}$$

This property is furthermore true for any (second-order) Q-tensor in $\mathbb{R}^d$ *and any* $d \in \mathbb{N}$.

We will use the property given in Remark 3, when describing cell shape using a Q-tensor, for example in Subsection 3.4.2 in the definition of an elongation based activity or in Subsection 6.2.1, to describe the overall nematic structure of the tissue model.
While the case $Q_1 = 0$ was formally excluded in Lemma 2 and Remark 3, this is not excluded from the definition of Q-tensors and even plays a crucial role, for example in the identification of topological defects, see 6.2.2. This case is however simple to treat, keeping in mind that the structure of $\mathbf{Q}$ simplifies to

$$\mathbf{Q} = \begin{bmatrix} Q_0 & 0 \\ 0 & -Q_0 \end{bmatrix}$$

Then the euclidean basis vectors e_1 and e_2 form an orthogonal basis of the eigenspace of $\mathbf{Q}$ with corresponding eigenvalues Q_0 and $-Q_0$.
These rather theoretical constructions will form the basis for a variety of concepts, for example the introduction of nematic structure in the following section.

2.4 | Liquid Crystals and Nematic Structure

Various materials are known to have states of matter that go beyond the typical classifications solid, liquid and gaseous. One famous example are the so-called *liquid crystals*, a type of material, which exhibits a hybrid state of matter with properties of both liquids - like the existence of flowing patterns - and solids - like a crystalline order structure.
The theoretical and experimental investigation of liquid crystals has a long history and we only want to touch this topic here, to give a rough idea of how the concepts can be helpful for the investigation of cellular structures. For more details we refer to the variety of literature on the topic, e.g. [Cha92; GP93]. In liquid crystal systems, particles typically have a rod-like shape with a specific head-tail symmetry. More precisely, this symmetry implies that no distinction between a certain particle and the π-rotated version of the particle is possible.

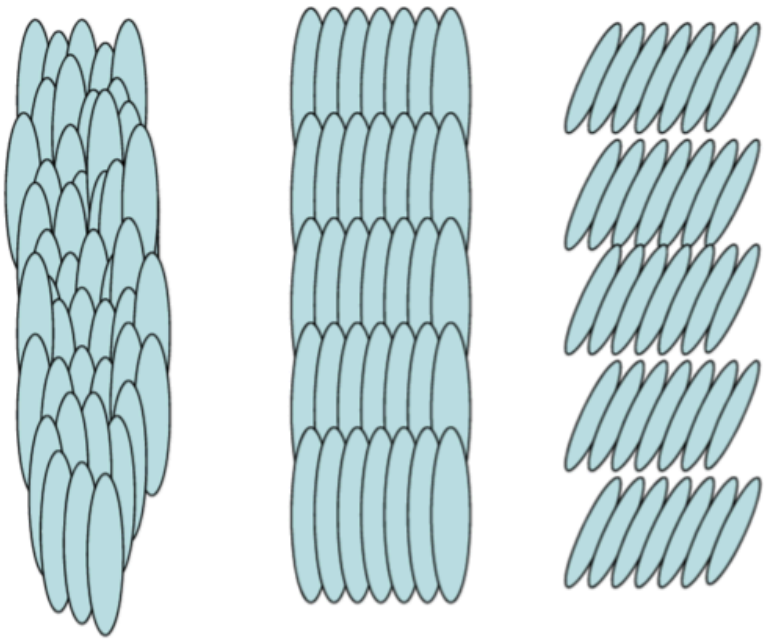

FIGURE 2.1: Schematic visualization of the different phases in liquid crystals: nematic, smectic A and smectic C phase from left to right. Taken and adapted from [IS13].

The detailed ordering structure in liquid crystal systems can differ, depending on a variety of factors, for example material composition and temperature. It is, however, possible to identify characteristic phases in the alignment structure. The most typical configurations that occur in $2D$ systems are shown in Figure 2.1. The nematic phase is characterized by a certain degree of orientational order but no positional order, i.e. the elongated particles have a preferred direction but the centers can be located anywhere in space. This will be of highest importance, as similar orderings

can be observed in cellular structures, see Chapter 6. The smectic phases are characterized by more ordering in the sense that particle centers are aligned in layers. For the smectic A phase, the orientation is exactly orthogonal to the layer direction, while this is rotated by some particular angle in the smectic C phase.
The mathematical description of liquid crystals or more general systems with nematic order is not trivially given. In particular, the head-tail symmetry makes the description difficult. Vector fields for example, with clearly distinct heads and tails, are not suited for the task. The usual approach is to describe the system using a Q-tensor field, where the eigenvectors represent the particle directors. In Section 2.3, we have observed that the eigensystems of these tensors have certain special properties. In particular, the fact that the eigenvectors form an orthogonal system and can be analytically computed from the components of the tensor. Furthermore, eigenvectors are always invariant under scalar multiplications, perfectly resembling the fact that head and tail of a director can be identified.
While the theory of liquid crystals and their phases is rich, we will not go into any more details at this point and refer to the aforementioned literature. Instead we want to focus solely on the essence of nematic order structure, namely the partial ordering of rod-like particles with locally preferred directions and the occurrence of topological defects in those director fields. We will use these concepts, for example, in the construction of two different mechanisms of propulsion, in Section 3.4, and the investigation of the alignment in tissue models, in Chapter 6.

Having introduced the general setup and notation, we have used this chapter to review some basic concepts like the formulation of evolution equations from energies and their variational derivatives. Furthermore, we have introduced Q-tensors, a type of second-order tensor with special properties that give rise to a use in the description of partially ordered systems of rod-like particles, for example in liquid crystal materials.

3 Model Derivation and Implementation

The derivation and investigation of computational models for cellular structures has been a topic of scientific interest for decades. Especially in the last years, due to new approaches in modeling and simulation of various types of physical, mechanical or chemical systems and the rapidly increasing possibilities in high performance computing, this topic has moved into focus more and more.

This thesis is focused on models applicable for epithelial monolayers. These systems are characterized by an effectively two-dimensional (flat) ordering structure or, more precisely, an area that is several times larger compared to the thickness. This gives rise to the distinction between a well-defined top (apical), bottom (basal) and side (lateral) of the tissue. Figure 3.1 shows the significant differences between the apical and the lateral view on epithelial tissue, exemplary visualized in the Drosophila Wing imaginal disc. In particular, the approximately polygonal packing structure in apical perspective becomes obvious which will be a subject of interest in the following chapters.

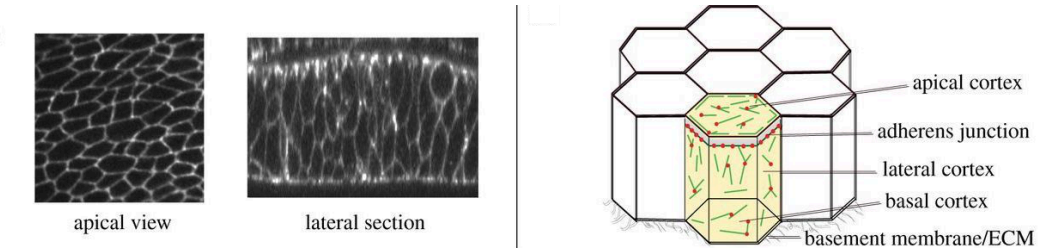

FIGURE 3.1: Drosophila Wing imaginal disc from apical (left, taken from [Sta+10]) and lateral perspective (middle, taken from [Bie+16]). Schematic visualization of epithelial cell monolayers (right, taken from [AGS17]).

From the point of view of *in vitro* experiments, epithelial cultures are usually plated as monolayers. In order to create comparable setups and due to the high computational requirements which will be addressed later, many existent models describe epithelial structures as two-dimensional. We will thus restrict most considerations to these types of models and only in Chapter 7 give an outlook to curved manifolds in three-dimensional space. The goal of this thesis is to derive and investigate a class of Multi-Phasefield models for cellular structures, based on the following key properties:

(i) Each cell is described as an individual, deformable object. This creates flexibility in shape changes.

(ii) Interactions between cells are defined explicitly, depending on the intercellular distance. This allows to include both adhesion and repulsion mechanisms.

(iii) Cell activity can be included using different approaches. This gives the possibility to adjust simulations to the organism of interest or the experimental setup.

This chapter is structured as follows: in Section 3.1, we review other existing models for cells and tissue, from a macroscopic to a microscopic scale. Afterwards, we start with the derivation of the models for this thesis, successively building a setup for *in silico* experiments fulfilling all three aforementioned key properties. In Section 3.2, we derive a description of an individual cell as a deformable object using the famous Cahn-Hilliard energy. Afterwards, we generalize this towards multicellular systems with cell-cell interactions in Section 3.3. The following Section 3.4 is purely devoted to the definition of different mechanisms of activity that are capable of driving the cell out of equilibrium states. We conclude this chapter with remarks on the boundary conditions in Section 3.5 and implementation in Section 3.6.

3.1 | REVIEW OF EXISTING MODELS

A variety of different computational models was introduced for the description of cells and tissue. The representation of these complex structures usually requires a compromise between detail and computational effort. This results in different scales, from a very coarse grained description (large cell numbers, no subcellular details) using lattice models in 3.1.1 and particle models in 3.1.2 across a meso-scale (medium cell numbers, low subcellular details) using vertex models in 3.1.3 towards the whole-cell models in 3.1.4 (single cells, large subcellular details).

3.1.1 | CELLULAR AUTOMATA / LATTICE MODELS

Lattice models can be seen as the most minimalistic type of description for cellular structures. They rely on an underlying polygonal tessellation of a domain, constructed by a set of lattices with a unique numbering. The state of the system is then described by the cells occupying a certain lattice. Different variants of this concept exist, depending on the number of cells that may occupy a lattice:

1. Every cell occupies exactly one lattice. Such models can be used with regular tessellations or unstructured ones, compare Figure 3.2. It is commonly used in cancer models to study tumor growth, see e.g. [BSD07].

2. A single lattice site can be occupied by multiple cells. This enables irregular distributions, without the (more costly) computation of irregular lattices. On the downside, this comes with reduced information about position and volume of individual cells. More details can be found in [Rad+09].

3. One cell can occupy multiple lattice sites. Also often denoted by cellular potts model, this approach is capable of describing more complex cell shapes on structured lattices. Every lattice is assigned a unique identifier, for example the index of the respective cell. Examples can be found in [GG92] or [ACR07].

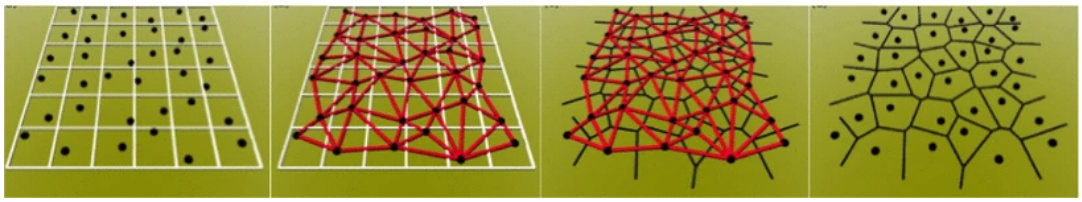

FIGURE 3.2: Construction of unstructured lattices for cellular automata. From left to right: Starting with a regular square grid and one point randomly distributed in each cell, Delaunay triangulation for the points and Voronoy tessellation to create the dual grid. Taken from [Lie+15].

Furthermore, it is possible to additionally store a velocity for each cell instead of just the position. This naturally leads to different emerging patterns in cellular flow and can, on a large scale, even result in behavior known from incompressible Navier Stokes equations, see e.g. [FHP86]. Even though originally introduced in a physical context, these types of models have also been successfully applied for growth and in particular migration of cells in large systems. Further details can be found in [DD05] or [DDL01].
While the general approach of lattice models is very intuitive and computationally efficient, even for high numbers of cells, it lacks certain features that can be important. It is for example not possible to incorporate complex shapes of cells. Futhermore, as all types of lattice models are describing the whole structure as one stochastic process, there is very little flexibility in defining individual behavior or intracellular dynamics.

3.1.2 | PARTICLE MODELS

The limitations of lattice models are reached, as soon as the size of individual cells or the distance between multiple cells is required. The class of so-called particle models goes one step further by describing each cell i of the system as a round object

characterized by a center $\mathbf{X}_i$ and a radius R_i.

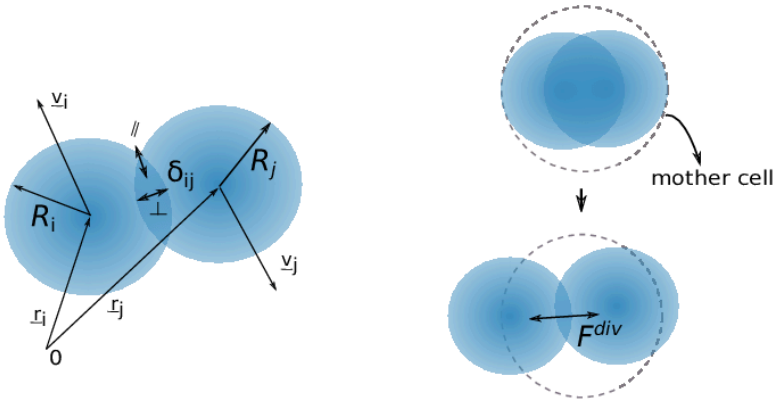

FIGURE 3.3: Visualization of particle-based cell models. (Left) Important quantities like radii R_i and R_j or the distance δ_{ij}. (Right) Cell division in particle based models. Taken from [Lie+15].

The first advantage of this approach is the definition of a distance between cells that can be computed as simple as

$$\delta_{ij} = |X_i - X_j| - R_i - R_j$$

and gives rise to a variety of interaction mechanism, see Figure 3.3 (Left) for a visualization. From simple repulsive dynamics preventing cells from overlapping, as performed in early work like [Vic+95], to short-range repulsion with mid-range adhesion, inspired by Lennard-Jones type potentials in [Bas+11], a wide range of choices is possible.
Another interesting phenomenon, that can be taken into account, is the concept of neighboring relations and in particular contact inhibition. This means that cell i may recognize the velocity $\mathbf{v}_j$ of its neighbors and adjust its own velocity $\mathbf{v}_i$ accordingly, enforcing locally correlated movement patterns and, on a large scale, sometimes even globally collective motion as observed in [Sep+13].
Cell growth and division can be incorporated in particle models, by simply varying the radius and replacing a single parent cell by two children after division. This process is visualized in Figure 3.3 (Right).
More complex approaches are even capable of incorporating moderate deformations, immediately before cell division, see for example [DH05]. Furthermore, it is also relatively straight forward to include cell-substrate interaction as done in [GLD05].
While particle models are a powerful extension of the lattice models and computationally still affordable, no internal structure is included. Similar to lattice models, the approaches presented here are appropriate on a macro-scale where the individual dynamics of each cell are of minor importance.

3.1.3 | VERTEX MODELS

Having introduced lattice models and particle models in Subsections 3.1.1 and 3.1.2 for macro-scale descriptions of large cell numbers with no subcellular detail, we here want to focus on the meso-scale. In particular, we are interested in approaches for the description of cellular structures that are capable of incorporating properties like

cell shape and more complex mechanisms of activity while still being computationally efficient for larger colonies of cells.
One popular example for these requirements are vertex models. The epithelial structure is represented by a set of points, capturing vertices where 3 or more cells are in contact. The cells are then described by connecting these vertices. The idea was originally introduced in the context of foams, see e.g. [WR84] and later on transferred to biological systems, which was extensively reviewed in [AGS17].
While it is possible to define vertex models also for the lateral section of epithelium (compare Figure 3.1) and even for three-dimensional cell packings, we want to focus on the description of two-dimensional vertex models for the apical view. The work in [NH01] generalized the phyiscal models to cellular structures. Intercellular interactions were introduced and compared for example in [Far+07]. This gave rise to comparisons with different experimental setups like wound closure as done in [NH09] or the wing development in Drosophila, see [Aig+10].
The dynamics are described purely in terms of equations of motion for the vertices. This means that vertex position $\mathbf{x}_i$ evolves according to the simple law

$$\eta \frac{\mathrm{d}\mathbf{x}_i}{\mathrm{D}t} = \mathbf{F}_i,$$

with $\mathbf{F}_i$ the total force acting on the vertex and η a mobility coefficient, see [Fle+14] for more detailed descriptions of the approach. While the general form of this evolution equation is rather intuitive, the particular choice of $\mathbf{F}_i$ is less trivial and we will not go into detail here.
One advantage of vertex models is the numerically unproblematic definition, involving ordinary differential equations, which allows simulations for larger numbers of cells at moderate cost. Furthermore, changes in shape (e.g. elongation or number of surrounding vertices) of individual cells are possible and result implicitly from the choice of $\mathbf{F}_i$.

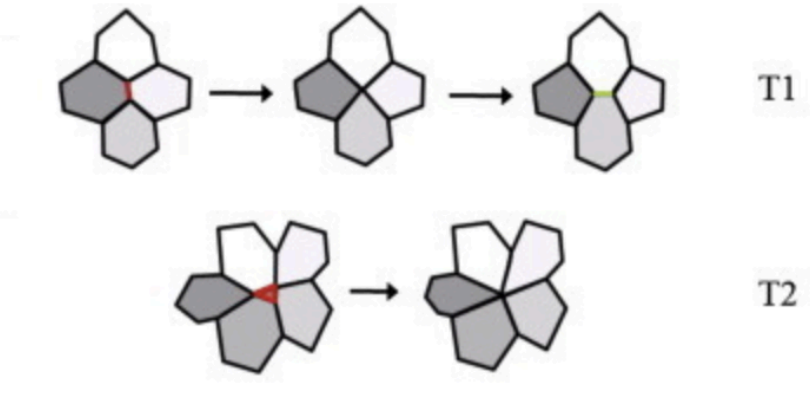

FIGURE 3.4: Schematic images for the typical T1 (top) and T2 (bottom) transitions in vertex models. If an edge becomes too short or the cell area is too small (marked in red), the vertices are repositioned or removed. Taken from [Fle+14].

A critical point of the approach is that numerous topological changes, such as the typical T1 transition - a change in neighbors - or T2 transition - shrinkage and apoptosis - have to be enforced actively. The T1 transition for example is usually enforced by actively repositioning vertices if a certain edge becomes too short while the T2

transition results from removing a number of vertices if the contained cell becomes too small, compare Figure 3.4.

3.1.4 | WHOLE-CELL MODELS

More recently, new methods in computational models have enabled the study of cells in a micro-scale description. The so-called whole-cell models try to capture as much microstructure of each individual cell as possible. A review on this topic can be found for example in [Szi+18].
Genetic components of cells, their influence on differentation or phenotype formation and the interplay with environmental factors are a highly complex system. Among other modeling approaches, the use of AI-based methods has been observed to be highly promising for the description of whole-cell models.

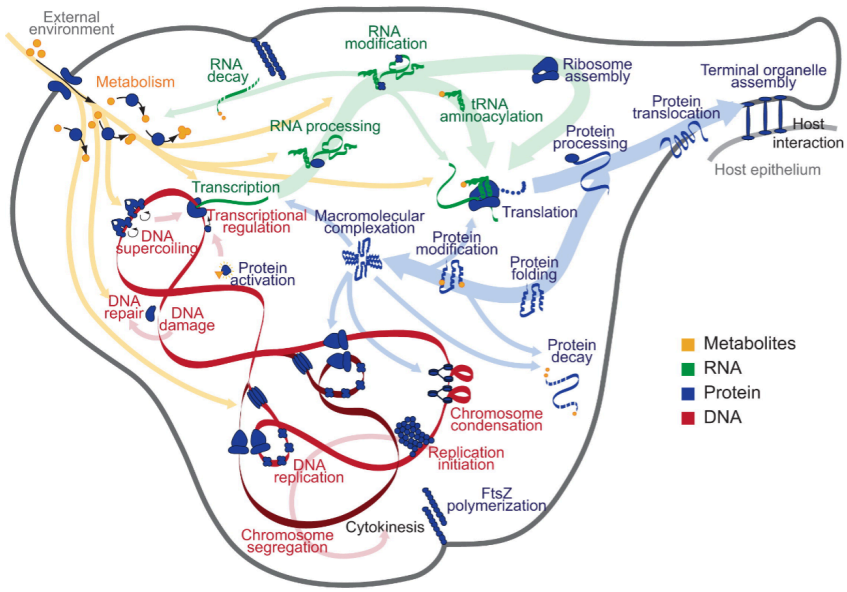

FIGURE 3.5: Schematic for the variety of intracellular processes and their interplay. Taken and adapted from [Kar+12].

One of the key advantages of AI-based methods is the ability to efficiently process large sets of experimental data and automatically adapt the model accordingly. On the other hand, the description of individual cells on a micro-scale is complex, see for example a schematic description for the variety of requirement components in Figure 3.5. From a computational point of view, this is not efficiently doable for large numbers of cells.

The models investigated in this thesis will describe cellular structures on an intermediate scale between microscopic and macroscopic approaches. In particular, the aim is to derive models that are capable of describing individual cells with more detail than the vertex models described in Subsection 3.1.3 but are less computationally demanding compared to the whole-cell models introduced in Subsection 3.1.4. The weaknesses of the vertex models, for example the limited flexibility in cell shapes which are always polygonal and the need to explicitly enforce topological transitions, shall be addressed.

3.2 | Individual Cells as Deformable Droplets

The first step on the way towards the description of cellular structures like epithelium is the description of an individual cell. We want to use a Phasefield approach as proposed for example in [MV14a] or [LZA15b], which allows cells to change their shapes almost arbitrarily.

3.2.1 | Diffuse Domain Approach

Consider a two-dimensional domain $\Omega \subset \mathbb{R}^2$, representing the apical perspective of a non-curved epithelial structure (compare Figure 3.1). To generalize this, we will in Chapter 7 give an outlook towards two-dimensional manifolds in $\Gamma \in \mathbb{R}^3$, representing curved monolayers.
Let the region of interest, later representing the cell, be denoted by the closed set $\Omega_1 \subset \Omega$ with interior Ω_1° and boundary $S = \Omega_1 \setminus \Omega_1^\circ$. We now want to create an implicit representation of Ω_1. To do this, define a smooth function $\phi : \Omega \to [-1, 1]$, such that $\phi \approx 1$ holds in Ω_1 while $\phi \approx -1$ holds in $\Omega \setminus \Omega_1$. This type of implicit representation of an arbitrarily shaped domain Ω_1 using a function ϕ is usually called a diffuse domain description, while ϕ is called a Phasefield, motivated by the distinction between interior and exterior phase.
The transition region between $\phi \approx -1$ and $\phi \approx 1$, which requires non-vanishing width to achieve continuity, is usually called the diffuse interface and the cross-section diameter is denoted by ϵ, see Figure 3.6. The sharp interface S can be approximated by the levelset $\phi = 0$, i.e.

$$S \approx \{x \in \Omega | \phi(x) = 0\}.$$

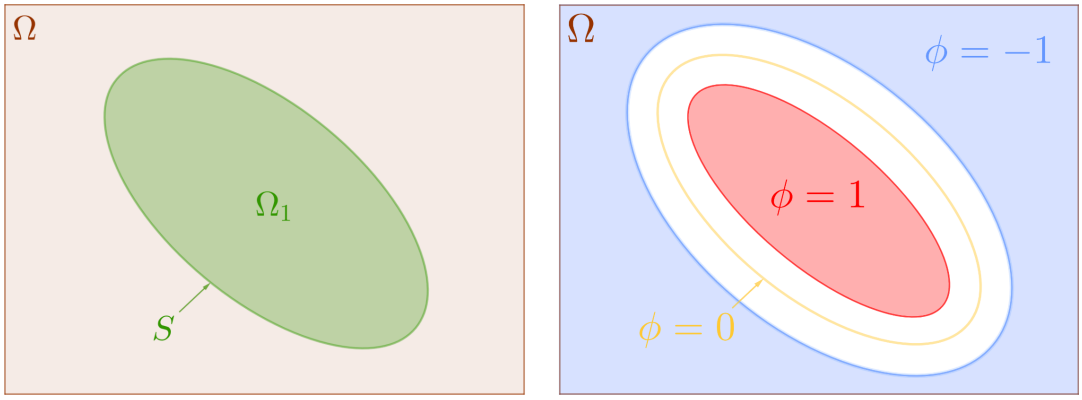

Figure 3.6: Schematic visualization of the Phasefield derivation. (Left) Original domain Ω_1 with sharp interface S. (Right) Phasefield function with $\phi \approx -1$ on the outside, $\phi \approx 1$ on the inside and a smooth transition region of width ϵ.

Starting in Subsection 3.2.2, we want to describe the evolution of Phasefields over time using partial differential equations. We will, however, mention at this point how it is possible to construct them from scratch, e.g. for initial conditions. Let Ω and Ω_1 be given. A classical approach is to use a (continuos) signed distance function $d : \Omega \to \mathbb{R}$, giving for any point $x \in \Omega$ the shortest distance to the surface S. Assume that d has negative sign inside of Ω_1° and positive sign in $\Omega \setminus \Omega_1$, to distinguish between the two regions. As a consequence, due to the continuity, $d \equiv 0$ holds

in S. For certain simple geometries, for example spheres and rectangles, the signed distance function can be derived analytically. Otherwise there exist different techniques to find approximations, e.g. the *Fast Marching Method* originally introduced in [Set96].
A Phasefield ϕ can then be derived directly from d. To do this, we introduce the parameter ϵ, modeling the width of the transition region between negative and positive sign, and define

$$\phi(x) := \tanh\left(\frac{d(x)}{\sqrt{2}\epsilon}\right).$$

It can be verified that this definition of ϕ satisfies the requirements for a Phasefield that have been given before. Figure 3.7 illustrates for a simple example geometry - a circle in $\mathbb{R}^2$ - both the signed distance function d and the resulting Phasefield ϕ. Due to the weak assumptions, this approach can cover a wide range of applications including the description of cell geometries.
Note that the choice of the tanh profile results from the equilibrium shape that the evolution equations introduced in Subsection 3.2.2 attain, see for example the original work of Cahn and Hilliard in [CH58].

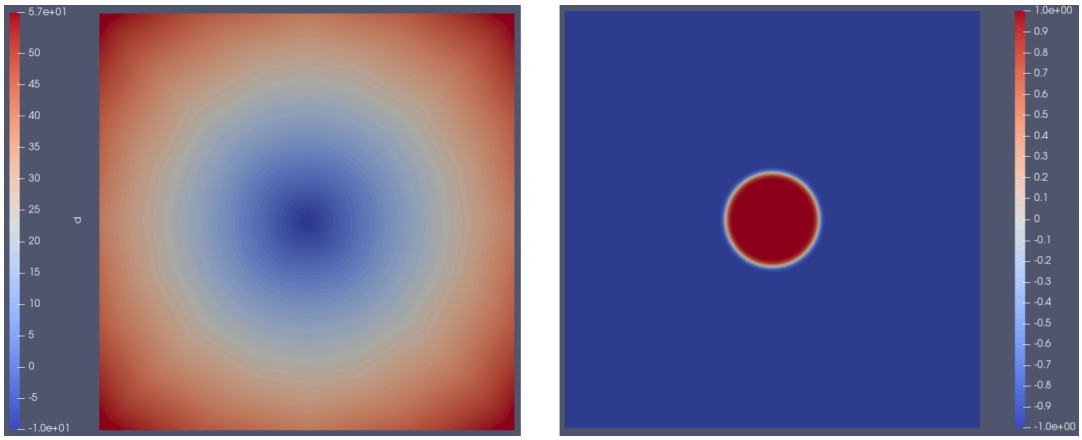

FIGURE 3.7: Signed distance function d (left) and resulting Phasefield function ϕ with interface-width $\epsilon = 0.5$ (right) for a circular geometry on the domain $\Omega = [0, 100]^2$. Blue and red color corresponds to negative and positive values respectively.

3.2.2 | TIME EVOLUTION OF PHASEFIELD DESCRIPTIONS

We have introduced a diffuse domain description using Phasefields $\phi : \Omega \to [-1, 1]$, capable of implicitly representing the interior of the cell as the region where $\phi \approx 1$ holds. This is, however, for the modeling of cellular structures only the very first step, keeping in mind that processes in nature are usually dynamically changing over time. In the following we will, as a consequence, always assume the Phasefields to depend on both time and space, i.e. $\phi : [0, T] \times \Omega \to [-1, 1]$.
A crucial requirement for the goal of describing cellular structures, is the preservation of a clear distinction between cell interior and exterior over time. To do this, we want to introduce energy formulations and describe the evolution of the system using gradient flow approaches according to Section 2.2.
To ensure the distinction between interior and exterior, we transfer an energy, originally introduced by Cahn and Hilliard in [CH58] in the context of phase separation

processes. Let

$$\mathcal{E}_{CH}(\phi) = \int_\Omega \frac{\epsilon}{2}|\nabla\phi|^2 + \frac{1}{\epsilon}W(\phi)\mathrm{d}x, \tag{3.1}$$

with $W(\phi) = \frac{1}{4}(\phi^2-1)^2$ the so-called double-well potential and ϵ scaling the width of the interface region.
The second term in this energy punishes deviations from both the $\phi = -1$ and $\phi = 1$ phase as these are the minima of the double-well W. The first term on the other hand punishes variations in ϕ and so the combination prefers piecewise constant ϕ with small transition regions between $\phi \approx -1$ and $\phi \approx 1$.

Remark 4.
Assume that an explicit description of the 0*-levelset*

$$S = \{x \in \Omega \big| \phi(x) = 0\}$$

is known and consider the interface area

$$E_A(S) = \int_S 1\mathrm{d}s.$$

Then $\mathcal{E}_{CH}(\phi) \to E_A(S)$ *holds for* $\epsilon \to 0$ *in the sense of* Γ*-convergence, see e.g. [CC92].*

From Remark 4 we can conclude that the introduced Cahn-Hilliard energy $\mathcal{E}_{CH}$ is an approximation of the surface area E_A.
In the remainder of this chapter, only energy formulations are described while the actual evolution equations are given in Chapters 4, 5 and 6. We will, however, make an exception here and derive the gradient flows of the energy $\mathcal{E}_{CH}$ as they result in famous partial differential equations.
One particular focus will be the conservation properties of the gradient flows, as this will be relevant for the context of describing cellular structures. Precisely, if we use the term conservation, we refer to

$$\frac{\partial}{\partial t}\int_\Omega \phi(t,x)\mathrm{d}x = 0,$$

which means that there are no changes in the total area of the domain implicitly represented by ϕ.
The variational derivative of $\mathcal{E}_{CH}$ in $L_2(\Omega)$, see Subsection 2.2.1, is given by

$$\frac{\delta\mathcal{E}_{CH}(\phi)}{\delta\phi} = -\epsilon\Delta\phi + \frac{1}{\epsilon}W'(\phi), \tag{3.2}$$

where we have used the notation emphasizing the variation over ϕ. For a given mobility parameter $\gamma > 0$, the L_2 gradient flow is then given by

$$\partial_t\phi = -\gamma\frac{\delta\mathcal{E}_{CH}(\phi)}{\delta\phi} = -\gamma\left(-\epsilon\Delta\phi + \frac{1}{\epsilon}W'(\phi)\right), \tag{3.3}$$

which is known as the Allen-Cahn equation. This evolution equation is not conservative for ϕ over time and the behavior is sometimes referred to as *Model A* type dynamics. This non-conservative approach, however, is not suitable for the description of cellular systems as this would include shrinkage and death of cells.

Using on the other hand an H^{-1} gradient flow and the observation in Remark 2, one arrives at

$$\delta_t \phi = \gamma \Delta \left(\frac{\delta \mathcal{E}_{CH}(\phi)}{\delta \phi} \right) = \gamma \Delta \left(-\epsilon \Delta \phi + \frac{1}{\epsilon} W'(\phi) \right), \tag{3.4}$$

which is called the Cahn-Hilliard equation or *Model B* type dynamics and conserves the area of the domain represented by ϕ. This makes H^{-1} gradient flows better suited for the implicit description of cellular structures using Phasefields.

In this section, we have derived a representation of a single, non-motile, deformable droplet implictly described by a Phasefield ϕ. Furthermore, we have introduced an energy serving as the basis for evolution equations and observed that only the H^{-1} gradient flow preserves the volume, making this the approach of choice for the Phasefield models in this thesis. The next step is a generalization towards models involving multiple Phasefields, representing different individual particles that may describe tissue.

3.3 | Multi-Cellular Models and Interaction

In the previous section, we have derived the first important component in the model describing cellular structures, namely implicit representations of the cell shape using Phasefields and the corresponding Cahn-Hilliard energy as basis for the evolution equations. The Cahn-Hilliard equation in (3.4) ensures a separation between intracellular and extracellular material and preserves an approximately circular shape for the $\phi \approx 1$ phase, if no external forces are applied.
The next step is the derivation of a description of multi-cellular systems. The foundation for this - and another strength of the Phasefield based approach - is to consider a set of multiple Phasefield variables $\{\phi_i\}_{i=1}^N$. Each ϕ_i implicitly describes exactly one cell. The total energy of the system is then given by

$$\mathcal{E}_{CH}\left(\{\phi_i\}_{i=1}^N\right) = \sum_{i=1}^N \mathcal{E}_{CH}(\phi_i) = \sum_{i=1}^N \int_\Omega \frac{\epsilon}{2} |\nabla \phi_i|^2 + \frac{1}{\epsilon} W(\phi_i) \mathrm{d}x, \tag{3.5}$$

where we have transferred the Cahn-Hilliard energy for one Phasefield as defined in (3.1) to the Multi-Phasefield system by summing up all individual contributions. This, however, is not sufficient for the description of multi-cellular systems as there exists no coupling or any intercellular forces. Practically, this would mean that any given cell would behave as if no other cell exists.
To overcome this problem, any appropriate model should at least include repulsive forces between the cells on short distances, in order prevent overlap. Additionally, we also want to introduce attractive forces to gain more flexibility in model construction. In the following we want to give an overview of different approaches for interaction potentials.

3.3.1 | Qualitative Phasefield-based Approach

The first approach, as used e.g. in [LZA15a], is defined directly in terms of the Phasefield of neighboring cells. As a prior step, we need a rescaled version of each Phasefield ϕ_i from value range $[-1, 1]$ to $[0, 1]$, as introduced in Section 3.2, using the affine

map

$$\tilde{\phi}_i = \frac{1}{2}\phi_i + \frac{1}{2}. \tag{3.6}$$

The equivalence

$$\{\tilde{\phi}_i > 0\} \cap \{\tilde{\phi}_j > 0\} = \emptyset \Leftrightarrow \tilde{\phi}_i \tilde{\phi}_j \equiv 0$$

holds and this gives rise to the intercellular repulsive energy

$$\mathcal{E}_{INT}^{rep}\left(\{\phi_i\}_{i=1}^N\right) := \sum_{i,j=1}^{N} \int_\Omega \tilde{\phi}_i^2 \tilde{\phi}_j^2. \tag{3.7}$$

Motivated by similar observations, an adhesive contribution to the energy can be introduced by

$$\mathcal{E}_{INT}^{ad}\left(\{\phi_i\}_{i=1}^N\right) := \sum_{i,j=1}^{N} \int_\Omega \nabla\tilde{\phi}_i \cdot \nabla\tilde{\phi}_j, \tag{3.8}$$

which essentially enforces the outer normals of both cells, represented by $\nabla\tilde{\phi}_i$ and $\nabla\tilde{\phi}_j$, to point in opposing directions. While this approach has been successfully used in various studies like [LZA15a; MYD19; Pey+19], it has certain downsides. Both repulsion and adhesion are introduced only in a qualitative way but not depending on the actual distance between cells. While the repulsive force is a purely numerical contribution, in order to prevent overlap, the adhesive force is motivated by intercellular bonds. On the other hand, the presented approach gives no possibilities of controlling the distance of adhesion and repulsion, one can only balance the two contributions. For these reasons, we will not use this approach in the studies here.

3.3.2 | DISTANCE-BASED INTERACTION

Motivated by the lack of control over the adhesion and repulsion distances in the qualitative interaction presented in Subsection 3.3.1, we want to introduce a different approach, based completely on the distance between two cells.
The definition of a distance, however, is not clear in diffuse interface models. The interface of cell j is given as the level-set $S_j = \{x \in \Omega | \phi_j(x) = 0\}$. For any point $x \in \Omega$ the signed distance of x to cell j is then given by

$$d_j^{sharp}(x) = -sgn(\phi_j(x)) \min\{|x-y| \mid y \in \Omega, \phi_j(y) = 0\},$$

which is an extension of the typical definition of distance between a point in space and a set of points. This quantity is not suited for practical applications as it is inefficient to compute. To overcome this problem, we want to use an approximation of the signed distance that can be computed from the Phasefield ϕ_j. According to [CH58], the equilibrium shape of ϕ_j in the diffuse interface region is a scaled tanh profile of the distance function, so we define

$$d_j^{diffuse}(x) := -\frac{\epsilon}{2} \ln\left(\frac{1+\phi_j(x)}{1-\phi_j(x)}\right) \tag{3.9}$$

which involves the inversion of tanh. However, as the tanh profile is only given in the diffuse interface region, only there $d_j^{diffuse}$ approximates d_j^{sharp} accurately enough. Another crucial component in this approach is the definition of an interaction potential w, depending on the distance d_j to a particular neighbor. In a sharp interface formulation, i.e. assuming knowledge of d_j^{sharp}, the interaction acting on a single cell i reads

$$\sum_{j \neq i} \int_{S_i} w(d_j^{sharp}(x)) \mathrm{d}x. \tag{3.10}$$

To transfer this into a more natural formulation for Phasefield models, we approximate the surface integrals using

$$B(\phi_i) = \frac{1}{\epsilon} \left(\phi_i^2 - 1\right)^2.$$

This transfers (3.10) into a diffuse domain formulation by defining the global interaction energy, combining contributions from all cells, given by

$$\mathcal{E}_{INT}^d(\{\phi_i\}) = \sum_{i=1}^{N} \sum_{j \neq i} \int_{\Omega} B(\phi_i) w(d_j^{diffuse}(x)) \mathrm{d}x. \tag{3.11}$$

This approach has the advantage of giving the flexibility to use different interaction potentials w. On the other hand, the strong non-linearity of the terms in (3.11) makes this approach computationally challenging. In the following, we will investigate different ways to choose the interaction potential and the effect on the resulting dynamics. Note that, in general, positive energy contributions model repulsion, while a negative sign represents adhesion. Note furthermore that we will omit the superscript clarifying the difference between the sharp and the diffuse notion of distance in the following. From here on out all definitions are in the diffuse interface formulation, i.e. $d_j := d_j^{diffuse}$.

Exponentially repulsive potential

Focusing only on the numerical requirement of short-range repulsion, in order to prevent overlap, we start with the construction of a strictly positive, i.e. purely repulsive, potential. In particular, we want to choose a potential with large values close to distances $d_j \approx 0$ but decaying fast for growing distances. The fast decay is required as the signed distance approximation involving the inversion of tanh is only valid inside the diffuse interface.
We choose a Gaussian potential, i.e. exponential dependence on the distance, by defining

$$w_E(d_j(x)) := \exp(-d_j^2(x)/\epsilon^2) \tag{3.12}$$

as suggested for example in [MV16]. By choosing ϵ^2 as scaling coefficient, we observe that the contributions for distances larger than ϵ, i.e. outside of the diffuse interface region, are negligibly small. This potential is visualized in Figure 3.8 (Left) and has proven to be numerically very stable. It will be extensively used in the study of purely repulsively interacting cells in the Chapters 4, 5 and 6.

Lennard-Jones potential

While the exponentially repulsive potential in (3.12) is well-suited to ensure the non-overlap condition throughout the simulation, it is strictly positive and thus includes no adhesive forces between cells. We now want to present a different approach, including also adhesion, by using the well-known Lennard-Jones potential, originally introduced in [Jon24] in the context of particle interaction.
Let

$$w_{LJ}(d_j(x)) := \left[\left(\frac{\epsilon}{2d_j(x)} \right)^{12} - 2 \left(\frac{\epsilon}{2d_j(x)} \right)^{6} \right], \tag{3.13}$$

which is commonly known as the $(12, 6)$ Lennard-Jones potential and visualized in Figure 3.8 (Right). Note that a rescaling with ϵ was added, adjusting the potential to the interface width.
One observes that w_{LJ} is, in contrast to w_E, not strictly positive, i.e. it also incorporates adhesive forces. In particular the sign is positive for $0 < d_j < \epsilon/2$ and negative for all values $d_j > \epsilon/2$ while decaying fast for increasing distances. While the minimal value of the potential is explicitly given as -1, it is not bounded from above. In particular there is a pole at $d_j = 0$, which can be numerically problematic. It can thus be useful to cut off the potential values above a certain threshold.

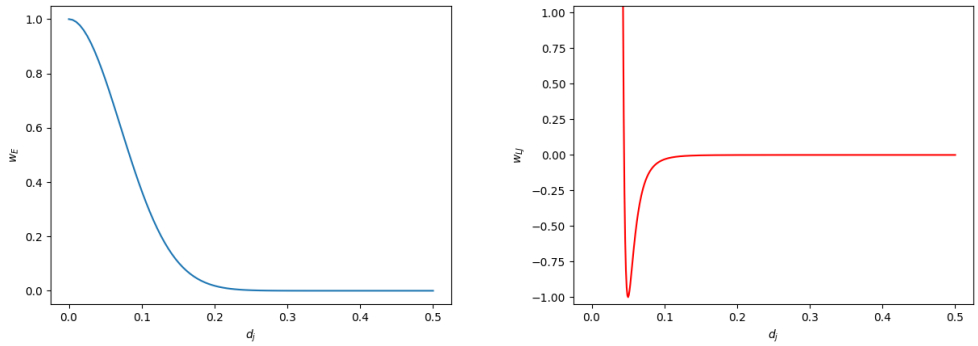

FIGURE 3.8: (Left) Exponentially repulsive potential in (3.12) and (Right) Lennard-Jones type potential in (3.13) for interface width $\epsilon = 0.1$ and distances up to $d_j = 0.5$.

While the Lennard-Jones type potential is interesting from a theoretical point of view, we have observed numerical instabilities. In particular, the distinction between adhesive and repulsive contributions, all given only inside the ϵ-wide diffuse interface, requires very fine resolutions in both time and space, which is not acceptable in practicable cases and thus the Lennard-Jones potential will not be used in the following.

3.3.3 | QUANTITATIVE PHASEFIELD-BASED APPROACH

The last approach for an energy contribution modeling intercellular interactions can be seen as a hybrid version of the Phasefield-based definition in Subsection 3.3.1 and the distance-based in Subsection 3.3.2. In particular, we want to combine the positive aspects of both approaches, in order to define a versatile interaction energy that allows for the definition of both adhesive and repulsive components.

The energy contribution

$$\mathcal{E}^{\phi}_{INT}(\{\phi_i\}) = \sum_{i=1}^{N} \sum_{j \neq i} \int_{\Omega} \tilde{\phi}_i w(\phi_j(x)) \mathrm{d}x \tag{3.14}$$

is a tranfer from (3.11) with different individual alterations. The first step was to remove the integral over the diffuse interface that enters with the term $B(\phi_i)$ and instead integrate over the cell interior using $\tilde{\phi}_i$. This removes the numerically problematic part of the Lennard-Jones type potential that both the repulsive and the adhesive regime have to act inside of the only ϵ-wide diffuse interface. On the other hand, we can preserve the concept of an interaction potential w incorporating positive and negative contributions instead of the individual parts for repulsion and adhesion as introduced in (3.7) and (3.8) which are difficult to control. In comparison to (3.11), the interaction potential does not depend on the approximated distance d_j but instead on the Phasefield ϕ_j itself.
When using this approach, we consider the interaction potential

$$w_{pol}(\phi_j) = 1 - (a+1)\left(\frac{\phi_i - 1}{2}\right)^2 + a\left(\frac{\phi_i - 1}{2}\right)^4, \tag{3.15}$$

which is a polynomial in ϕ_j and thus computationally unproblematic. Furthermore, indicating the versatility of this potential, it is parametrized by just one real-valued parameter a but still gives the possibility to include both repulsive and adhesive forces. In particular, for the choice $a = 1.0$, the potential is strictly positive and thus

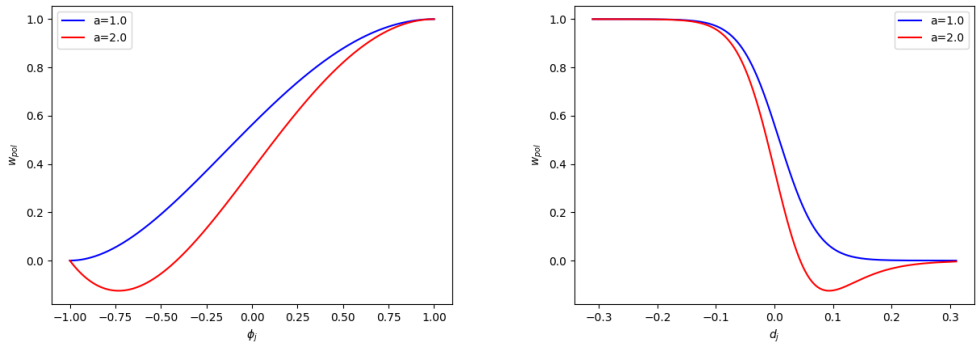

FIGURE 3.9: Visualization of the interaction potential in (3.15) for purely repulsive variant $a = 1.0$ (blue) and adhesive-repulsive variant $a = 2.0$ (red). The potential is visualized depending on both the Phasefield ϕ_j (left) and the resulting distance d_j (right). In both visualization the equal interface width $\epsilon = 0.1$ is chosen.

models purely repulsive forces while, for $a = 1.5$ or $a = 2.0$, a negative value range exists, which corresponds with adhesive forces. Figure 3.9 visualizes the potential for two choices of the parameter a, depending on the Phasefield value itself (Left) and on the resulting approximate distance d_j (Right) to increase comparability with the distance-based approaches in Subsection 3.3.2.
While this approach is strictly phenomenological and not motivated by physical interaction laws, it has certain advantages. In contrast to the distance-based approach, where only the distance between the interfaces is taken into account, the repulsive forces grow proportional to the overlap between cells, which seems more natural. Furthermore, aside of the versatility of changing the entire behavior depending on

just one parameter, it can also be numerically less problematic. Especially in case of an adhesive contribution, this approach is favorable compared to the Lennard-Jones potential as it is more regular in different ways (no pole exists and the area of adhesion is wider with a less steep descent) and thus significantly increases stability in computations.

3.4 | Mechanisms for Activity

The movement or motility of cells is crucial for a variety of developmental processes, both *in vivo* and *in vitro*. From morphogenesis to wound healing and cancer invasion, it is required for cells to actively change locations [FG09; Ror09; SM16]. Even though this has been studied for a long time, the precise mechanisms that create and moreover even coordinate cellular motion remain partially unclear and are still a focus of current research [AE07].
The investigation of different mechanisms for activity in cellular structures and the resulting patterns of motion is one of the main targets of this thesis. The *in silico* experiments performed with the following models can be a step towards a more complete understanding of the forces that drive cells and create the foundation of life.
While the system energy $\mathcal{E} = \mathcal{E}_{CH} + \mathcal{E}_{INT} + ...$ depends on the particular choice of the interaction mechanism and potentially other contributions according to the following sections, the general structure of the evolution equations for ϕ_i is always preserved. In particular, we include activity by a first-order term which reads

$$\partial_t \phi_i + v_0(\mathbf{v}_i \cdot \nabla \phi_i) = \Delta \frac{\delta \mathcal{E}}{\delta \phi_i} \tag{3.16}$$

for an individual propulsion $\mathbf{v}_i$ and a real valued scaling factor $v_0 \in \mathbb{R}$, which is constant for all cells. This section is devoted to the derivation of different possible choices for $\mathbf{v}_i$.
At this point, we want to emphasize that including activity into the evolution of the system changes the gradient flow structure. For $v_0 > 0$ the energy minimization, stated in Lemma 1 is no longer given.

3.4.1 | Random Walk

The first approach we consider here is the most simple one. Inspired by the dynamics of particle systems, the direction of propulsion can be assumed to be following a random process. Originally introduced for vertex models in [Bi+16; Gia+18; Yan+17] this concept was most recently applied for Multi-Phasefield models in [Loe+20].
The direction of motion for the cell is represented by an angle θ_i that follows the stochastic law

$$\mathrm{d}\theta(t) = \sqrt{2D_r}\mathrm{d}W_i(t), \tag{3.17}$$

where D_r is the rotational diffusivity parameter and W_i a Wiener process. The propulsion is then given by

$$\mathbf{v}_i^{ran} = \begin{bmatrix} \cos\theta_i \\ \sin\theta_i \end{bmatrix}, \tag{3.18}$$

which corresponds to a standard transformation between polar and cartesian coordinates. This means that the direction of motion at each time instance follows a rescaled normal distribution around the direction in the previous moment. At typical example for the random propulsion field is shown in Figure 3.10.

The major advantage of this approach is simplicity. The definition of $\mathbf{v}_i^{ran}$ is numerically unproblematic and offers wide possibilities for generalizations, e.g. from flat domains to definitions on manifolds as performed in Subsection 7.2.2. On the other hand, we observe that this propulsion mechanism is fully decoupled from the values of the Phasefield ϕ_i and thus the shape of the represented cell. This contradicts the findings in various experimental studies like [MK09], where a strong correlation between shape and motility of cells was observed. Furthermore, it does not include the modeling of any intracellular machinery like polymerization and depolymerization of actin filaments, which also seems to be relevant for the motility of cells as reported e.g. in [MO96].

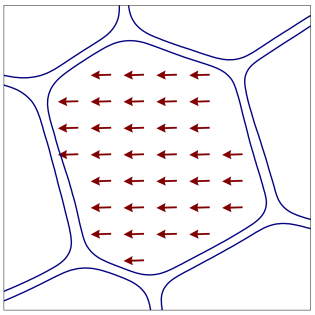

FIGURE 3.10: Schematic visualization of the levelset $\phi_i = 0$ and a random advection field $\mathbf{v}_i^{ran}$.

In the following subsections, we will define different types of propulsion mechanisms that take more and more detail into account, usually at the cost of higher computational effort.

3.4.2 | DEFORMATION-BASED NEMATIC FORCE

Having introduced the most basic random type of propulsion, which does not take the cell shape into account at all, we want to go one step further. In order to do this, we use the ideas proposed in [MYD19] for confluent monolayers that were applied to confined systems in [Pey+19], describing the mesoscopic shape of each cell using a geometrical Q-tensor.
For each Phasefield ϕ_i let

$$\mathbf{S}_i = \begin{bmatrix} S_{i,0} & S_{i,1} \\ S_{i,1} & -S_{i,0} \end{bmatrix} = \begin{bmatrix} \int_\Omega \frac{1}{2}\left((\partial_y\phi_i)^2 - (\partial_x\phi_i)^2\right) & \int_\Omega -(\partial_x\phi_i)(\partial_y\phi_i) \\ \int_\Omega -(\partial_x\phi_i)(\partial_y\phi_i) & \int_\Omega \frac{1}{2}\left((\partial_x\phi_i)^2 - (\partial_y\phi_i)^2\right) \end{bmatrix} \tag{3.19}$$

which is by definition tracefree and symmetric. This geometrical Q-tensor was originally introduced in the context of flowing foams in [Asi+03] and later transferred to Phasefield models for cellular structures. We want to address the intuition behind this definition, in order to motivate its use in the construction of an active propulsive contribution.
As pointed out in Section 2.3, the eigenvectors of $\mathbf{S}_i$ form an orthonormal system with exactly two distinct eigenvalues. In particular the eigenvalues are given by

$$\lambda_i^{\pm} = \pm\sqrt{S_{i,0}^2 + S_{i,1}^2} \tag{3.20}$$

with corresponding eigenvectors

$$\eta_i^{\pm} = \begin{bmatrix} \frac{S_{i,0} + \lambda_i^{\pm}}{S_{i,1}} & 1 \end{bmatrix}^T. \tag{3.21}$$

In case $S_{i,1} = 0$ the tensor simplifies to

$$\mathbf{S}_i = \begin{bmatrix} S_{i,0} & 0 \\ 0 & -S_{i,0} \end{bmatrix}$$

and thus $\lambda_i^{1,2} = \pm S_{i,0}$ are eigenvalues. The eigenvectors are in this case given by the Euclidean standard basis vectors in $\mathbb{R}^2$ and the distinction between positive and negative depends on the sign of $S_{i,0}$.

FIGURE 3.11: Schematic visualization of the eigenvectors $\eta_i^{\pm}$ of $\mathbf{S}_i$ for different Phasefields ϕ_i represented by the levelset $\phi_i = 0$.

The eigenvectors η_i^+ and η_i^- according to (3.21) represent the axes of largest elongation and contraction, respectively, while the strength of deformation is given by the corresponding eigenvalues $\lambda_i^{\pm}$ in (3.20). More precisely, the axis of elongation is given by η_i^+. This is visualized in Figure 3.11 for different exemplary Phasefield shapes.
From this definition of the Q-tensor $\mathbf{S}_i$, representing the shape of each Phasefield ϕ_i, it is possible to define the global quantity

$$\mathbf{Q} = \sum_i \tilde{\phi}_i \mathbf{S}_i \tag{3.22}$$

using $\tilde{\phi}_i$, which results from ϕ_i by a rescaling to value range $[0, 1]$ according to (3.6). From this we define the tissue stress tensor

$$\boldsymbol{\text{œ}}_{tissue} = -\mathbf{Q},$$

inspired by the work in [MYD19]. Note that the definition $\boldsymbol{\text{œ}}_{tissue} = -PI - \mathbf{Q}$ was used in [MYD19] with P representing a passive pressure, given by the total variation of the system energy.
Using the tissue stress $\boldsymbol{\text{œ}}_{tissue}$, the activity of the system can be defined by

$$\mathbf{v}_i^{elo} = \int_\Omega \tilde{\phi}_i \nabla \cdot \boldsymbol{\text{œ}}_{tissue} = -\frac{1}{2} \int_\Omega \boldsymbol{\text{œ}}_{tissue} \cdot \nabla \phi_i. \tag{3.23}$$

The first variant expresses the propulsion to be the local force $\nabla \cdot \boldsymbol{\text{œ}}_{tissue}$, integrated over the cell interior, represented by the rescaled Phasefield $\tilde{\phi}_i$ while the second version models the tissue stress in outward normal direction $\nabla \phi_i$ for each cell.
The presented approach creates activity along the direction of elongation of a particular Phasefield and thus couples the motility directly to the deformation. In a sense this macroscopic description of the cell shape as underlying quantity for propulsion bridges the scales between a

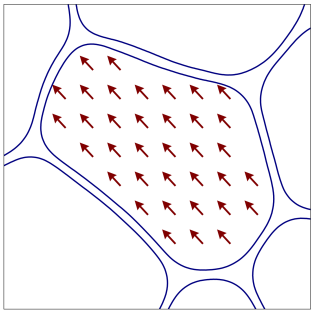

FIGURE 3.12: Schematic visualization of the levelset $\phi_i = 0$ and the elongation-based advection field $\mathbf{v}_i^{elo}$.

fully random advection as done in 3.4.1 and a more detailed description of the intracellular dynamics as introduced in 3.4.3 and 3.4.4. Numerically, it is a compromising way between detail and efficiency, as the computation of the global quantity $\mathbf{Q}$ is more costly than a strictly local definition of a random vector but in contrast to the models in 3.4.3 and 3.4.4 the energy only involves the Phasefields ϕ_i .
In the following, we want to introduce two different mechanisms for activity that both try to model the subcellular machinery with an additional quantity. In 3.4.3 we introduce a polar driven model and in 3.4.4 the approach considers active nematodynamics.

3.4.3 | Active Polar Gel Model

The next approach for the definition of a propulsion mechanism is motivated by polymerization and depolymerization of actin filaments inside of the cell, especially near the cell boundaries [Bea93; MO96]. We will model this microscopic effect in an averaged mesoscopic way by introducing an orientation field $\mathbf{P}_i$ for each cell, pointing from regions of depolymerization to regions of polymerization. Although $\mathbf{P}_i$ is defined on the whole domain Ω, we will use a model that enforces $\mathbf{P}_i$ to vanish outside of the cell interior.
To include $\mathbf{P}_i$ in our model, we introduce an Oseen-Frank energy contribution inspired by the description of liquid crystals [TMC12]. This approach was originally proposed in coupling with hydrodynamics in [MPV15]. The energy now depends on both the Phasefields ϕ_i and the polarization fields $\mathbf{P}_i$ and reads

$$\mathcal{E}_{POL}(\{\phi_i, \mathbf{P}_i\}) := \sum_{i=1}^{N} \int_\Omega \frac{1}{2}(\nabla \mathbf{P}_i)^2 - \frac{1}{2}|\mathbf{P}_i|^2 \left(\phi_i - \frac{1}{2}|\mathbf{P}_i|^2\right) + \beta \mathbf{P}_i \cdot \nabla \phi_i \mathrm{d}x. \tag{3.24}$$

The first term in equation (3.24) corresponds with the typical one-constant approximation known from Oseen-Frank descriptions of liquid crystal systems and models stiffness and elasticity. The second term restricts $\mathbf{P}_i$ to the interior of each Phasefield and ensures normalization. More precisely, outside the cell area ($\phi \approx -1$), the minimum is attained for $|\mathbf{P}_i| = 0$, i.e. vanishing polarization field. On the other hand, for $\phi \approx 1$, this forms a double-well with two minima satisfying $|\mathbf{P}_i| = 1$. The last term couples shape and polarization. In particular, it punishes deviations from an orthogonal direction of $\mathbf{P}_i$ on the cell interface, measured by $\mathbf{P}_i \cdot \nabla \phi_i$. We will later examine the effects of the coupling strength on the emerging behavior. In Chapters 4, 5 and 6, we will use an L_2 gradient flow for the evolution of $\mathbf{P}_i$ starting from random initializations, in order to allow for changes in the magnitude, adjusting to the normalization term in (3.24). Given the energy contribution for the polarization field and the resulting variational derivatives, which we will introduce later, the definition of propulsion is given by

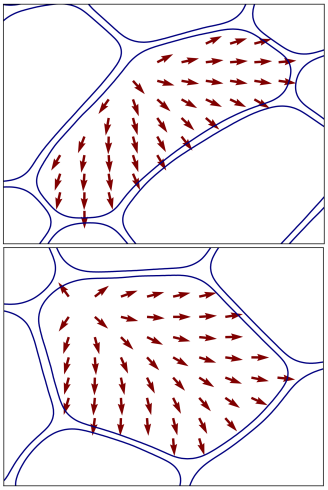

FIGURE 3.13: Schematic visualization of the levelset $\phi_i = 0$ and the polar advection field $\mathbf{v}_i^{pol}$ for two exemplary situations.

$$\mathbf{v}_i^{pol} = \mathbf{P}_i. \tag{3.25}$$

Note that $\mathbf{v}_i^{pol}$, in contrast to the previously defined $\mathbf{v}_i^{ran}$ and $\mathbf{v}_i^{elo}$, is not constant inside of the cell. The onset of motility results from a splay instability in the interplay between the outward orthogonal alignment enforced by $\mathbf{P}_i \cdot \nabla\phi_i$ and the smoothing effect of $(\nabla\mathbf{P}_i)^2$. This results in a shape-dependent $+1$ defect in the polarization field located away from the center and thus a dominating direction as visualized in Figure 3.13 for two different examples.
Compared to the random and elongation-based approach introduced in Subsections 3.4.1 and 3.4.2, it is possible to include much more detail using the non-constant polarization field. Furthermore, the coupling between shape and polarization, adjustable by choosing β, is more flexible than the elongation-based approach and can produce different phenomena, revealed for example in Chapter 4. On the other hand, the computational effort increases drastically by adding an additional quantity to the system, in particular a vector-valued function which will later on double the number of degrees of freedom.

3.4.4 | Active Nematic Model

The last approach we want to introduce in this section includes subcellular structure like the polar model in 3.4.3 but with an active nematic description. The motivation behind this lies in the key role of microtubules for cell motility as reviewed for example in [GS19; EM13]. These rod-like proteins without a distinct head or tail lead to movement in case of an asymmetric distribution inside of the cell as explained in [KS11a]. In order to describe the elongated, thin particles, we use the Q-tensor representation known from the description of liquid crystals. These materials with special order structure have been shortly introduced in Section 2.4. The active nematic propulsion has been used for particles given in a particle density formulation in [KV21] and in singular Phasefield simulations in [GD14; GL17].
For each cell, we include an additional tensor field $\mathbf{Q}_i$, which will by definition be tracefree and symmetric, i.e. a Q-tensor. As already mentioned in Section 2.4, the eigenvectors of $\mathbf{Q}_i$ give a mathematical representation of the elongated particles with head-tail symmetry (e.g. microtubules).
The energy contribution is captured using a Landau-de Gennes type formulation given by

$$\mathcal{E}_{NEM}(\{\phi_i, \mathbf{Q}_i\}) := \sum_{i=1}^{N} \int_\Omega \frac{1}{2}\|\nabla\mathbf{Q}_i\|^2 + \operatorname{tr}\mathbf{Q}_i^2(-\frac{1}{2}\phi_i + \frac{1}{4}\operatorname{tr}\mathbf{Q}_i^2) + \gamma\nabla\phi_i\mathbf{Q}_i\nabla\phi_i \,\mathrm{d}\mathbf{x}. \tag{3.26}$$

The structure of this energy is similar to $\mathcal{E}_{POL}$, introduced in Subsection 3.4.3. The first term enforces a smooth behavior, the second one restricts $\mathbf{Q}_i$ to the interior of the cell and the last term couples shapes and intracellular dynamics. While it is less obvious compared to the polar case, the last term in the energy, scaled with the parameter γ, again tries to enforce an orthogonal alignment near the cell boundary, in this case for the eigenvectors of $\mathbf{Q}_i$. Similar to the polar model in 3.4.3, we will in Chapters 5 and 6 use an L_2 gradient flow starting from a random initialization for the evolution of $\mathbf{Q}_i$.
The propulsion is defined similar to the elongation-based approach in Subsection 3.4.2 and given by

$$\mathbf{v}_i^{nem} = \nabla \cdot \mathbf{Q}_i. \tag{3.27}$$

We observe in Figure 3.14 (top) that the director field, given by the eigenvectors of $\mathbf{Q}_i$, resembles nematic alignments and forms two $+\frac{1}{2}$ defects near the most elongated points of the Phasefield, pointing outwards. The visualization in Figure 3.14 (bottom) shows that the advection field $\mathbf{v}_i^{nem}$ points along the directors of the defects, resulting in pulling forces which intensify elongations.

Comparing the computational effort of this approach with the previously discussed propulsion models, it may seem as the most complex choice due to the additional tensor-valued equation for $\mathbf{Q}_i$. However, due to the fact that $\mathbf{Q}_i$ is trace-free and symmetric, it can be represented by only two components which makes the model similar to the polar variant in terms of computational cost. The advantages of the approach are obvious and lie in the richness of details and possibility to include complex subcellular dynamics.

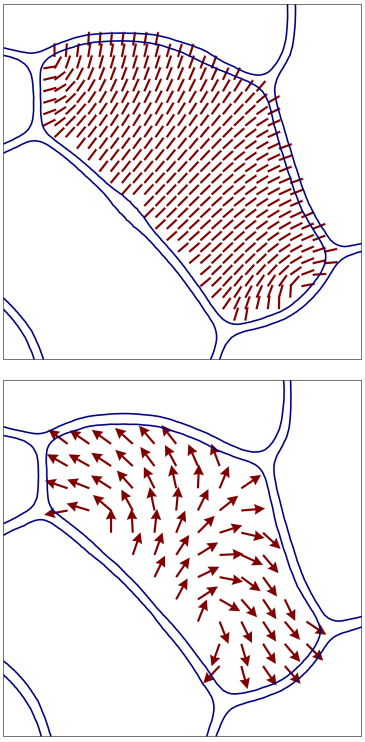

FIGURE 3.14: Schematic visualization of the levelset $\phi_i = 0$ with the eigenvectors of $\mathbf{Q}_i$ (top) and the resulting advection field $\mathbf{v}_i^{nem}$ (bottom).

In this section we have introduced 4 different approaches to define activity in our Multi-Phasefield models for cellular structures. Starting from a very simple random definition, we have considered an approach based on a global nematic elongation field and two variants incorporating subcellular dynamics, a polar and a nematic one. This gives rise to an extensive study of the effects of these propulsion mechanisms on the arising phenomena, which will be performed in Chapters 5 and 6. Of particular interest is the relevance of the single-cell dynamics on the occuring tissue-wide patterns in both movement and alignment.

3.5 | BOUNDARY CONDITIONS

In experimental studies on epithelial thin structure two setups dominate: either a very large, confluent monolayer is considered or a smaller, confined tissue which is restricted, for example, by the geometry of a petri dish or the underlying substrate. We want to create simulation setups for both variants.
The modeling of large cellular structures in a detailed description like the Multi-Phasefield approach is usually limited by computational resources. To ensure responsible use of those resources, we investigate all phenomena in confluence with a limited number of cells and periodic boundary conditions. This is a common way to imitate large-scale domains without unacceptably large computational effort.

To model the behavior of a confined system, different approaches are possible. One would be to be prescribe Dirichlet boundary conditions with the value -1, representing the exterior phase. Using this approach, Phasefields can freely move infinitesimaly close to the boundary without experiencing any repulsive forces. This is problematic for densely packed active systems where numerical instabilities occur as soon as cells are pushed towards to boundary.
We have, however, chosen a different approach, using the fact the all interaction potentials introduced in Section 3.3 include repulsive forces. More precisely, we want to use the repulsion dynamics used for cell-cell interactions also for cell-confinement interactions.
Let

$$\phi_{con}(\mathbf{x}) = \tanh\left(\frac{||\mathbf{x}-\mathbf{c}|| - r_{con}}{\sqrt{2}\epsilon}\right) \tag{3.28}$$

for $\mathbf{c}$ the center of the domain and r_{con} the designated radius of the confinement. The choice of $||\cdot||$ determines the confinement shape, where $||\cdot|| = ||\cdot||_\infty$ corresponds to a square confinement while the Euclidean norm $||\cdot|| = ||\cdot||_2$ represents circular shapes.

Then ϕ_{con} is a Phasefield type variable with $\phi_{con} \approx -1$ in the interior of the confinement and $\phi_{con} \approx 1$ in the exterior, which can be seen in Figure 3.15. Due to the fact that all interaction potentials are designed to keep other cells in the -1 phase, the sign of ϕ_{con} is inverted compared to standard Phasefield definitions.
The actual energy contribution from the confinement is then chosen to be consistent with the intercellular interaction potential. In practical, this means that in case of the distance-based interaction presented in Subsection 3.3.2, we introduce the energy

$$\mathcal{E}^d_{CON}(\{\phi_i\}) = \sum_{i=1}^{N} \int_\Omega B(\phi_i) w_E(d_{con}(x)) \mathrm{d}x \tag{3.29}$$

with B the usual surface delta approximation, w_E the exponentially repulsive potential and d_{con} the approximate signed-distance function for the confinement Phasefield. Using the quantitative Phasefield-based interaction from Subsection 3.3.3 on the other hand, the confinement energy is given by

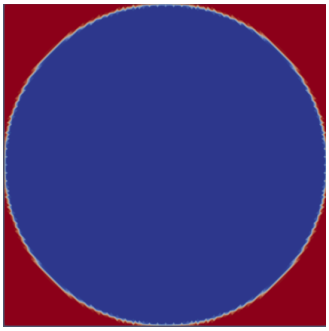

FIGURE 3.15: Visualization of the confinement Phasefield ϕ_{con} , constructed with $||\cdot||_2$. Blue color, representing $\phi_{con} \approx -1$, models the inside of the confinement and red color, visualizing $\phi_{con} \approx 1$, represents the outside.

$$\mathcal{E}^\phi_{CON}(\{\phi_i\}) = \sum_{i=1}^{N} \int_\Omega \tilde{\phi}_i w_{pol}(\phi_{con}(x)) \mathrm{d}x \tag{3.30}$$

with the parameter in the polynomial interaction potential chosen as $a = 1$, i.e. the purely repulsive variant.
We have introduced a modeling approach for confined systems, using the interaction mechanisms presented in Section 3.3. This has many advantages, for example similar choices of weighting parameters for interaction and confinement or the repulsive forces acting on a larger distance compared to the simple Dirichlet boundary conditions. The drawback is the necessity to resolve the grid fine enough, close to

the confinement boundary, which is in practical cases not problematic as the grid is already fine enough as soon as cells are actually approaching the boundary.

3.6 Implementation Details

All simulations performed for this thesis are based on a formulation of partial differential equations. While the particular system of equations will be given in the respective chapter, assembled in a modular way from different energy contributions, the general approach of implementation is preserved.
The models are implemented in AMDiS (*Adaptive Multidimensional Simulations*), a C++ framework originally developed and permanently optimized by members of the Institute of Scientific Computing at TU Dresden. More details on the software can be found in [VV07b; VV07a; VW12; Wit+15] and the repository is available for access at [Pra+].
For time discretization a typical explicit-implicit strategy is used. In particular, all linear operators are assembled implicitly. Non-local contributions of non-linear terms, e.g. from the interaction given in (3.11), are treated explicitly for reasons of communication efficiency in the parallel implementation, see 3.6.1. Local non-linear terms, e.g. from the double-well potential in (3.1), are linearized using a Taylor expansion of order 1 that reads

$$W'(\phi_{new}) \approx W'(\phi_{old}) + (\phi_{new} - \phi_{old})W''(\phi_{old}),$$

applying non-linear functions exclusely to values from the old timestep. In total this creates a linear system, enabling the use of standard linear solvers.

3.6.1 Parallelization

The simulation of possibly large numbers of Phasefield evolutions, in some cases even coupled with additional vector or tensor fields (see 3.4.3 and 3.4.4), is a computationally challenging task. The grid used for the simulations, is required to resolve the diffuse interface region of every Phasefield sufficiently well, to ensure numerical stability of the phases. Defining a single grid that simultaneously resolves all interface regions fine enough, would lead to unacceptably large numbers of degrees of freedom. Furthermore, including all individual contributions in one system of equations would result in a discrete system, scaling with the number of cells, while actually the coupling only results from intercellular interactions. Combining these two problems, it becomes obvious that this approach is not practically doable for larger numbers of cells.

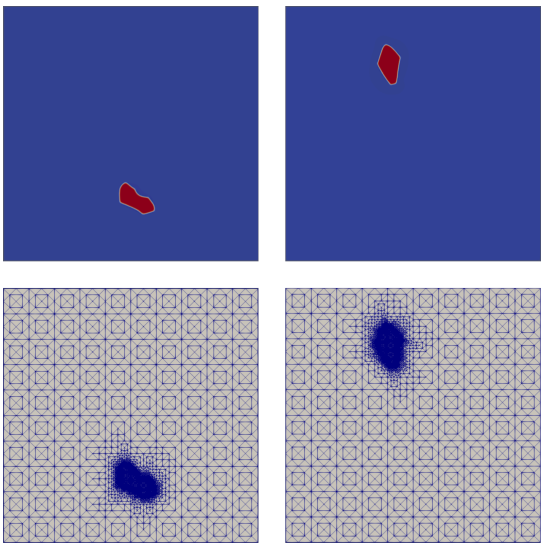

FIGURE 3.16: Two examples of Phasefields with color map from red ($\phi \approx 1$) to blue ($\phi \approx -1$) at the same time (top) alongside the locally refined grids (bottom).

We use a cell-based parallelization approach with `MPI` that was originally proposed

in [PV18]. The key idea is to consider each cell, represented by ϕ_i, individually on a single core of the CPU, with a grid locally refined according to the interior and interface of ϕ_i. This results in a local problem on each core that requires solving a small system of equations (2 - 4, depending on the propulsion mechanism) with a moderate number of degrees of freedom. In Figure 3.16, we observe that the strictly local properties of the Phasefields, which are constant in most of the domain, transfer to the grid structure perfectly with coarse resolution far away from the cell interior and fine grid inside the diffuse interface.
For large cell numbers, however, the communication of the intercellular interaction could lead to an additional bottleneck. This problem can be solved, keeping in mind that all interactions, inspired by intercellular mechanisms in real tissue, have a very short range. In particular, we remember Figures 3.8 and 3.9 that indicate how all approaches for interaction vanish for cellular distances in the magnitude of ϵ, i.e. small compared to the domain sizes. The computation and communication of interaction terms, as a consequence, is done only for the nearest neighbors, where the term near is defined using a heuristic based on the centers of mass for all cells.
The combination of these two aspects - solving every system locally on a single core of the CPU and communicating interactions only with closest neighbors - results in a great scaling behavior with more details reported in [PV18].

3.6.2 | INITIALIZATION

One huge advantage of Phasefield models, compared to simpler approaches like particle models is the flexibility in shapes. As a consequence, much higher packing fractions are possible. In case of volume-preserving models as used in Chapters 4, 5 and 6 it is, however, necessary to initialize the structure already with the designated packing fraction. In all cases, we will choose initial shapes with analytically given signed distance functions and compute the Phasefield from those. Furthermore, in all approaches presented here we define initial conditions for a full packing and then afterwards shrink the individual Phasefields by a constant factor to ensure that the diffuse interfaces of different cells will not overlap.

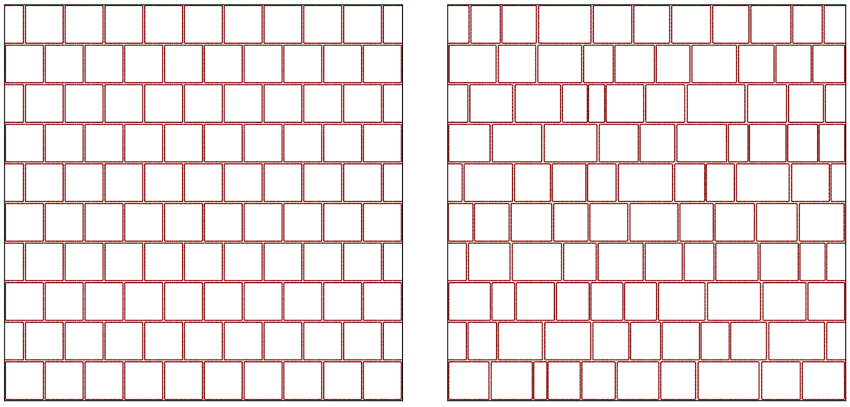

FIGURE 3.17: Visualization of densely packed initial conditions used in this thesis for confluent setups with periodic boundary conditions. Each cell is represented by the levelset $\phi_i = 0$.

According to the observations in Section 3.5 about the boundary conditions, we create initial conditions for both periodic and confined settings. The setups for periodic boundaries are shown in Figure 3.17. The most basic situation is given for equally

sized cells in a $2D$ square (or potentially rectangular) domain and visualized in Figure 3.17 (Left). We use a structure inspired by brick walls where the initial shapes are chosen rectangular with half a cell width shift in every second row. This approach already establishes the optimal hexagonal packing and is used in Chapters 5 and 6. For the studies performed in Chapter 4 differences in cell size are necessary. We use a normal distribution of cell widths in each row of the brick wall while keeping the height of the rows constant as visualized in Figure 3.17 (Right). More precisely, in a row with N cells the first $N-1$ sizes have widths according to a normal distribution while the last one gets the remaining size to ensure full packing.

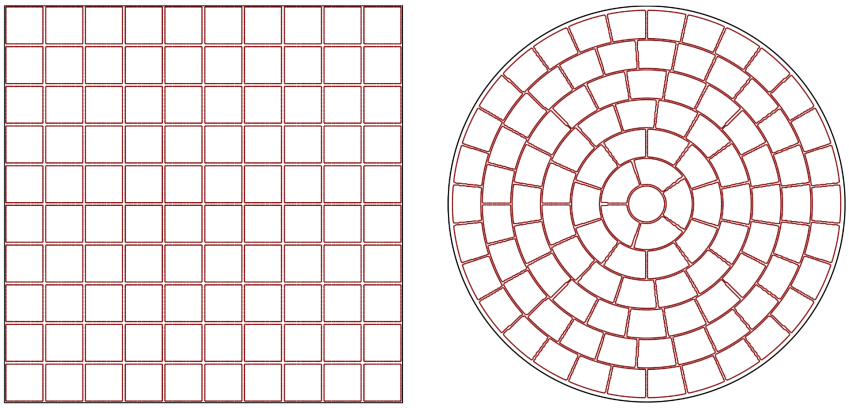

FIGURE 3.18: Visualization of densely packed initial conditions in rectangular (Left) and circular (Right) confinement. Each cell is represented by the levelset $\phi_i = 0$.

To perform studies in confinement, the initially created Phasefields should not cross the domain boundaries. For rectangular confinements we use the setup visualized in Figure 3.18 (Left). It is similar to the construction in Figure 3.17 (Left) but the row-wise shift is omitted. For the circular confinement used in Chapter 5, we have constructed an initial packing inside of the circle as shown in Figure 3.18 (Right). In particular almost all initial shapes are curved trapezoidals, aligned in radial rings of fixed size with one round cell in the center of the domain.

The initial conditions presented in this section involve shapes that are far from reality in biological systems. Hence, it is always necessary to exclude a certain number of timesteps after initialization from the actual observations during which the influence of the Cahn-Hilliard energy deforms the cell.

4 | Topological and Geometrical Quantities in Cellular Structures

The first step towards an understanding how Multi-Phasefield models can be used for the description of cellular structures, is to analyze the topology and ordering of the systems. This can also be seen as a prior step on the road towards experimental validation, as we will compare our findings mostly with other models and less with biological data due to the lack of quantitative measurements for cellular systems. One particular focus will be the investigation of the influence that the induced activity has on observables like topology and geometrical ordering.

Although driven and active systems are far from equilibrium, they have been shown to share key features with passive systems. Examples are effective thermal behavior and time correlation functions in assemblies of cells, which behave as equilibrium glass transitions [BK13; BT09] or motility induced phase separation, which shares properties such as coarsening laws and statistical self-similarity with classical phase separation in binary systems [Wit+14; Spe+14]. Certain topological and geometrical quantities are well studied for passive systems like foams and froths [Fly93; DBV11] or Ostwald ripening of minority phase domains after a rapid temperature quench [Voo85; MAL19]. We will here test if those quantities are also valid for *in silico* experiments on monolayers of cells.
We will consider two empirical laws. The first one is Lewis' law, originally proposed in studies of the epidermis of Cucumis [Lew28], which expresses the existence of a correlation between area and number of neighbors (coordination number q) of a cell. The second one is Aboav-Weaire's law, with the original aim to understand the mechanism of growth of polycrystals [Abo70], which states that cells with high (low) coordination number are surrounded by small (large) cells. In other words, Lewis's law indicates how space is most likely to be filled by cells, whereas Aboav-Weaire's law gives the most probable correlation between neighboring cells. Both laws for space-filling cellular structures can be found in biological, geographical, mathematical and physical literature, see e.g. [Chi95] for a review. Such topological properties find a rapidly growing interest in studying the interplay between mechanics and the

collective behavior of cells on the tissue level [LM17].

The chapter is organized as follows: In Section 4.1, we assemble the considered model from the individual components presented in Chapter 3. In particular, we focus on the mechanism of activity, namely the polar model introduced in 3.4.3. In Section 4.2, the model is used to analyze the occurrence of typical topological phenomena like T1 transitions and rosettes. Afterwards, in Section 4.3, we investigate the coordination of cellular movements and the creation of collective motion. In Section 4.4, we compare geometrical properties like the distribution of coordination numbers. In Section 4.5, we investigate the equilibrium Lewis' and Aboav-Weaire's laws depending on two essential parameters, based on the observations in the previous sections. We thereby demonstrate the possibility to classify cellular systems according to their collective behavior. In Section 4.6, we draw conclusions and give an outlook to the following chapters.

4.1 | Model Setup

In this chapter, we restrict our considerations to the Multi-Phasefield model with polar propulsion mechanism and distance-based interaction in a periodic setting. These active polar Phasefield models have been previously investigated in [KJ00; Kru+04; MPV15] and a similar interaction was used in [MV16].
We consider $i = 1, \dots, N$ individual Phasefields $\{\phi_i\}_{i=1,\dots,N}$ and the corresponding polarization fields $\{\mathbf{P}_i\}_{i=1,\dots,N}$. The total energy of the system is assembled as

$$\mathcal{E}\left(\{\phi_i, \mathbf{P}_i\}\right) = \frac{1}{Ca}\mathcal{E}_{CH}\left(\{\phi_i\}\right) + \frac{1}{In}\mathcal{E}^d_{INT}\left(\{\phi_i\}\right) + \frac{1}{Pa}\mathcal{E}_{POL}\left(\{\phi_i, \mathbf{P}_i\}\right) \tag{4.1}$$

with

$$\mathcal{E}_{CH}\left(\{\phi_i\}_{i=1}^N\right) = \sum_{i=1}^N \int_\Omega \frac{\epsilon}{2}|\nabla\phi_i|^2 + \frac{1}{\epsilon}W(\phi_i)\mathrm{d}x$$

the Multi-Phasefield Cahn-Hilliard energy as introduced in (3.5),

$$\mathcal{E}^d_{INT}(\{\phi_i\}) = \sum_{i=1}^N \sum_{j\neq i} \int_\Omega B(\phi_i) w_E(d_j(x))\mathrm{d}x$$

the distance-based interaction as defined in (3.11) using the exponentially repulsive potential in (3.12) and

$$\mathcal{E}_{POL}(\{\phi_i, \mathbf{P}_i\}) := \sum_{i=1}^N \int_\Omega \frac{1}{2}(\nabla\mathbf{P}_i)^2 - \frac{1}{2}|\mathbf{P}_i|^2\left(\phi_i - \frac{1}{2}|\mathbf{P}_i|^2\right) + \beta\mathbf{P}_i\cdot\nabla\phi_i\mathrm{d}x$$

the polar energy introduced in (3.24). To balance the individual contributions to the total energy, we use the dimensionless weight parameters Ca, In and Pa as motivated in [MV16]. To derive the evolution equations for all ϕ_i and $\mathbf{P}_i$, we use the gradient flow approach presented in 2.2. In particular we use the volume-preserving H^{-1} gradient flow for each Phasefield, given by

$$\partial_t\phi_i = M\Delta\frac{\delta\mathcal{E}}{\delta\phi_i},$$

using a mobility M in combination with the polar propulsion $\nabla \cdot (\phi_i \mathbf{P}_i)$. The evolution equations for ϕ_i thus read

$$\begin{aligned} \partial_t \phi_i + v_0 \nabla \cdot (\phi_i \mathbf{P}_i) &= M \Delta \mu_i \,, \\ \mu_i := \frac{\delta \mathcal{E}}{\delta \phi_i} &= \frac{1}{Ca} \left(-\epsilon \Delta \phi_i + \frac{1}{\epsilon} W'(\phi_i) \right) \\ &+ \frac{1}{Pa} \left(-\frac{1}{2} \|\mathbf{P}_i\|^2 - \beta \nabla \cdot \mathbf{P}_i \right) \\ &+ \frac{1}{In} \left(B'(\phi_i) \sum_{j \neq i} w_E(d_j) + w_E'(d_i) d_i'(\phi_i) \sum_{j \neq i} B(\phi_j) \right). \end{aligned} \tag{4.2}$$

To derive the evolution equations for $\mathbf{P}_i$, we use the non-preserving L_2 gradient flow

$$\partial_t \mathbf{P}_i = -\frac{\delta \mathcal{E}}{\delta \mathbf{P}_i},$$

in order to allow for changes in the magnitude of $\mathbf{P}_i$, according to the normalizing and restricting energy contributions in $\mathcal{E}_{POL}$. The evolution equations read

$$\partial_t \mathbf{P}_i + \big(v_0 \mathbf{P}_i \cdot \nabla\big) \mathbf{P}_i = -\frac{1}{Pa} \Big(-\phi_i \mathbf{P}_i + \|\mathbf{P}_i\|^2 \mathbf{P}_i - \Delta \mathbf{P}_i + \beta \nabla \phi_i \Big). \tag{4.3}$$

where the non-linear self-advection term $\big(v_0 \mathbf{P}_i \cdot \nabla\big) \mathbf{P}_i$ was added for thermodynamic consistency, see [TMC12; MPV15; MV16] for details. We have, however, observed that this term does not influence the qualitative behavior of the system and thus remove it in Chapters 5 and 6.

Both equations are defined in $\Omega \times (0, T]$ for some simulation end time $T > 0$ and a two-dimensional domain $\Omega \subset \mathbb{R}^2$. We assume in the following periodic boundary conditions for Ω, to represent a large confluent monolayer, as motivated in Section 3.5. We solve these equations numerically, using the Finite-Element framework AMDiS, see Section 3.6 and make use of the cell-based parallelization approach described in Subsection 3.6.1. The local grid on each CPU process is refined according to the individual Phasefield ϕ_i, in particular with a spacing of $h \approx 0.2\epsilon$ inside the diffuse interface while $h \leq \epsilon$ in the interior region ($\phi_i \approx 1$) and $h \leq 10\epsilon$ in the exterior ($\phi_i \approx -1$). Due to the local refinements and recursive grid regularization, the spacing increases for larger distances from the cell interior. After very few initial time steps used to let the shapes relax after initialization, the time step size is chosen to be $\tau = 0.1$.

Previous studies of the model were concerned with dilute monodisperse systems and the emergence of collective motion [MV16; PV18]. We here consider densely packed disperse systems where different model parameters are varied to analyze the effect on topological and geometric quantities of the active cellular structures.

Ω	ϵ	M	Pa	Ca	In
$[0, 100] \times [0, 100]$	0.15	1	1	0.025	0.05

TABLE 4.1: Numerical parameters used in all simulations throughout Chapter 4.

For the normal distribution in the cell size, as introduced in Subsection 3.6.2, and depicted in Figure 3.17 (Right), we use the variance $\sigma = 3$. As already mentioned,

due to the Phasefield approach with diffuse interfaces and $\epsilon > 0$, a fully space-filling structure is not possible. We instead consider an area fraction of 0.95, achieved by a shrinkage of each cell, which explains the visible empty space in Figures 4.1 and 4.2. We vary the parameter β, which models the anchoring of the polarization field at the cell boundaries, as explained in 3.4.3, and the parameter v_0, which scales the strength of self-propulsion. When studying the influence of β, we choose $v_0 = 2.5$ and in the study of v_0, we fix $\beta = 0.3$. All other parameters are fixed over all simulations, see Table 4.1 for the considered values.

4.2 | Topological Properties

For developmental processes, different types of reordering are necessary and have been observed to occur in tissue. One example are the so-called T1 transitions, where one pair of neighboring cells detaches, while simultaneously a new pair forms, which has to be incorporated manually in vertex models like [FRA07]. This is problematic, as it brings some type of externally enforced determinism into an otherwise intrinsically driven procedure. Multi-Phasefield models on the other hand, due to their nature of describing each cell individually with cellular bonds only given implicitly, create these transitions naturally. This can be observed in Figure 4.1 and gives a huge advantage of the models considered throughout this thesis in comparison with other mesoscopic descriptions of cellular structures like vertex models.

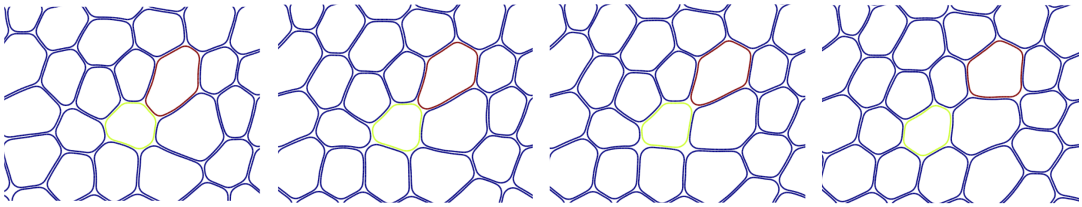

FIGURE 4.1: Typical T1 transition. The color highlights the involved cells in the topological change which are in contact with each other at the beginning of the T1 transition.

It has been observed that points where four or more cells are in contact, the so called rosettes, are of crucial importance for the development of tissue, as reviewed in [HMN14]. In particular, they have been shown to play a crucial role in Drosophila eye development as observed in [EBF07; Rob+12] and the formation of the Zebrafish lateral line, see [HG06; HN12] for details. While rosettes also have to be enforced artificially in vertex models like [YB18], they occur naturally in Multi-Phasefield models. Figure 4.2 shows typical examples for rosettes occurring in our simulations.
More quantitative studies on the occurrence of rosettes and their relative number, compared to vertices with 3 cells, will be performed in Chapter 5 for different mechanisms of propulsion.

4.3 | Coordinated Activity and Collective Motion

It has been studied in a wide range of organisms, how the individual motion patterns of cells correlate on a larger scale. A variety of reviewing articles exists on this subject, for example [MV14b].
One interesting phenomenon, observed for example in bird embryos (see [Sat+10])

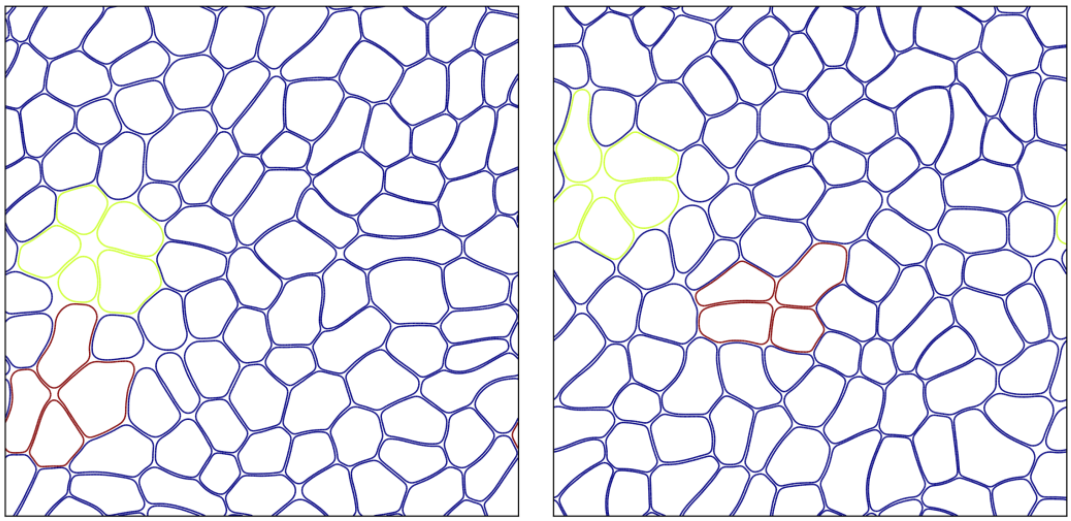

FIGURE 4.2: Examples for rosettes found in the simulations. The color highlights "vertices" with four (red) or five (green) cells.

and also lymph nodes (see [Bel+07]), is the so-called streaming in monolayers. While on a larger scale no flocking occurs, local correlations in the movements can be observed, resembling turbulent flow patterns. In Chapter 5, we will give more insight into these dynamics in Multi-Phasefield models with different mechanisms of propulsion.
On the other hand, Madine Darby Canine Kidney (MDCK) cells have been observed to form a global flocking behavior in certain circumstances, with all cells moving in the same direction. In [Pou+07], an experiment was performed imitating the occurrence of a wound by plating a confluent epithelium on a free surface without damaging individual cells. Interestingly, the availability of surface has proven to be sufficient for inducing collective motion on a large scale. This indicates that the internal cell machinery, in a large colony, self-enhances alignment of motion. We want to investigate, whether this phenomenon can be reproduced in our computational model and how it depends on the choice of model parameters.
We measure the individual movement direction in terms of the polarization field $\mathbf{P}_i$ of each cell, which is the source of activity in the system. Alternatively, one could also consider the actual direction of motion of the Phasefield ϕ_i. This approach, however, has been observed to create a much stronger noise as individual cells in densely packed epithelium can never move freely. More precisely, we compute the average polarization of a single cell by

$$\overline{\mathbf{P}}_i := \frac{\int_\Omega \mathbf{P}_i \, (\phi_i + 1) \, \mathrm{d}\mathbf{x}}{\int_\Omega (\phi_i + 1) \, \mathrm{d}\mathbf{x}}, \tag{4.4}$$

for each snapshot in time. The averaging procedure is visualized in Figure 4.3. Shown are the zero-level lines of ϕ_i (cell boundaries of each cell). The red arrows in the pictures left and right visualize $\mathbf{P}_i$ for two exemplary cells while the blue arrows in the middle frame depict $\overline{\mathbf{P}}_i$ for all shown cells.

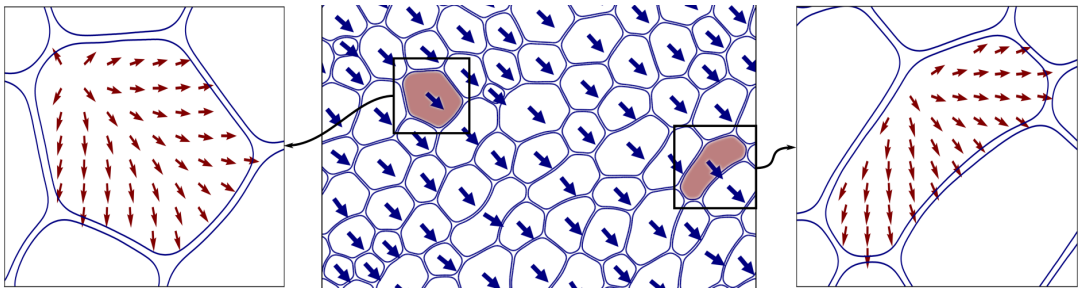

FIGURE 4.3: Examples of $\overline{\mathbf{P}}_i$ (middle) as average of $\mathbf{P}_i$ (left,right).

We start by fixing a single set of parameters, namely $\beta = 0.3$ and $v_0 = 2.5$ and investigating the time-dependent evolution of the average polarization for all cells in the epithelium. Figure 4.4 shows snapshots of the evolution of the cellular structure with arrows indicating $\overline{\mathbf{P}}_i$ for all cells.

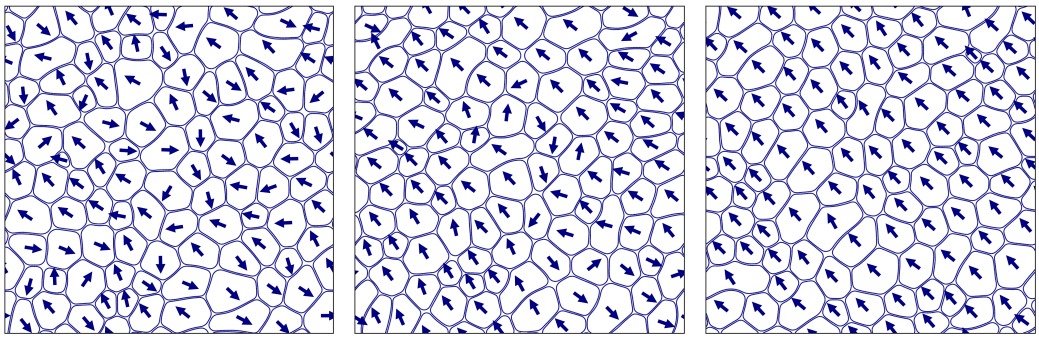

FIGURE 4.4: Snapshots of the evolution for $t = 60, 225, 800$ from left to right. The simulation is done with $\beta = 0.3$, $v_0 = 2.5$ and a random initialization of the polarization field. Shown are the $\phi_i = 0$ levelsets, superimposed with the average polarization $\overline{\mathbf{P}}_i$. From left to right, we observe the time-dependent development towards a state of collective motion.

From Figure 4.4, we can conclude that for the chosen parameter values for β and v_0 indeed a global flocking evolves. In order to investigate this further, we introduce the translational order parameter

$$\theta(t) = \frac{1}{n} \left\| \sum_i \overline{\mathbf{P}}_i(t) \right\|$$

according to [LZA15a; APV16]. It is 1 if all cells move in the same direction and 0 if all cell polarizations and thus movements are independent. We want to investigate the influence of the coupling parameter β and the activity strength v_0 on the evolution of θ.

In particular, we use the threshold $0.9 < \theta$ to classify a state of global collective motion or flocking, see [TT98; TTR05]. Figure 4.5 shows the evolution of the order parameter θ for different initial conditions and different β with fixed $v_0 = 2.5$. For $\beta = 0.3$, a state of collective motion is reached almost immediately, whereas for $\beta = 0.1$ this state is never reached within the considered time T and one could conclude that it will probably never be reached. For $\beta = 0.2$, it takes a long time before collective motion can be observed. Depending on the initial conditions, it might not even be reached within the considered time. Note that both the final time and the

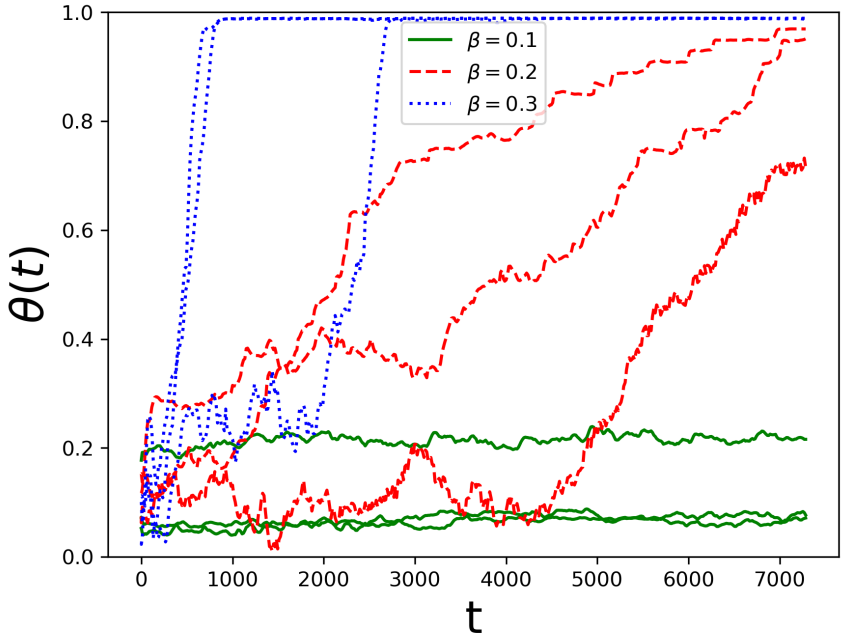

FIGURE 4.5: Translational order parameter $\theta(t)$ indicating collective motion for increasing values of β with fixed $v_0 = 2.5$. The time is considered in non-dimensional units.

number of performed simulations are a compromise between predictability and economic use of computing resources.
Figure 4.6 on the other hand shows the evolution of θ with different values of v_0 but fixed $\beta = 0.3$. In comparison to $v_0 = 2.5$, we observe that for the slightly increased value $v_0 = 3.5$ the system still reaches a collective state after relatively short time, although oscillations in the translational ordering are strengthened. Upon increasing the activity further to $v_0 = 5.0$, no simulation showed collective motion in the considered time T and oscillations in θ are increased even more. Even though in the state of high activity no global flocking is observed, the values of θ are still significantly larger than 0, so the system is not in a fully disordered state. A possible explanation is the occurrence of more local correlations in the polarization fields, which can be associated with the aforementioned phenomenon of streaming.
In conclusion, we have observed that a sufficiently strong coupling of shape and polarization by the parameter β is necessary to ensure the occurrence of globally collective motion. For high levels of activity, induced by increasing v_0, the systems do not evolve a stable state of flocking but instead show a more turbulent behavior resembling the phenomenon of streaming. These findings are in qualitative agreement with results obtained for more dilute systems [PV18].

4.4 | NEIGHBORING RELATIONS AND COORDINATION NUMBER

The number of neighbors, i.e. cells that are close enough to form intercellular junctions, is influenced by different individual factors: the cell density (packing fraction), the tension of the cell surface (higher deformations potentially allow more neighbors) and also the level of activity. We will leave the first two contributions out of focus at this point, as we are only interested in cellular systems at a state of high

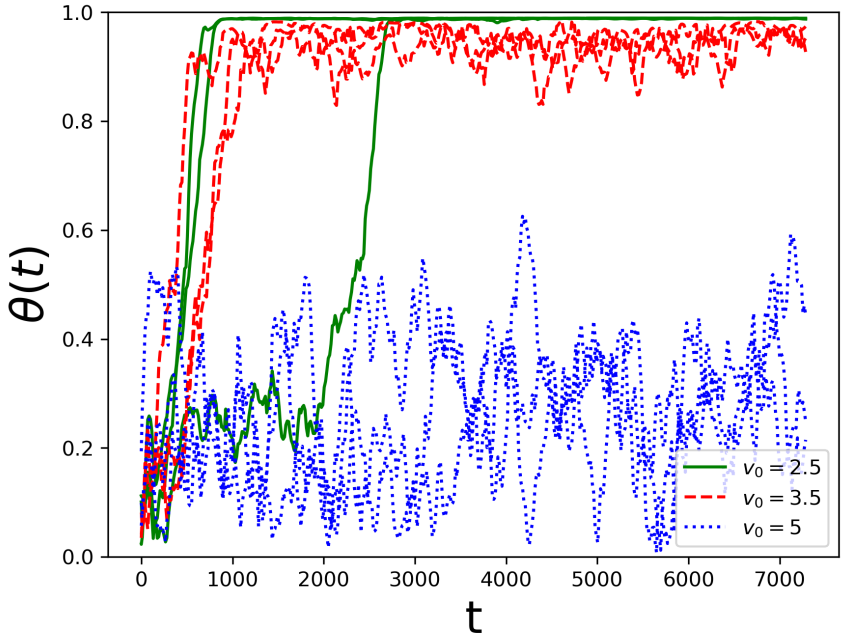

FIGURE 4.6: Translational order parameter $\theta(t)$ indicating collective motion for increasing values of v_0 with fixed $\beta = 0.3$. For high activity the system evolves a turbulent state. The time is considered in non-dimensional units.

packing fraction, usually called confluency, and with approximately constant physical properties like surface tension, in our case implicitly represented by the capillary number Ca.

While the optimal packing of equal-sized cells is known to be a honeycomb-type structure, where each cell is approximately hexagonal in shape with exactly 6 neighbors, this is not the case in most practical examples. It has, however, been observed that usually a normal distribution with mean value of approximately 6 evolves, see e.g. [Rup+17] for studies in Drosophila.

We investigate if our computational model shows a similar behavior and in particular how the level of activity influences this distribution. For this, we will study the influence of varying both the shape-polarization coupling parameter β and the self-propulsion velocity v_0. While in experimental setups the identification of neighbors is rather non-trivial and requires complex image-processing techniques, it is much simpler in the Multi-Phasefield approach.

The short-range interaction potential w_E, used in the definition of the model, automatically detects if two cells are close to each other. As a consequence the criterium

$$\int_\Omega B(\phi_i) w(d_j) > 0$$

states if cells i and j are neighbors. This is computed during run-time anyways and causes no additional computational cost.

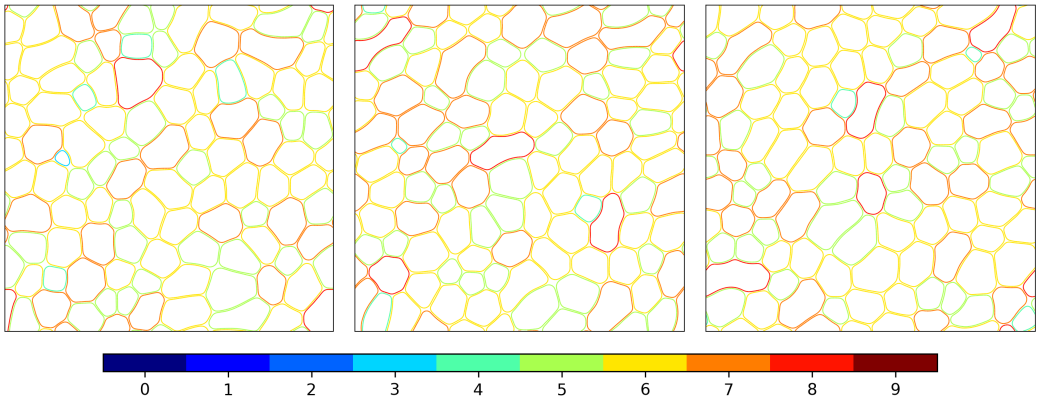

FIGURE 4.7: Snapshots of the cellular for $t = 60, 225, 800$ from left to right. The simulation is done with $\beta = 0.3$, $v_0 = 2.5$ and a random initialization of the polarization field. The color coding shows the number of neighbors of a cell.

Figure 4.7 hints that indeed a majority of cells has 6 neighbors but we can also observe that a significant amount of cells has other coordination numbers. In order to quantify this, we introduce the empirical probability $P(q) = N(q)/N$, where $N(q)$ is the number of cells with q neighboring cells and $N = \sum_q N(q)$. Interesting quantities are the mean value $\mathbb{E}[P(q)]$, which is predicted to be around 6, independent of the simulation setup, and the variance $\mu_2[P(q)] = \sum_q (q - \mathbb{E}[P(q)])^2 P(q)$. Unfortunately, no quantitative data for real epithelial structures was available and hence the simulation results in [SS95], given for passive systems, were chosen as quantitative reference.

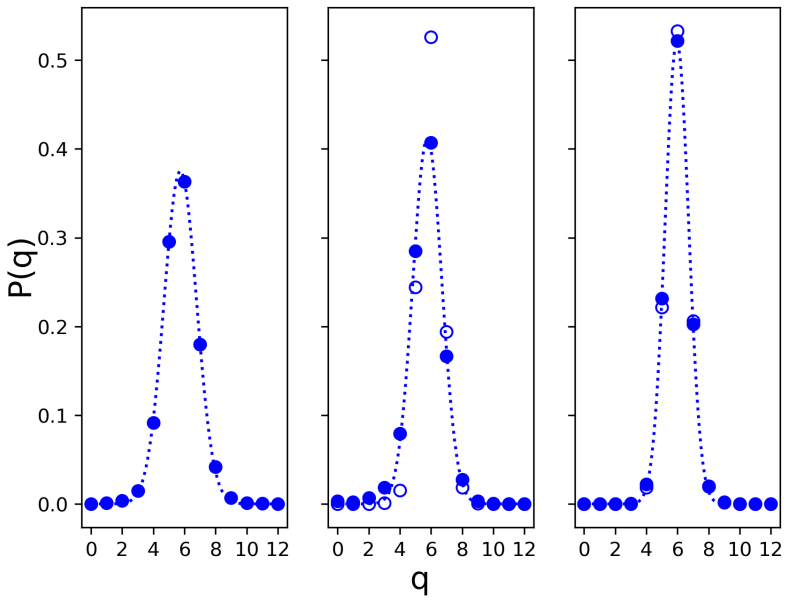

FIGURE 4.8: Coordination number probability for $\beta = 0.1, 0.2, 0.3$ with fixed $v_0 = 2.5$ from left to right. Shown is the average of the whole time evolution and all considered samples (closed symbols and fit) and average over the time, where collective motion is already reached ($0.9 < \theta$) (open symbols).

We have varied the parameter $\beta \in [0.1, 0.2, 0.3]$ for constant $v_0 = 2.5$ and performed three simulations for each setup. Recalling the results in Figure 4.5, the simulations for higher values of β reach a state of somewhat collective motion at a certain time. To account for this, we have computed $P(q)$ for all timesteps and also for those timesteps where $0.9 < \theta$ holds. The results in Figure 4.8 show that indeed all setups show a mean value $\mathbb{E}[P(q)] \approx 6$ and an approximately symmetric distribution. For the variance we obtain $\mu_2[P(q)] = \sum_q (q-6)^2 P(q) \approx \{1.05; 0.94; 0.76\}$ for $\beta = 0.1; 0.2; 0.3$, respectively. Considering for $\beta = 0.2$ only the time, where collective motion is reached, which is identified by $0.9 < \theta$, we obtain $\mu_2 = 0.75$.

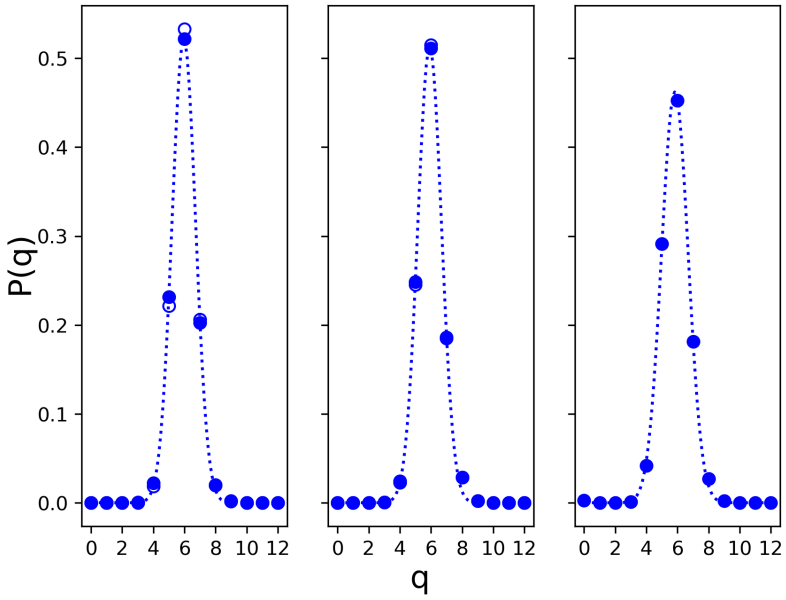

FIGURE 4.9: Coordination number probability for $v_0 = 2.5, 3.5, 5.0$ with fixed $\beta = 0.3$ from left to right. Shown is the average of the whole time evolution and all considered samples (closed symbols and fit) and average over the time, where collective motion is already reached ($0.9 < \theta$) (open symbols).

On the other hand, we have varied $v_0 \in [2.5, 3.5, 5.0]$ for a constant value of $\beta = 0.3$ and performed again three independent simulations for each setup. The results in Figure 4.9 show again a symmetric distribution centered at $\mathbb{E}[P(q)] \approx 6$, independent of the parameter v_0. Furthermore, we observe a slight increase in $\mu_2[P(q)]$ for increasing self-propulsion. In particular we obtain $\mu_2 \approx \{0.76, 0.77, 0.86\}$ for $v_0 = 2.5; 3.5; 5.0$, respectively.

We can conclude that the results are in general qualitative agreement with both experimental data for MDCK cells found in [Kal18] or [SG+16] (only visual results available) and also simulation data from passive systems as reported in [SS95]. All setups show a symmetric distribution centered at a mean value of $\mathbb{E}[P(q)] \approx 6$. If our system is in a state of collective motion, e.g. for $v_0 = 2.5$ and $\beta = 0.3$ as depicted in Figure 4.8 (right), the values for the variance $\mu_2[P(q)]$ are even in qualitative agreement with [SS95], where $\mu_2 = 0.64$ has been reported. This indicates that, in terms of coordination numbers and neighboring structures, a globally collectively moving system behaves effectively passive.

4.5 | CELLULAR ORGANISATION DRIVEN BY SIZE AND SHAPE

The self-organization evolving in cellular structure like epithelium has been a topic of huge interest for decades. The fundamental question is, whether the distributions of cell shapes, coordination numbers and sizes are purely driven by geometry and topology - and thus the minimization of a certain system energy - or if some higher intercellular communication and ordering is involved. We do not claim to answer this question but we do, however, investigate the fulfillment of geometrical laws known for biological systems in our model.
Of particular interest for almost a century has been Lewis's law, originally proposed in [Lew28] based on observations in Cucumis. It reads

$$\frac{\overline{A}(q)}{\overline{A}} = \alpha(q-6) + \gamma \tag{4.5}$$

with $\overline{A}(q)$ the average area of q-coordinated cells, $\overline{A}$ the overall average cell area and α and γ scalar fitting parameters. Qualitatively, this means that cells with a coordination number $q = 6$ tend to have a size equal to the average cell size while cells that are larger (smaller) than the average cell size tend to have a coordination number larger (smaller) than six.
Experimental results for different organism, e.g. Drosophila, in [SG+16] have shown that Lewis' law is not only true for plant cells like Cucumis (original work in [Lew28]) but also holds in animal tissue. In order to identify these neighboring relations *in vitro*, an identification of tissue as networks, originally proposed in [Esc+11] was used.
While Lewis' law originated from the context of plant cells and can intuitively be explained easily, the relevance of the so-called Aboave-Weaire's law is less obvious. Originally introduced in [Abo70] and [Wea74], in the context of polycrystals, it quantifies the relation between the coordination number q of a particle and the coordination number of its neighbors $p_{nn}(q)$ and reads

$$q\overline{p}_{nn}(q) = (6-\zeta)(q-6) + \eta \tag{4.6}$$

with scalar fitting parameters ζ and η. Practically, Aboav-Weaire's law states that cells with high coordination number are surrounded by cells with a small coordination number, with a linear dependence.
In current research, it has been observed that this law from material sciences holds also in plant tissue, see e.g. [JB02]. More recently, experiments in Drosophila, as done in [Esc+11] and [SG+16], have revealed that Aboav-Weaire's law is also fulfilled for animal tissue in certain cases.
The combination of both Lewis's law and Aboav-Weaire's law leads to a correlation between the area of a cell, A, and the average area of its neighbors, $\overline{A}_{nn}$, see Figure 4.10. Cells which are larger (smaller) than the average cell size are mostly surrounded by neighbor cells that are smaller (larger) in size. The functional form for this relation is given by

$$f(x) = \frac{1}{x}\left(1 + \frac{\alpha^2\mu_2 - \zeta\alpha(x-1)}{6\alpha + (x-1)}\right) \tag{4.7}$$

with $x = A/\bar{A}$ and $f(x) = \bar{A}_{nn}/A$ and the fitting data α from Lewis's law, ζ from Aboav-Weaire's laws and μ_2 the variance of $P(q)$ as computed in Section 4.4. The law

results from maximum entropy theory for random two-dimensional cellular structures [PSR91; SMS94].

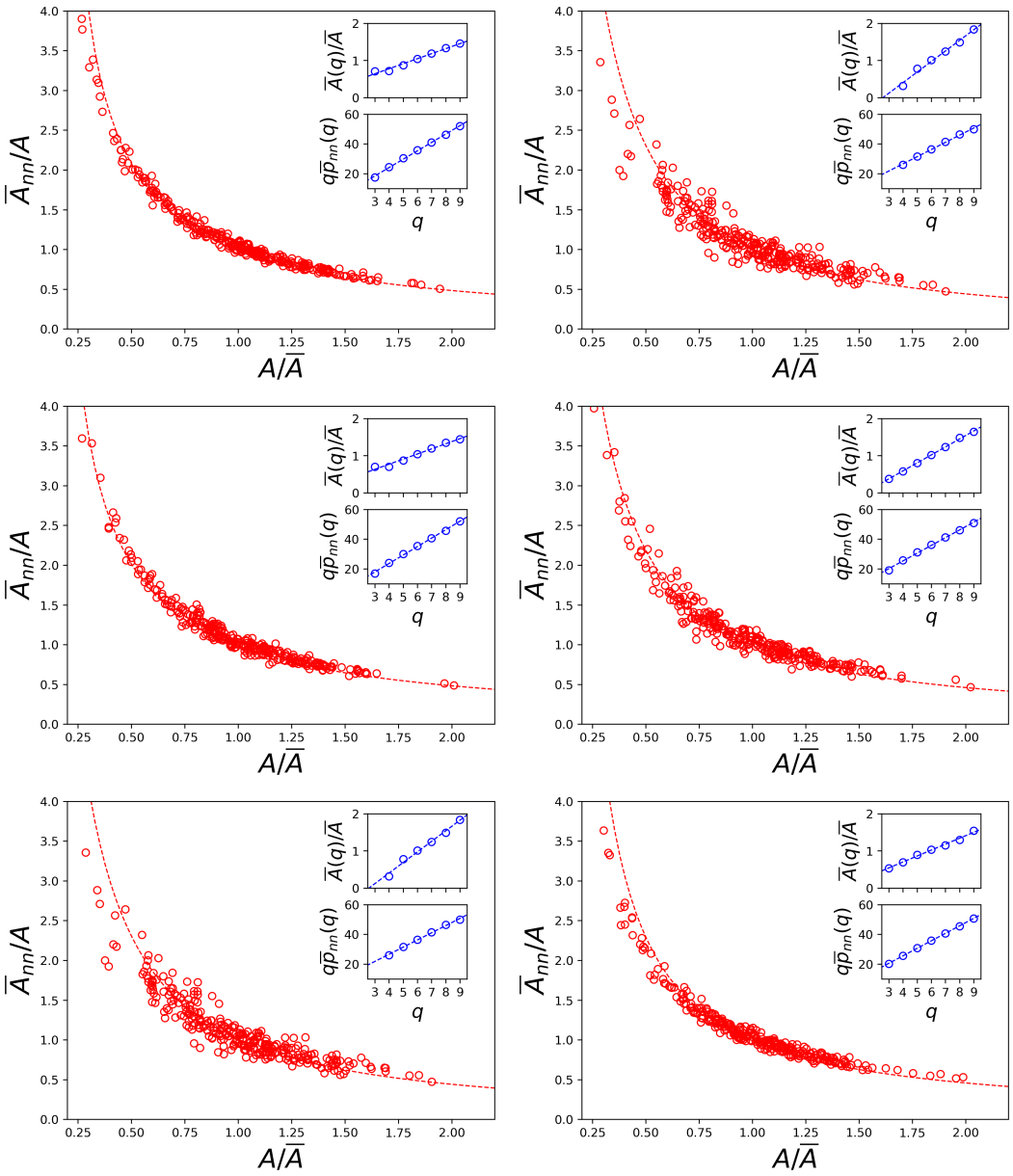

FIGURE 4.10: Normalized average area of neighbor cells, $\bar{A}_{nn}/A$ vs. $A/\bar{A}$ for $\beta = 0.1, 0.2, 0.3$ with fixed $v_0 = 2.5$ (left column) and $v_0 = 2.5, 3.5, 5.0$ with fixed $\beta = 0.3$ (right column) from left to right, together with a fit according to (4.7). Inset (top) shows $\bar{A}(q)/A$ vs. coordination number q, corresponding to Lewis's law. The line shows a linear fit through the data. Inset (bottom) shows the average coordination number of nearest neighbor cells of q-coordinated cells vs. coordination number q, corresponding to Aboav-Weaire's law. The line shows a linear fit through the data.

We have performed a numerical study to check whether Lewis' law (4.5), Aboav-Weaire's law (4.6) and the derived relation in equation (4.7) holds for our models and how these relations are influenced by two components:

1. The coupling strength of shape and activity, given by β. We set a constant $v_0 = 2.5$ and vary $\beta \in \{0.1, 0.2, 0.3\}$.

2. The self-propulsion velocity parameter v_0 effectively scaling the strength of activity. We set $\beta = 0.3$ and choose $v_0 \in \{2.5, 3.5, 5.0\}$.

Furthermore, we investigate the dependence on a state of collective motion or flocking, which has been shown to depend on these parameters in Section 4.3.
The results for the fitting of Lewis' law to our simulation data are shown in the upper insets of Figure 4.10. For fixed $v_0 = 2.5$ and $\beta = 0.1, 0.2, 0.3$ the least-square fits for α and γ are given in Table 4.2. On the other hand, for a constant shape-polarization coupling of $\beta = 0.3$, the fitted values depending on $v_0 = 2.5, 3.5, 5.0$ are given in Table 4.3.

$v_0 = 2.5$	$\beta = 0.1$	$\beta = 0.2$	$\beta = 0.3$
α	0.14	0.14	0.28
γ	1.05	1.05	0.97

TABLE 4.2: LS-Fits for α and γ in Lewis's law. Self-Propulsion is constant at $v_0 = 2.5$ and β is varied. Each parameter is fitted over the data from three independent simulations.

$\beta = 0.3$	$v_0 = 2.5$	$v_0 = 3.5$	$v_0 = 5.0$
α	0.28	0.21	0.16
γ	0.97	1.02	1.02

TABLE 4.3: LS-Fits for α and γ in Lewis's law. Shape-Polarization coupling is constant at $\beta = 0.3$ and v_0 is varied. Each parameter is fitted over the data from three independent simulations.

If for $\beta = 0.2$ (Table 4.2, middle column) only the times, where collective motion is already reached ($0.9 < \theta$), are considered, we obtain $(\alpha, \gamma) = (0.19, 0.99)$. Thus, we observe that the values for situations with collective motion are again in excellent agreement with data in [SS95], where $0.20 \leq \alpha \leq 0.25$ and $0.95 \leq \gamma \leq 1.05$ has been reported.
The data collection for Aboav-Weaire's law is shown in the lower insets of Figure 4.10 for the same simulations as before. The fitted values for the parameters ζ and η depending on β and v_0 are given in Tables 4.4 and 4.5 respectively.

$v_0 = 2.5$	$\beta = 0.1$	$\beta = 0.2$	$\beta = 0.3$
ζ	0.36	0.32	1.18
η	35.35	34.97	36.22

TABLE 4.4: LS-Fits for ζ and η in Aboav-Weaire's law. Self-Propulsion is constant at $v_0 = 2.5$ and β is varied. Each parameter is fitted over the data from three independent simulations.

$\beta = 0.3$	$v_0 = 2.5$	$v_0 = 3.5$	$v_0 = 5.0$
ζ	1.18	0.79	0.96
η	36.2	35.76	35.62

TABLE 4.5: LS-Fits for ζ and η in Aboav-Weaire's law. Shape-Polarization coupling is constant at $\beta = 0.3$ and v_0 is varied. Each parameter is fitted over the data from three independent simulations.

For $\beta = 0.2$, if collective motion is already reached ($0.9 < \theta$), we obtain the values $(\zeta, \eta) = (1.20, 35.93)$. We can again observe that, if cells are close to a system of collective motion, the simulation results are very close to those measured in passive systems, see [SS95], where $(\zeta, \eta) = (1.10, 36.64)$ have been reported. The linearity of the Aboav-Weaire's law has also been found theoretically [GKY92] and experimentally [MVD90].
To further confirm these results, we classify the whole data set (all β, all v_0, all initial conditions) according to the value of the translational order parameter θ. We classify the chaotic regime by $\theta < 0.3$, the intermediate regime by $0.3 \leq \theta \leq 0.9$ and the state of collective motion if $0.9 < \theta$ and obtain the values in Table 4.6.

		Lewis's law		Aboav-Weaire's law	
	μ_2	α	γ	ζ	η
$\theta < 0.3$	0.98	0.14	1.04	0.64	35.25
$0.3 \leq \theta \leq 0.9$	0.88	0.17	1.03	0.69	35.40
$0.9 < \theta$	0.78	0.26	0.97	1.11	36.28
Sire et al. [SS95]	0.64	[0.20, 0.25]	[0.95,1.05]	1.10	36.64

TABLE 4.6: Variance of coordination number probability $P(q)$ and linear fitting parameters - α, γ for Lewis' law and ζ, η for Aboav-Weaire's law - over all simulations, classified according to translational order parameter θ.

In summary, we obtain qualitative agreement with equilibrium topological and geometrical relations widely found in passive systems, independent of the used parameters and the macroscopic state of the active cellular structure. Furthermore, we have observed quantitative agreement with typical values for Lewis's law, Aboav-Weaire's law and the combined functional form in eq. (4.7) for passive systems, within the state of collective motion.

4.6 | CONCLUSIONS

Our investigations indicate that also in active cellular structures, if they are collectively moving, the cells are arranged in space to maximize the configurational entropy. This could indicate that intercellular arrangements are not mainly driven by actively organizing mechanism (e.g. the distribution of certain chemicals) but instead result mostly from essential geometrical and topological order structures. This coincides with the observations in [Kok+19] and [Vet+19] that claim surface energy minization and angle constraints to be the reason for well-defined alignment patterns like Lewis' law and Aboav-Weaire's law in biological systems.

5 | Cellular Shape and Flow Driven by Activity

The dynamically changing structures of cells in tissue, in particular the deformation and movement of individual cells, has been a focus of interest throughout the history of biology and medicine. More recently, the interplay between motion and shape of cells has also been examined, for example during organogenesis in [ET+18] or early stage development of zebrafish embryos in [Ban+21]. While there is growing experimental evidence for connections between cell deformations and tissue motility, the underlying dynamics are still not fully understood. The simulations performed in the following give rise to a deeper understanding and may help in the design of models that reproduce the behavior of nature even better.

This chapter is structured according to a variety of different experimental setups, in order to successively gain a deeper understanding how deformations and movements in Multi-Phasefield descriptions of cellular structures are connected.
We start by a definition of the models in Section 5.1, including the 4 different mechanisms for activity introduced in the Section 3.4. Then we investigate the occurrence of a transition between a solid-like and liquid-like state in a large, confluent system, depending on the parameters of the model in Section 5.2. Having identified the liquid regime, we concentrate on the occurring patterns in cell shape and tissue topology throughout Section 5.3. Afterwards, in Section 5.4, we investigate the cellular structures with the measures of active flows and identify patterns like the occurrence of vortices. At the end of the chapter, in Section 5.5, we compare the findings for large, confluent tissue structures with the occurring patterns in confined systems.

5.1 | Model Setup

In this chapter, we use 4 different modeling setups with the essential difference in the mechanism of activity. The dynamics underlying cell motility are still not fully

understood and, as a consequence, this is one of the most focused aspects of this chapter and the thesis in general. To isolate the dependence on the mechanism of activity, we have created experimental setups that are otherwise mostly identical. In practical, this means we always consider evolution equations of the form

$$\partial_t \phi + v_0(\mathbf{v}_i \cdot \nabla \phi_i) = \Delta \frac{\delta \mathcal{E}}{\delta \phi_i}$$

for a particular system energy $\mathcal{E}$ and propulsive force $\mathbf{v}_i$.
To define the *random model* and also the *elongation model* we use the Cahn-Hilliard type energy introduced in (3.5) and the distance-based interaction in (3.11), which reads

$$\mathcal{E}^{ran,elo}\left(\{\phi_i\}\right) = \frac{1}{Ca}\mathcal{E}_{CH}\left(\{\phi_i\}\right) + \frac{1}{In}\mathcal{E}^{d}_{INT}\left(\{\phi_i\}\right) \tag{5.1}$$

with the dimensionless weight parameters Ca and In. For the random model, activity is based on the stochastic law in (3.17), i.e. $\mathrm{d}\theta(t) = \sqrt{2D_r}\mathrm{d}W_i(t)$ and the resulting vector

$$\mathbf{v}_i^{ran} = \begin{bmatrix} \cos\theta_i \\ \sin\theta_i \end{bmatrix}$$

as already defined in (3.18). The evolution equation for a single Phasefield ϕ_i, according to an H^{-1} gradient flow, is then given by

$$\begin{aligned} \partial_t \phi_i + v_0\left(\mathbf{v}_i^{ran} \cdot \nabla \phi_i\right) &= M\Delta\mu_i\,, \\ \mu_i := \frac{\delta \mathcal{E}^{ran,elo}}{\delta \phi_i} &= \frac{1}{Ca}\left(-\epsilon\Delta\phi_i + \frac{1}{\epsilon}W'(\phi_i)\right) \\ &+ \frac{1}{In}\left(B'(\phi_i)\sum_{j\neq i} w_E(d_j) + w_E'(d_i)d_i'(\phi_i)\sum_{j\neq i} B(\phi_j)\right) \end{aligned} \tag{5.2}$$

with M a mobility factor. For the elongation model on the other hand, the active force is given by

$$\mathbf{v}_i^{elo} = \int_\Omega \tilde{\phi}_i \nabla \cdot \boldsymbol{\varpi}_{tissue}$$

as introduced in (3.23) and the resulting evolution equation reads

$$\begin{aligned} \partial_t \phi_i + v_0\left(\mathbf{v}_i^{elo} \cdot \nabla \phi_i\right) &= M\Delta\mu_i\,, \\ \mu_i := \frac{\delta \mathcal{E}^{ran,elo}}{\delta \phi_i} &= \frac{1}{Ca}\left(-\epsilon\Delta\phi_i + \frac{1}{\epsilon}W'(\phi_i)\right) \\ &+ \frac{1}{In}\left(B'(\phi_i)\sum_{j\neq i} w_E(d_j) + w_E'(d_i)d_i'(\phi_i)\sum_{j\neq i} B(\phi_j)\right). \end{aligned} \tag{5.3}$$

We emphasize at this point that the only difference between (5.2) and (5.3) lies in the used advection term but we will later in this chapter see how significantly this seemingly minor change affects the model behavior.
To define the *polar model*, the energy is assembled from the previously used components $\mathcal{E}_{CH}$ and $\mathcal{E}_{INT}$ with the additional Oseen-Frank type energy defined in (3.24). This approach now uses both a Phasefield ϕ_i and a polarization field $\mathbf{P}_i$ to describe

a single cell and reads

$$\mathcal{E}^{pol}\left(\{\phi_i, \mathbf{P}_i\}\right) = \frac{1}{Ca}\mathcal{E}_{CH}\left(\{\phi_i\}\right) + \frac{1}{In}\mathcal{E}^d_{INT}\left(\{\phi_i\}\right) + \frac{1}{Pa}\mathcal{E}_{POL}\left(\{\phi_i, \mathbf{P}_i\}\right) \tag{5.4}$$

with the additional weight Pa. Note that this energy is identical to the one used in Chapter 4 for the study of Topological and Geometrical Quantities. The propulsion in this model is directly given by the (non-constant) polarization field and thus reads

$$\mathbf{v}_i^{pol} = \mathbf{P}_i.$$

The evolution of ϕ_i follows an H^{-1} gradient flow while we use an L_2 gradient flow for $\mathbf{P}_i$, so the whole system is described by

$$\begin{aligned}
\partial_t \phi_i + v_0\left(\mathbf{v}_i^{pol}\cdot\nabla\phi_i\right) &= M\Delta\mu_i\,, \\
\mu_i := \frac{\delta\mathcal{E}^{pol}}{\delta\phi_i} &= \frac{1}{Ca}\left(-\epsilon\Delta\phi_i + \frac{1}{\epsilon}W'(\phi_i)\right) \\
&\quad + \frac{1}{Pa}\left(-\frac{1}{2}\|\mathbf{P}_i\|^2 - \beta\nabla\cdot\mathbf{P}_i\right) \\
&\quad + \frac{1}{In}\left(B'(\phi_i)\sum_{j\neq i} w_E(d_j) + w_E'(d_i)d_i'(\phi_i)\sum_{j\neq i} B(\phi_j)\right),
\end{aligned} \tag{5.5}$$

$$\partial_t \mathbf{P}_i = -\frac{\delta\mathcal{E}^{pol}}{\delta\mathbf{P}_i} = -\frac{1}{Pa}\Big(-\phi_i\mathbf{P}_i + \|\mathbf{P}_i\|^2\mathbf{P}_i - \Delta\mathbf{P}_i + \beta\nabla\phi_i\Big). \tag{5.6}$$

Note that we have, in contrast to (4.3), omitted the self-advection term in (5.6). While it was originally included in the model for reasons of thermodynamical consistency, we have observed no significant influence of this term on the model behavior and thus removed it to create a setup that is easier comparable with the models without subcellular structure.

The *nematic model* involves for each Phasefield ϕ_i an additional tensorfield, denoted by $\mathbf{Q}_i$. In addition to the Cahn-Hilliard type energy and the interaction energy, we use the Landau-de Gennes type energy introduced in (3.26). The total energy of the system then reads

$$\mathcal{E}^{nem}\left(\{\phi_i, \mathbf{Q}_i\}\right) = \frac{1}{Ca}\mathcal{E}_{CH}\left(\{\phi_i\}\right) + \frac{1}{In}\mathcal{E}^d_{INT}\left(\{\phi_i\}\right) + \frac{1}{Ne}\mathcal{E}_{NEM}\left(\{\phi_i, \mathbf{Q}_i\}\right) \tag{5.7}$$

for Ne a scalar weight parameter, as usual. The propulsion is defined as in (3.27) and given by

$$\mathbf{v}_i^{nem} = \nabla\cdot\mathbf{Q}_i.$$

To define the evolution equations for ϕ_i and $\mathbf{Q}_i$, we again invoke an H^{-1} and L_2 gradient flow, respectively and arrive at

$$\begin{aligned}\partial_t\phi_i + v_0\left(\mathbf{v}_i^{nem}\cdot\nabla\phi_i\right) &= M\Delta\mu_i\,,\\ \mu_i := \frac{\delta\mathcal{E}^{nem}}{\delta\phi_i} &= \frac{1}{Ca}\left(-\epsilon\Delta\phi_i + \frac{1}{\epsilon}W'(\phi_i)\right)\\ &+ \frac{1}{Ne}\left(-\frac{1}{2}\,\mathrm{tr}\mathbf{Q}_i^2 + \gamma\nabla\cdot(\mathbf{Q}_i\nabla\phi_i)\right)\\ &+ \frac{1}{In}\left(B'(\phi_i)\sum_{j\neq i}w_E(d_j) + w_E'(d_i)d_i'(\phi_i)\sum_{j\neq i}B(\phi_j)\right),\end{aligned} \tag{5.8}$$

$$\begin{aligned}\partial_t\mathbf{Q}_i = -\frac{\delta\mathcal{E}^{nem}}{\delta\mathbf{Q}_i} &= -\frac{1}{Ne}\Big(-\phi_i\mathbf{Q}_i + \mathrm{tr}\mathbf{Q_i}^2\mathbf{Q_i} - \Delta\mathbf{Q}_i\\ &+ \gamma\left(\nabla\phi_i\nabla\phi_i^T - ||\nabla\phi_i||^2 Id\right)\Big).\end{aligned} \tag{5.9}$$

We notice similarities between this nematic model and the polar model in (5.5) and (5.6), for example a restriction to the interior of the Phasefield. The key differences lie in the propulsion mechanism and the different type of coupling between the Phasefield and intracellular field $\mathbf{P}_i/\mathbf{Q}_i$. Interestingly, the last term in (5.9), i.e. a source depending on the Phasefield ϕ_i, is identical to the geometrical Q-tensor $\mathbf{S}_i$ introduced in (3.19), measuring cell elongations.
In case of confined systems, we additionally use the confinement energy introduced in (3.29), which is independent of the mechanism of propulsion and has variational derivative

$$\frac{\delta\mathcal{E}^d_{CON}}{\delta\phi_i} = B'(\phi_i)w_E(d_{con}). \tag{5.10}$$

We never explicitly include the confinement in the dynamics of the intracellular fields to keep the models more comparable. Due to the restrictive terms in both (5.6) and (5.9), it is however implicitly enforced as $\mathbf{P}_i/\mathbf{Q}_i$ vanishes outside the cell interior.
If we model confinement in our simulations, we thus add the term (5.10) to the equation for μ_i, scaled with a parameter Con. For example in the random model, the evolution equations for the Phasefields ϕ_i then read

$$\begin{aligned}\partial_t\phi_i + v_0\left(\mathbf{v}_i^{nem}\cdot\nabla\phi_i\right) &= \gamma\Delta\mu_i\,,\\ \mu_i := \frac{\delta\mathcal{E}^{ran,elo}}{\delta\phi_i} &= \frac{1}{Ca}\left(-\epsilon\Delta\phi_i + \frac{1}{\epsilon}W'(\phi_i)\right)\\ &+ \frac{1}{In}\left(B'(\phi_i)\sum_{j\neq i}w_E(d_j) + w_E'(d_i)d_i'(\phi_i)\sum_{j\neq i}B(\phi_j)\right)\\ &+ \frac{1}{Con}B'(\phi_i)w_E(d_{con}),\end{aligned} \tag{5.11}$$

and all other models are treated equivalently.
All evolution equations described here, are simulated in $\Omega\times(0,T]$ for a finite end time $T>0$ and a two-dimensional domain Ω. The domain is equipped with periodic boundary conditions. The partial differential equations are numerically solved in AMDiS with the cell-based parallelization, see Section 3.6.
For the initial conditions, we choose three of the setups presented in Subsection 3.6.2

and depicted in Figures 3.17 and 3.18, depending on the particular experiment. In case of purely periodic systems, representing large, confluent tissue structures, as done in Sections 5.2 - 5.4, we use the brick-wall structure in a rectangular domain. In 5.5, however, we focus on confined systems in both rectangular and circular geometry (depending on the used norm in (3.28)). For rectangular confinements, we simply alter the brick-wall structure by shifting every second row by half a brick-width to prevent any boundary overlap. For circular geometries on the other hand, we use the ring packing. More details and visualizations of the initial conditions are found in Subsection 3.6.2.
Almost all parameters of the system are kept constant throughout the simulations and can be chosen equal for all mechanisms of propulsion. A summary of the parameterset can be found in Table 5.1. Not listed are the self-propulsion parameter v_0 and the scaling of the Cahn-Hilliard energy, namely Ca. We will observe throughout this chapter how these two parameters, in interplay, have crucial influence on many observables like the physical state of the system.

Ω	ϵ	M	In	Pa	Ne	Con	β	γ
$[0,100] \times [0,100]$	0.15	1	0.025	1	1	0.004	0.01	0.1

TABLE 5.1: Numerical parameters used in all simulations throughout Chapter 5.

To resolve the Phasefield boundaries well, without including unnecessary computational effort, we use the typical locally refined grids. In particular, we choose $h \approx 0.2\epsilon$ inside the diffuse interface, $h \leq \epsilon$ in the interior and $h \leq 10\epsilon$ in the exterior of each Phasefield as visualized in Figure 3.16. We let the system relax for a few small time steps and then use a constant time stepping with $\tau = 0.1$.
We will use the rest of this chapter to investigate the influence of the propulsion mechanism on the evolving patterns in cell shape and flow. In particular, we will focus on the emergence of transition between a solid and liquid-type behavior as observed in living tissue. Afterwards, we will analyze the typical shapes and investigate the flow of the cellular structure from the point of view of fluid dynamics in turbulent systems. We conclude this chapter by changing the experimental setup to a confinement.

5.2 | SOLID-LIQUID TRANSITION IN TISSUE MODELS

Traditionally, it was a very common approach to consider tissue as purely liquid material. This was motivated for example by experiments on the intrinsically driven separation of two species of cells, as performed in [Ste62], strongly resembling typical phase separation behavior known from multi-liquid systems. Observations of wetting-like phenomena, that have been investigated more recently in [DDBW12], have strengthened this viewpoint even further.
There is, however, a variety of phenomena in living tissue that can not be explained using the perspective of a constantly liquid state of matter. We will use the description of tissue as a system capable of transitioning between a solid and a liquid state. This behavior of a so-called solid-liquid or glass transition was originally observed in crystalline materials or polymers, see [KP61] and [SN59]. There has been growing experimental evidence that a solid-liquid transition plays a crucial role in tumor spreading as reviewed in [Osw+17]. Furthermore it has been reported in [Mon+18]

that a liquid-solid transition, i.e. the reversed process, happens during the body axis elongation in Zebrafish.
At this point, we also want to clarify the connection to the physical phenomenon *jamming*. Originally, the jamming transition describes the process of increasing particle density and the resulting solid-like behavior. However, it was pointed out in [LN98] that jamming does not only depend on particle density but also on temperature and activity. Keeping in mind, that in a state of confluence, resembled by the high packing fraction in our models, the density is constant and temperature is usually of minor importance in cellular systems, we observe that the phenomena jamming transition and solid-liquid transition are in fact closely related.
Solid-liquid transitions have been extensively studied in vertex and voronoi models, see e.g. [Bi+14; Bi+15; Kra20]. They have been observed to depend mostly on the strength of activity and the cell deformability. While in vertex models the deformability is typically described using a shape index, we here follow [Loe+20] and directly consider the surface tension, respectively the capillary number Ca. The strength of activity is, due to the modular derivation of the models, always represented by v_0.
To quantify the transition, an easily accessible structural property, the coordination number q, i.e. the number of neighboring cells, is considered. In particular, we measure the deviation from the hexagonal ordering, the optimal dense packing in rectangular domains, which can be expressed by the statistic variance

$$\mu(q) = \sum_q (q-6)^2 P(q) \tag{5.12}$$

with $P(q)$ the discrete probability distribution obtained from counting the presence of each value q. We identify the liquid phase, if $\mu(q) > \theta_{P(q)}$ holds for the variance $\mu(q)$ and the threshold $\theta_{P(q)} = 0.001$. Figure 5.1 shows the phase diagram for the four models. Blue are regions where the observable indicates solid-like behaviour and red are regions where $\mu(q)$ indicates liquid-like behaviour.

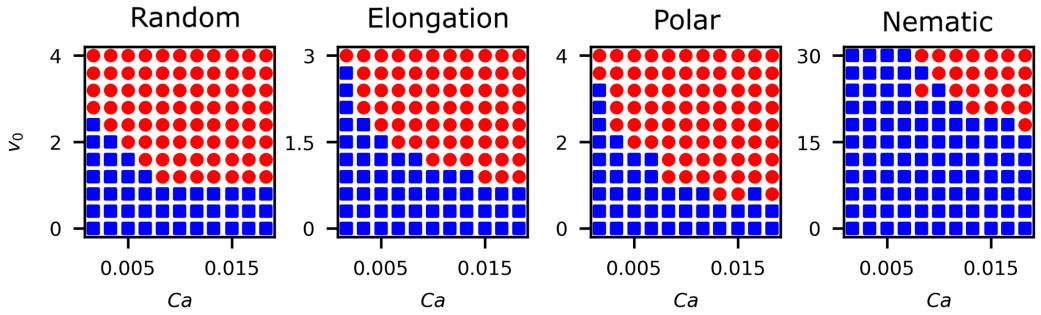

FIGURE 5.1: Phase diagram showing transition between solid (blue) and liquid (red) state as function of the deformability parameter (capillary number) Ca and the activity (self-propulsion strength) v_0.

Although the qualitative behavior of the phase diagram is quite similar for all four models and the previous studies using vertex and voronoi models like in [Bi+16], the actual quantitative results in terms of the parameter range for v_0 differ strongly. Both the random and the polar model are driven by a normalized vector field with a clearly preferred direction, which results in a quantitatively similar behaviour. For the elongation and the nematic model, the driving force is computed as divergence

of a tensor field and thus not normalized, indicating why they have a parameter range which is different from the other two models. Especially for the nematic model larger propulsion v_0 is required to drive the system out of equilibrium, due to the typical structure of the advection $\mathbf{v}_i^{nem}$ as visualized in Figure 3.14.
The snapshots in Figure 5.2 show typical cell shapes for the four models in the liquid and solid phase, respectively. The cell shapes are isotropic on average in the solid phase and anisotropic in the liquid phase, leading to differences in the number of neighbors. Also, the cell tracks significantly differ, they show dynamical arrest due to caging in the solid phase and diffusion in the liquid phase. These tracks are obtained by considering the center of mass of each cell in each time step. While the solid phase is more or less identical in all four models, the liquid phase differs significantly.

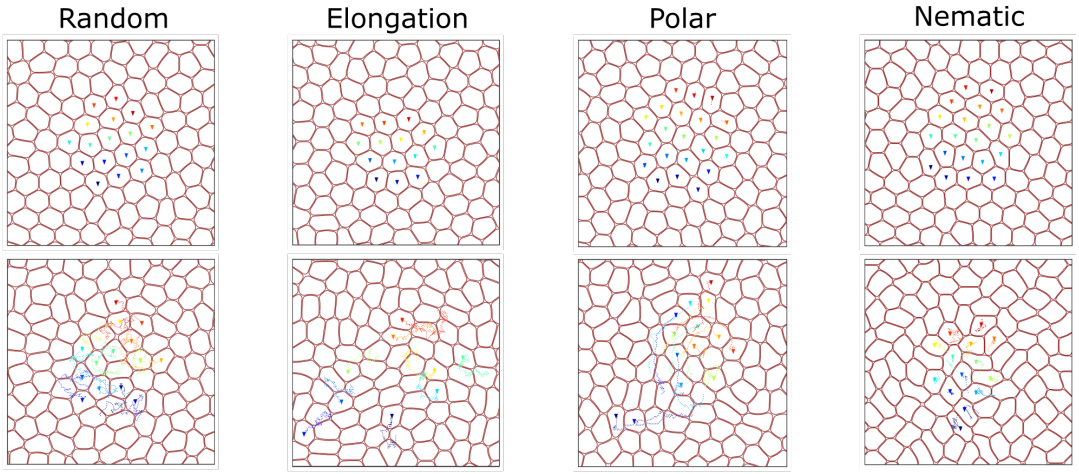

FIGURE 5.2: Snapshots of tissue morphology for solid phase (first row) and liquid phase (second row), for the four models, random, elongation, polar and nematic (from left to right). Shown are the levelsets $\phi_i = 0$ together with cell trajectories for some time span of the cells in the center, indicating diffusion in the liquid phase and dynamical arrest due to caging in the solid phase.

Having identified the liquid phase, we will focus most considerations on this parameter range. In particular, we will often fix the deformability parameter $Ca = 0.0148$ for all models and use three significant levels of activity strength v_0, which we denote low, medium and high. The precise choice of v_0 depends on the mechanism of activity but is kept constant throughout the following section and can be found in Table 5.2.

	random	elongation	polar	nematic
low	1.2	1.0	1.2	21.0
medium	2.4	2.0	2.4	24.0
high	3.6	3.0	3.6	30.0

TABLE 5.2: Chosen values for v_0 classified as low, medium and high activity for simulations in Chapter 5.

Having chosen these significant levels of activity, all in the liquid phase, we can investigate the probability distribution $P(q)$ for the coordination number q more in

detail. In particular, the arising question is how mean and variance of the discrete probability distribution $P(q)$ depend on the strength of activity. To investigate this, we have performed simulations for fixed $Ca = 0.0148$ and the three significant levels of activity. The results in Figure 5.3 visualize $P(q)$ as an average over all cells and timesteps .

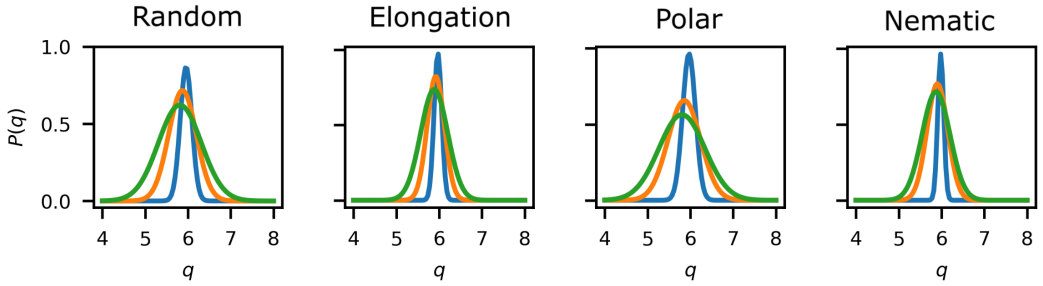

FIGURE 5.3: Coordination number probability $P(q)$ for $Ca = 0.0148$ with low (blue), medium (orange) and high (green) values of v_0. For actual values see Table 5.2.

To also give a quantitative insight into the results depicted in Figure 5.3, we have listed the values for both the empirical mean $\overline{q} = \sum_q qP(q)$ and the previously introduced variance $\mu(q)$ for all models in Tables 5.3 and 5.4, depending on the level of activity.

$\overline{q}$	random	elongation	polar	nematic
low	5.96	5.97	5.97	5.98
medium	5.87	5.92	5.86	5.90
high	5.81	5.88	5.80	5.87

TABLE 5.3: Empirical mean $\overline{q}$ of the coordination number for low, medium and high activity.

$\mu(q)$	random	elongation	polar	nematic
low	0.14	0.09	0.15	0.07
medium	0.32	0.20	0.38	0.24
high	0.50	0.32	0.54	0.33

TABLE 5.4: Empirical variance $\mu(q)$ of the coordination number for low, medium and high activity.

In review of these results, we can conclude that the overall behavior of the models is similar. All models show empirical mean values $\overline{q}$ close to but slightly below the value 6, corresponding with a perfect hexagonal packing. The shrinkage in the values of $\overline{q}$ for increased activity, observable for all models, can be explained by the typically larger crowding in certain parts of the domain that happens for high activity and the resulting free spaces in other areas, existing due to the packing fraction slightly below 100%. Furthermore, the variance $\mu(q)$ increases for higher activity in all models. This can be explained by larger cell deformations, see Section 5.3 for a more detailed investigation, that may lead to a change in the number of neighbors and also the more frequent exchanges in neighboring relations. A typical situation is visualized in Figure 5.4 with larger areas of free space and more strongly deformed

cells for high activity. The color coding visualizes q and emphasizes larger variance for the high activity.

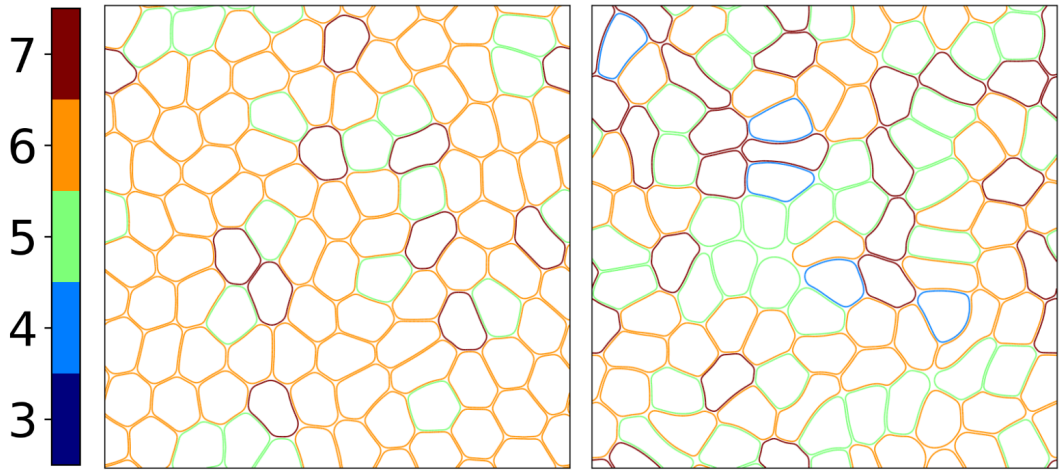

FIGURE 5.4: Typical cellular structure for low (left) and high (right) activity in the polar model. Phasefields are visualized by the levelset $\phi_i = 0$. Color coding represents the coordination number q.

We will use the remainder of this chapter to investigate the liquid phase further, with special focus on the occurring generic features and observables. Precisely, we will analyze the influence of the activity mechanism on the typical cell shapes, the evolving patterns of motion and long-range order structure.

5.3 | SHAPE AND TOPOLOGY

Typical shapes of cells and corresponding alignment in tissue can vary strongly between different organisms. Even among the same type of cell, strong differences can observed, depending for example on the age of the tissue or external factors like mechanical stress or diseases.

5.3.1 | DISTRIBUTION OF CELL SHAPE

Experimental data acquired in Human Bronchial Epithelial Cells (HBEC) in [Par+15] for example indicates significant differences in cell elongation and shape between asthmatic and non-asthmatic donors. On the contrary, most recent studies in [Ati+18] indicate that the general distribution of these quantities follows a similar statistical law, independent of the particular organism or disease.
In Section 5.2, we have already made the observation that the mechanism and strength of activity can have a significant influence on the resulting cell shape. We will use the beginning of this section to quantify this observation. Furthermore, we will validate the universal laws given in [Ati+18] for our models and investigate resulting topological properties like the occurrence of rosettes.
To measure the deformation of a particle cell, represented by a Phasefield ϕ_i, we use the tensor

$$\mathbf{S}_i = \begin{bmatrix} S_{i,0} & S_{i,1} \\ S_{i,1} & -S_{i,0} \end{bmatrix} = \begin{bmatrix} \int_\Omega \frac{1}{2}\left((\partial_y\phi_i)^2 - (\partial_x\phi_i)^2\right) & \int_\Omega -(\partial_x\phi_i)(\partial_y\phi_i) \\ \int_\Omega -(\partial_x\phi_i)(\partial_y\phi_i) & \int_\Omega \frac{1}{2}\left((\partial_x\phi_i)^2 - (\partial_y\phi_i)^2\right) \end{bmatrix}$$

which we have introduced in (3.19) as key component for the elongation propulsion mechanism. As already mentioned, the eigenvalues

$$\lambda_i^{\pm} = \pm\sqrt{S_{i,0}^2 + S_{i,1}^2}$$

capture the strength of the deformation of ϕ_i. We will from now on restrict all considerations to the positive eigenvalue λ_i^+.
While the quantitative values of λ_i^+ depend on different modeling parameters, especially the cell area, and are thus of minor relevance, they can be compared among different setups, given the fact that sizes are equal. We will in the following use the notation $AR_i := \lambda_i^+$ to clarify that we use this quantity to represent the aspect ratio of a cell.
Similar to the studies on the coordination number q, we measure the discrete probability distribution $P(AR)$ for all cells and timesteps in simulations with all 4 models and the three significant levels of activity as introduced in Table 5.2. We compute the empirical mean $\overline{AR}$ of the aspect ratio and the corresponding variance $\mu(AR)$.

$\overline{AR}$	random	elongation	polar	nematic
low	5.88	5.39	7.49	5.97
medium	8.04	5.96	7.67	7.70
high	9.48	6.35	7.66	8.30

TABLE 5.5: Empirical mean $\overline{AR}$ of the aspect ratio for low, medium and high activity.

$\mu(AR)$	random	elongation	polar	nematic
low	3.04	3.38	4.18	2.96
medium	4.31	3.83	4.41	3.35
high	5.11	5.13	4.41	3.77

TABLE 5.6: Empirical variance $\mu(AR)$ of the aspect ratio for low, medium and high activity.

In review of Tables 5.5 and 5.6, we observe in general an increase in both the average aspect ratio and the variance for higher activities. This means that cells in more active systems are more strongly deformed and there is additionally more differences in deformation across the tissue. This corresponds with the observations for asthmatic HBEC cells that have been reported in [Par+15] to be more deformed compared to non-asthmatic cells and quantifies the visual impression in Figure 5.4. We furthermore observe differences between the models in the sense that the values for the polar model change fewer, depending on the level of activity compared to the random, elongation or nematic model.
Interestingly, we can also observe that the mean aspect ratio $\overline{AR}$ and the variance $\mu(AR)$ seem to grow dependently, which coincides with the findings in [Ati+18]. There it has furthermore been proposed that the normalized aspect ratio $\frac{AR}{\overline{AR}}$ follows a universal k-Gamma distribution with probability distribution function

$$PDF(x,k) = \frac{k^k}{\Gamma(k)} x^{k-1} e^{-kx}$$

where $\Gamma(k)$ denotes the Legendre Gamma-function. This distribution is fully described by the parameter k, and has a mean of unity. In [Ati+18] the normalized

aspect ratio was investigated across a variety of organisms like Madin Darby Canine Kidney (MDCK) cells, the Drosophila embryo during ventral furrow formation and the aforementioned Human Broncial Epithelia Cells. It has been observed that $\frac{AR}{\overline{AR}}$ follows the k-Gamma distribution for all of these organisms. Even more, the distribution parameter k has been found to always be in the range between 2 and 3.

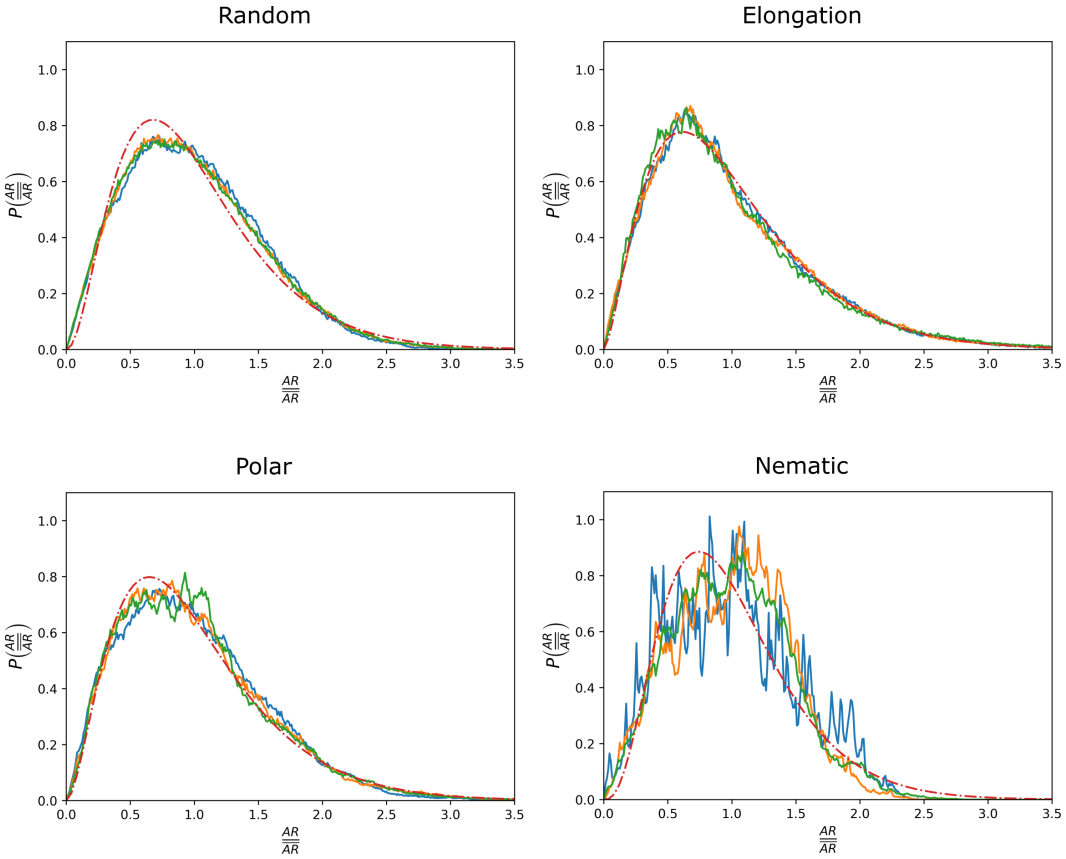

FIGURE 5.5: Shape variability for the four models using the rescaled parameter $x = \frac{AR}{\overline{AR}}$ with low (blue), medium (orange) and high (green) activity. Fitted values for the PDF (red) are computed using data for all three significant values of v_0, resulting in $k^{ran} = 3.11$,$k^{elo} = 2.59$, $k^{pol} = 2.84$ and $k^{nem} = 3.88$.

We have performed a numerical study to find out whether this general distribution can also be found in Multi-Phasefield models for tissue. We have chosen the capillary number $Ca = 0.0148$ and varied the activity according to the previously used significant values in Table 5.2. The discrete probability distributions are visualized in Figure 5.5 and the corresponding k-values for each v_0 are shown in Table 5.7.

k	random	elongation	polar	nematic
low	3.18	2.68	2.82	3.23
medium	3.12	2.60	2.87	4.20
high	3.04	2.49	2.85	4.21

TABLE 5.7: k-Gamma parameter fit for all four models with low, medium and high activity. The k-values are obtained with maximum-likelihood-estimation fits for $PDF(x,k)$ for one simulation run over the whole time.

Indeed, in accordance with the experimental results in [Ati+18], the data can be described by a k-Gamma distribution and k does not vary strongly within each model for the considered parameters. However, the k-values differ between the four models. While both the elongation and the polar model have values within the experimentally predicted universal range between 2 and 3, both the random and the nematic model are slightly above with the latter one leading to the largest values. These larger values for k in the nematic model become evident from the construction of the model, where active forces enhance elongation which is also apparent in Figure 3.14. This also explains why k is growing for larger values of v_0 only in the nematic model while it stays approximately constant in all others. The larger fluctuations in the polar and especially the nematic model can be explained by the stronger coupling between shape changes and active forces.

5.3.2 | ROSETTE FORMATION

Multicellular rosettes or higher-order vertices, where four or more cells meet, have been found in many types of tissue [HMN14]. The importance of cellular rosettes has been widely recognized and they have been proposed as an efficient mechanism for tissue remodeling. Further details have already been discussed in Section 4.2, where we have also visualized the occurrence of multi-cellular rosettes in the polar model. This part will be devoted to a slightly more quantitative study, depending on the mechanism of activity.
It is clear from all previous studies that the occurrence of rosettes and their ratio among all vertices where cells meet, should not only depend on the propulsion mechanism but also strongly on the level of activity v_0. To create a setup comparable with available experimental data, we have fixed the activity according the topological observable $\mu(q)$ introduced earlier. In particular, we use the value $\mu = 0.4$, which has been reported in [Bla+06] to be the typical coordination number variance in Drosophila embryos at an early stage of development (up to stage 7 before intercallation). Fixing the capillary number to $Ca = 0.018$, a lower value compared to the studies on $P(q)$ performed in Section 5.2, we have chosen v_0^* such that the observed variance $\mu(q)$ matches the target value 0.4.

	random	elongation	polar	nematic
v_0^*	1.3	0.6	1.3	19.0

TABLE 5.8: Activity levels v_0^* for the four models reproducing the physical state $\mu(q) \approx 0.4$, given capillary number $Ca = 0.018$.

Indeed, using the values in Table 5.8, we obtain $\mu = 0.41, 0.40, 0.44$ and 0.45 for the random, elongation, polar and nematic model, respectively which we consider to be physically comparable states. We have performed long-time simulations and measured the rosette ratio, i.e. the fraction of all vertices that connect more than three cells. The results for all four models are printed in Table 5.9.

	random	elongation	polar	nematic
rosette ratio	4.8%	2.6%	5.5%	1.3%

TABLE 5.9: Rosette ratio for all four models, considered for one simulation over the whole time for comparable physical states with $\mu(q) \approx 0.4$ resulting from the choices v_0^* given in Table 5.8.

Experimental data for the rosette ratio during the corresponding early stage of development (up to stage 7 before intercallation) in Drosophila embryos [Bla+06] show values between 5% and 6%, which is reproduced by the polar model. The random model leads to a ratio which is only slightly below. The other two models lead to significantly lower values. In later stages of development, this ratio is drastically increased. For the Drosophila embryos, the peak fraction of cells in rosettes at a single time point is 61% [Bla+06], but this corresponds to a different physical setting, for which the models have not been calibrated. Other data, e.g. in Zebrafish embryo [Hav+09], report a ratio of 1.8% which is closer to the values observed in the elongation and nematic model. Even if only one physical state is considered, which allows for a calibrated comparison with experimental data, the results strongly differ between the four models. These differences on the rosette ratio indicate a strong dependency on the mechanism of propulsion.

5.4 | Flow Patterns in Cellular Structures

The emergence of significant patterns in the flow of multi-cellular structures has been widely observed in different organisms. One aspect is the phenomenon of collective migration, investigated for example in [Pet+10], which we have extensively studied and reproduced for the polar model in Section 4.3. At this point, we have also observed that for sufficiently high activity and/or low coupling between shape and polarization, a regime of more chaotic motion with no collective order evolves which shall be the focus of this section.
In [BM+18] a large colony of Human Bronchial Epithelial Cells was investigated and flow patterns reminiscent of active turbulence were observed. In models for active liquid crystals such turbulent states emerge as a result of spontaneous defect pair creation. In [MYD19] the velocity field is also analysed for a Multi-Phasefield model. We here follow this approach and investigate the flow fields and vorticity patterns for all four models.
The first step in the investigation of large scale flow in cellular structures, compared to active turbulent systems, is the definition of a global velocity field $\mathbf{v}$. We define the velocity $\mathbf{v}_i$ of a single cell, using the center of mass

$$\mathbf{x}_i(t) = \frac{\int_\Omega x\tilde{\phi}_i(t,x)\mathrm{d}x}{\int_\Omega \tilde{\phi}_i(t,x)\mathrm{d}x} \tag{5.13}$$

which involves the $[0,1]$-rescaled Phasefield $\tilde{\phi}_i$ previously introduced. With an explicit time-scheme, using the travelled distance between the centers of mass in two consecutive time-instances, we can define the velocity $\mathbf{v}_i$ of each cell.
Starting from this single cell velocity, it is possible to choose different definitions of a global velocity field $\mathbf{v}$. In [MYD19], an approach similar to the one we use for the global deformation tensor in (3.22) is used, which reads $\sum_i \tilde{\phi}_i \mathbf{v}_i$. The disadvantage here is the discontinuity in densely packed systems, which can only be handled using a global smoothing. We use a more simple approach, involving a global linear interpolation with the data points given by $(\mathbf{x}_i, \mathbf{v}_i)$ onto a globally equidistant grid with 1000×1000 points. This has the advantage of being numerically more efficient, compared to handling all the locally refined Phasefields $\tilde{\phi}_i$, and handles the smoothing implicitly.
Figure 5.6 shows a Line Integral Convolution (LIC) visualization of the global velocity fields $\mathbf{v}$ for the low velocity in Table 5.2. We observe local maxima in the velocity magnitude, visualized by dark red color and the occurrence of local vortices. The

combination of these two observations resembles typical behavior in turbulent flow.

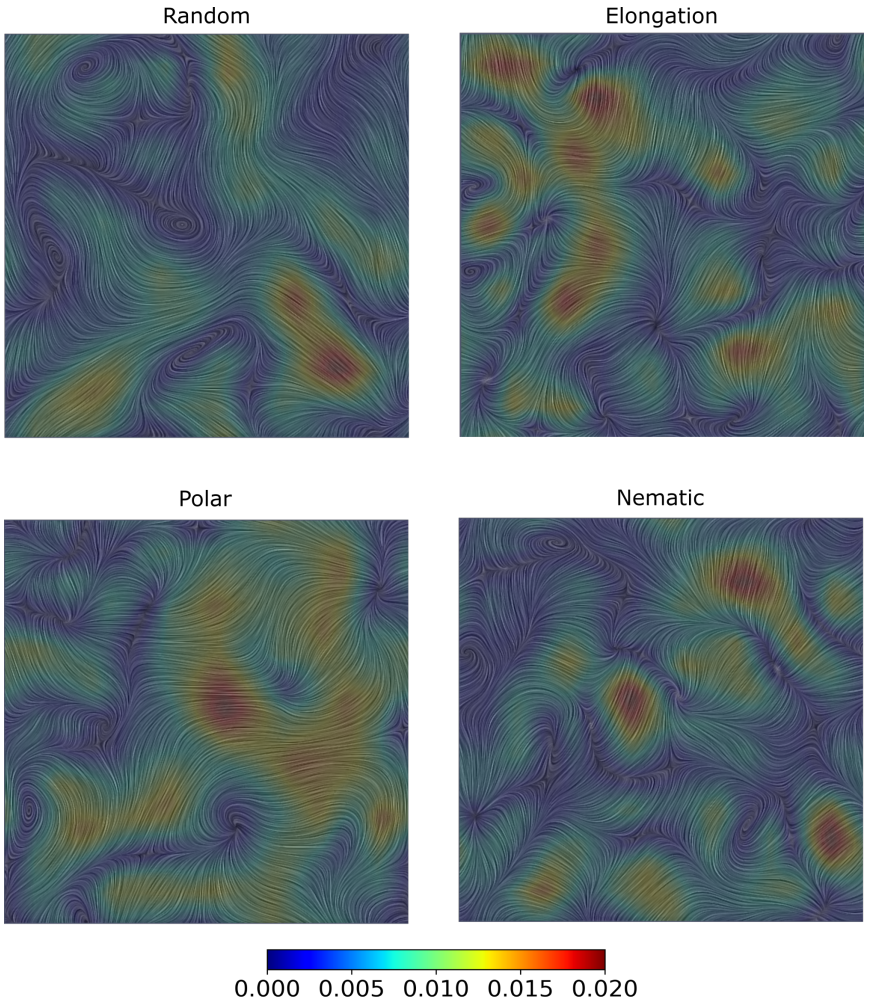

FIGURE 5.6: LIC visualization of large scale flow dynamics for the four models: random, elongation, polar and nematic (from left to right) in the low activity regime according to Table 5.2. Color represents the magnitude of the velocity with the same scaling for all models.

Interestingly, the vortices observable in the LIC visualization in Figure 5.6 look similar in all four models. To confirm this observation, we have computed the vorticity-vorticity correlation function

$$C_\omega(r) = \frac{\int_\Omega \omega(x,r)\omega(x,0)\mathrm{d}x}{\int_\Omega \omega(x,0)^2\mathrm{d}x}$$

where $\omega(x,r)$ denotes the vorticity average for all points of distance r from point x. The results are shown in Figure 5.7 for distances up to $r = 50$, in order to avoid any influence from the periodic boundaries. The previous observations are confirmed by the very similar behavior for C_ω in all models. The common feature is a well-defined length-scale at which the vorticity correlation attains negative values, corresponding with the occurrence of vortices at a particular distance. The position and depth of

the minimum in the polar model deviates from the other models which can be explained by the previously examined tendency to develop collective behavior.

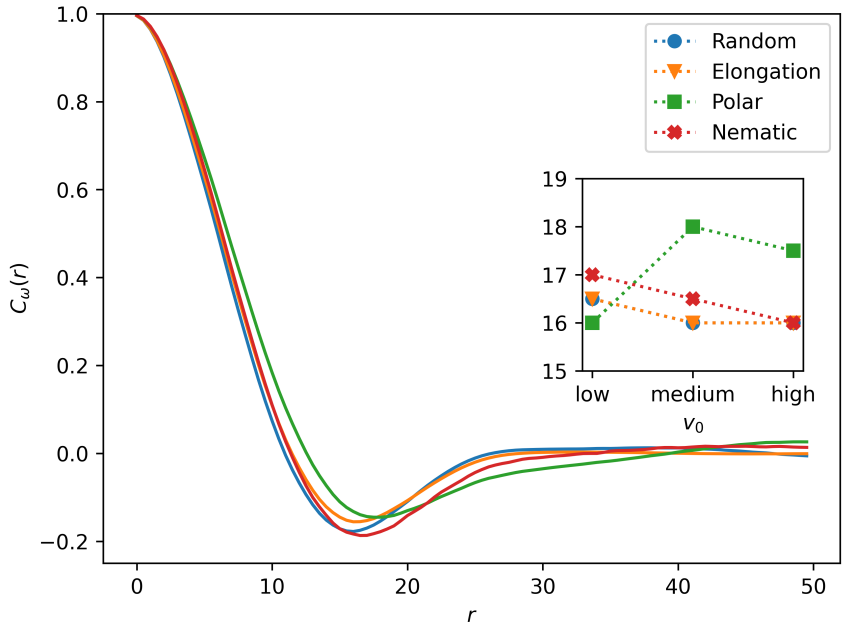

FIGURE 5.7: Vorticity-vorticity correlation function $C_\omega(r)$ depending on the distance r for all models. The data is averaged over 3 simulations with the "low" values for the self-propulsion velocity, see Table 5.2. The other values lead to qualitatively similar results. The inlet shows the position of the minima for the other activity values.

To quantify this further, we have measured the positions of the minima for the activity levels low, medium und high and visualized those in the inset of Figure 5.7. For the random, elongation and nematic model, the correlation length scale decreases for higher activity as typical for turbulent systems. In the polar model, we observe a different behavior which might again be due to collective phenomena, in our studies only occurring for this mechanism of propulsion.
We have observed that, in a certain parameter range of the activity, all models resemble certain phenomena of turbulent flows, like the occurrence of vortices with a significant length scale. While all studies in the chapter have been performed in a system with periodic boundaries, representing a large, confluent monolayer of cells, a variety of experimental data is available for confined systems. We will use the next section to investigate how the geometry influences the dynamics by using a confined setup.

5.5 | OSCILLATIONS IN CONFINEMENT

The geometry is a key factor in the evolution of flow and movement patterns in a variety of systems. In particular, for tissue, where experimental setups *in vitro* usually involve plating cells on a substrate with limited amount of available space, this is of major importance.
The first Multi-Phasefield simulations of such situations consider persistent rotational motion of two cells [Cam+14] on adhesive micropatterns. In this model, $\mathbf{v}_i$

follows from a reaction-diffusion equation to be solved within each cell. The emerging patterns in concentration of Rho GTPase define a polarity, which determines strength and direction of motion. For a more detailed modeling approach in this direction, we refer to [MV14a] and the references therein. Already these simulations, which consider the simplest possible collective motion, show a strong dependency of the emerging behaviour on subcellular features and substrate geometry.

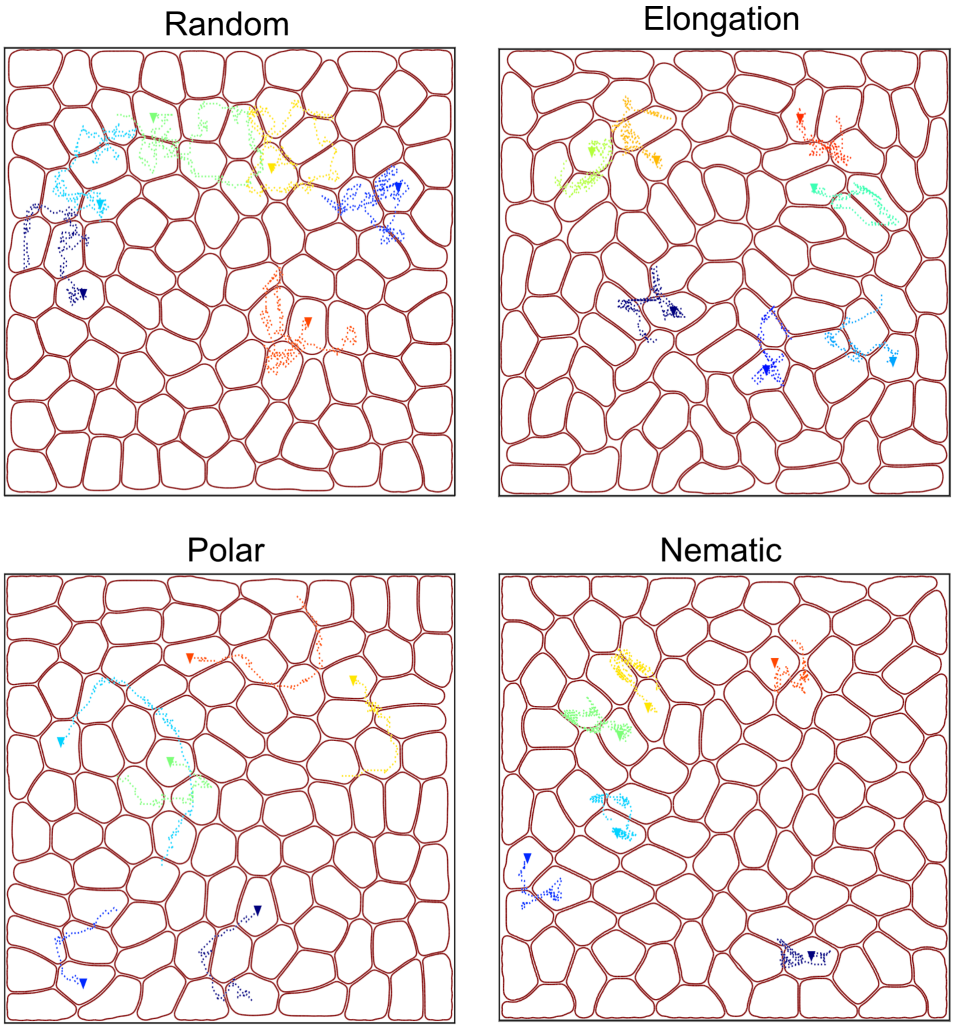

FIGURE 5.8: Cell shapes defined as the $\phi_i = 0$ levelset alongside trajectories for the center of mass for some individual particles in all models with medium values of activity according to Table 5.2. Different types of local oscillations can be observed.

Recent studies in [Pey+19], with more cells in a rectangular confinement could reproduce sustained oscillation experimentally observed for MDCK cells, human keratinocytes (HaCat) and enterocytes (CaCo2). The considered models in these studies are related to the elongation model. Here, we have performed a similar study for all four models in a square confinement modeled by the repulsive potential introduced in Section 3.5 and with the initial condition visualized in Figure 3.18 (Left). The resulting trajectories for the centers of mass of different cells alongside the $\phi_i = 0$ levelsets are depicted in Figure 5.8. We observe differences in the movement between

the models. While the polar model shows very long ranged movements, the trajectories in the random model cover shorter distances and are more strongly perturbed, likely due to the random advection. In the elongation and nematic model trajectories are shorter and thus resulting circular movements have smaller radii. We can, however, observe a certain type of rotational motion in all models, indicating that this local behavior is indeed mostly guided by the geometry and not the mechanism of propulsion.

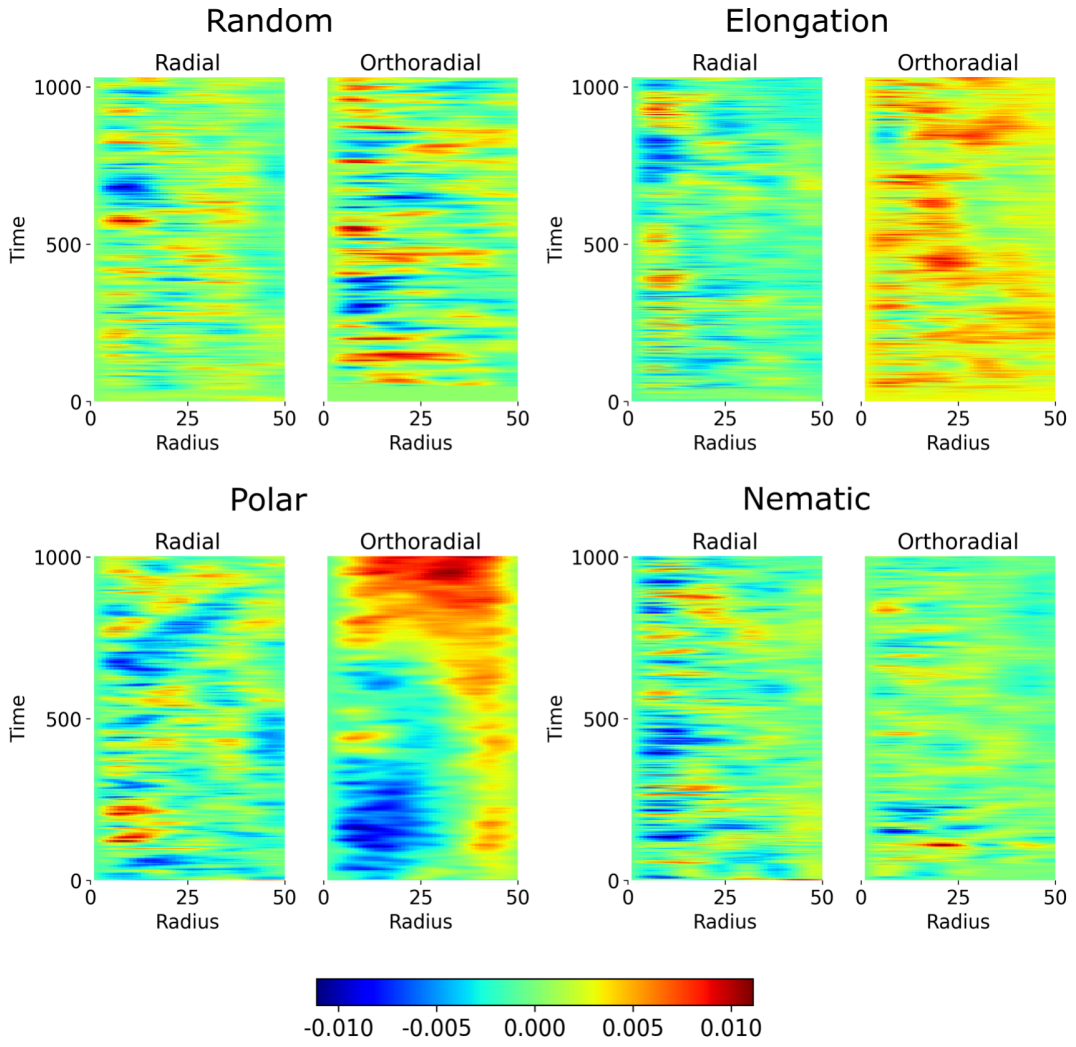

FIGURE 5.9: Kymographs of radial and orthoradial velocity components for the four models: random, elongation, polar and nematic, from left to right.

Now, we focus on a slightly different experimental setup by changing the confinement shape to a circle and the corresponding initial structure depicted in Figure 3.18 (Right). In particular, we compare the four models with experiments on MDCK cells in circular confinements as performed in [Dox+13; Def+14]. The studies show that confined epithelia exhibit collective low-frequency radial displacement modes and rotational motion, which was partly reproduced in corresponding particle-based simulations [HS17].

The circular geometry allows to split the velocities $\mathbf{v}_i$ into radial and orthoradial components $\mathbf{v}_i^{radial}$ and $\mathbf{v}_i^{ortho}$, given by

$$\mathbf{v}_i^{radial} = \mathbf{v}_i \cdot (\mathbf{x}_i - \mathbf{c})$$
$$\mathbf{v}_i^{ortho} = \mathbf{v}_i \times (\mathbf{x}_i - \mathbf{c})$$

for cell position $\mathbf{x}_i$ and domain center $\mathbf{c}$. The mean spatial distribution results from an averaging over all cells with similar distance from the center.
These values are shown in Figure 5.9 for all four models. While the radial component is qualitatively similar in all four models, the orthoradial component qualitatively differs between the models. Only the polar model could reproduce the rotation of the monolayer as a whole and a change in direction of the interior part, which is assumed to be responsible to a comparable size of the confinement and the spatial scale resulting from the vorticity-vorticity correlation in Figure 5.7. The simulations are performed with the medium values in Table 5.2.

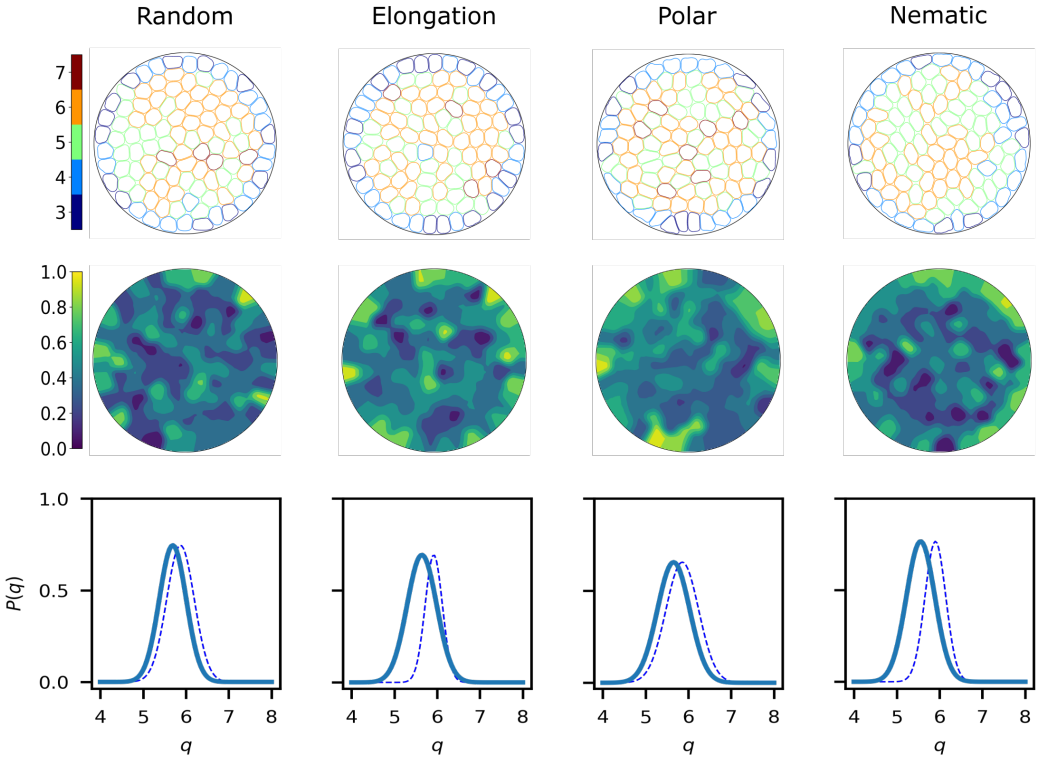

FIGURE 5.10: (First row) Cell morphology and number of neighbors. (Second row) Time averaged bond number. (Third row) Coordination number probability computed excluding cells in contact with confinement. The corresponding values from Figure 5.3 without confinement are shown for comparison (dashed curves).

To further analyze the emerging properties in the circular confinement, Figure 5.10 shows snapshots of the configuration, highlighting the cell morphology and their neighbour relations. We also compute the bond number

$$\Psi_6^j = \frac{1}{|N_j|} \left| \sum_{k \in N_j} e^{6i\theta_{jk}} \right|$$

for N_j the set of neighbors, θ_{jk} the angle between $\mathbf{x}_j$ and $\mathbf{x}_k$ and i the imaginary unit.

If $\Psi_6^j = 1$ for some cell, all neighbors are in perfect hexagonal arrangement while the value 0 represents isolated cells, see [Loe+20]. The quantity is computed locally and averaged over time, essentially showing a global liquid like behavior for all four models. The coordination number probability is computed as in Figure 5.3, but excluding the cells in contact with the confinement. All four models show a decrease in the mean value as a result of the confinement. The elongation and nematic models also show an increase in the variance if compared with the results in Figure 5.3 and thus indicate a shift of the solid-to-liquid transition towards lower activities in the phase diagram.
In real systems, confinement has a tremendous effect on the emerging macroscopic behaviour and might even induce morphogenesis-like processes. Our simulation results indicate that the emerging behavior in confinements strongly depends on subcellular details and the way how activity is enforced on the cellular level in the modeling approach. While the emerging local oscillations in rectangular confinements are similar, even though the length scales differ, the emergence of global oscillations in round confinements strongly depends on the mechanism of activity.

5.6 | CONCLUSIONS

We use Multi-Phasefield models with four different mechanisms of propulsion to analyze confluent and confined monolayers of deformable cells. Various of the known generic features of confluent monolayers are reproduced by all four models, highlighting the robustness of these features on microscopic details. This includes a solid-to-liquid transition, which leads after appropriate calibration of parameters to similar phase diagrams as obtained with vertex and voronoi models [Bi+16]. Other common features are the spontaneous formation of vortices as well as the emergence of active turbulent flows.
However, the four models also lead to different results if more quantitative measures are considered. This becomes apparent for the deformation of cells. While the shape variability of the cells can be described by a k-Gamma distribution over a broad range of parameters for all four models, the narrow range of the parameter k, found in [Ati+18] for various epithelia systems, could only be reproduced by the elongation and polar model. Not only geometrical properties of the cells, also topological features differ between the four models. The ratio of multicellular rosettes depends on the microscopic details. As these rosettes provide an efficient mechanism for tissue remodeling, see e.g. [YB19], these differences need to be considered in further model extensions. Simulations in confinement reveal further differences of the models. Induced global rotation, as observed in circular confinements for MDCK cells in [Def+14; Dox+13] and reproduced by particle-based simulations [HS17] could only be observed with the polar model.

6 | Cellular Structures as Active Nematics

Over the last years, it has been a growing focus of interest to investigate cellular structures in terms of their alignment and deformation structure. To be more precise, it has been observed that different systems resemble a behavior known from liquid crystals, namely a long range orientational order structure and the occurrence of topological defects.

The nematic phase is typically characterized by (partial) alignment of rod-shaped particles, with local defects in the orientation, see Section 2.4 for more details. For elongated bacteria or subcellular filament structures, the connection to living systems is rather obvious, see [FKF93] and [Del+18]. On the other hand, even for epithelia tissue, composed of fairly isotropic cells, a certain nematic order has been observed, which is less obvious. The main focus of this chapter will be an investigation of the previously introduced Multi-Phasefield models in terms of arising nematic structure, in order to elaborate their capabilities in the representation of epithelial tissue further.

One of the most common ways of investigating nematic behavior is through the topological defects in the orientation fields. These are regions, where the nematic order is lost, in order to minimize stresses. Defects are characterized by a topological charge, in the mathematics community also sometimes called the winding number. From theory and experiments on nematic systems, it is known that $\pm\frac{1}{2}$ defects are energetically most favorable in two-dimensional systems, classifying them as perfect focus for the following investigations.

In comparison to liquid crystalline materials, however, living systems are usually driven by active forces. Thus, we compare our findings with active nematic structures, characterized by spontaneous changes in the orientation fields, leading to generation and annihilation of topological defects. It has been proposed in [GD14] that $-\frac{1}{2}$ defects in active nematics are moved around passively, while $+\frac{1}{2}$ defects behave as self-propelled particles, with velocities proportional to activity. The latter relation can in turn provide a way to estimate activity in living systems, by measuring the

velocities of defects in the nematic alignment.
The motion of defects does not only allow to measure activity, it also provides a good way of distinguishing extensile and contractile behavior in living systems. For extensile systems, $+\frac{1}{2}$ defects move towards their 'head', as has been shown experimentally for microtubule (MT) bundles [San+12], human bronchial epithelial cells [BM+18] and Madine Darby Canine Kidney (MDCK) cells [Saw+17], whereas for contractile systems they move towards their 'tail', which has been observed in experiments on mouse fibroblast cells [Duc+17]. In [Saw+17] it was found that near $+\frac{1}{2}$ defects the rate of apoptosis of MDCK epithelial cells is higher, due to the presence of isotropic compressive stresses. In contrast, the $-\frac{1}{2}$ defects are characterized by tensile stresses and do not trigger apoptosis. In [KKS17], collective dynamics of cultured murine neural progenitor cells (NPCs) are studied. At high densities, the cells were capable of forming an aligned pattern. Rapid cell accumulation at $+\frac{1}{2}$ defects and escape from $-\frac{1}{2}$ defects has been identified.

The structure of this chapter follows the goal of identifying and analyzing the topological defects in cellular alignments. In Section 6.2, we will introduce methods for the identification and tracking of topological defects in the nematic structure of Multi-Phasefield models for tissue, flexibly transferrable to experimental setups. Afterwards, we will test these methods, investigating the density, creation and movement of topological defects in Section 6.3. From these observations and an additional investigation of mechanical properties like velocities and derived strain rates in the vicinity of topological defects in Section 6.4, we are able to draw conclusions on the overall behavior of the system, depending on the mechanism of propulsion.

6.1 | Model Setup

In this chapter, we will use an almost identical setup compared to Chapter 5, namely 4 different mechanisms of propulsion with the common evolution equation

$$\partial_t \phi + v_0(\mathbf{v}_i \cdot \nabla \phi_i) = \Delta \frac{\delta \mathcal{E}}{\delta \phi_i},$$

varying in the choice of $\mathbf{v}_i$ and the system energy $\mathcal{E}$. For the sake of readability, we will use this section to shortly review the used models without going into detail. For more insights into the definition of the energy contributions and the mechanisms of activity, we refer to Section 3, while the derivation of the evolution equations is performed more in detail in Section 5.1.
The *random model* is given by the evolution equation

$$\begin{aligned}
&\partial_t \phi_i + v_0 \left(\mathbf{v}_i^{ran} \cdot \nabla \phi_i\right) = M \Delta \mu_i \,, \\
&\mu_i = \frac{1}{Ca}\left(-\epsilon \Delta \phi_i + \frac{1}{\epsilon} W'(\phi_i)\right) + \frac{1}{In}\left(B'(\phi_i)\sum_{j \neq i} w_E(d_j) + w_E'(d_i) d_i'(\phi_i) \sum_{j \neq i} B(\phi_j)\right)
\end{aligned}$$

with propulsion

$$\mathbf{v}_i^{ran} = \begin{bmatrix} \cos\theta_i \\ \sin\theta_i \end{bmatrix}$$

and the movement angle θ_i following the Wiener process $\mathrm{d}\theta(t) = \sqrt{2D_r}\mathrm{d}W_i(t)$.
The *elongation model* follows the partial differential equation

$$\begin{aligned}\partial_t\phi_i + v_0\left(\mathbf{v}_i^{elo}\cdot\nabla\phi_i\right) &= M\Delta\mu_i\,,\\ \mu_i = \frac{1}{Ca}\left(-\epsilon\Delta\phi_i + \frac{1}{\epsilon}W'(\phi_i)\right) &+ \frac{1}{In}\left(B'(\phi_i)\sum_{j\neq i}w_E(d_j) + w_E'(d_i)d_i'(\phi_i)\sum_{j\neq i}B(\phi_j)\right).\end{aligned}$$

with

$$\mathbf{v}_i^{elo} = \int_\Omega \tilde{\phi}_i\nabla\cdot\boldsymbol{\alpha}_{tissue}$$

and $\boldsymbol{\alpha}_{tissue} = -\mathbf{Q}$ the global deformation tensor defined in (3.22). For both the random and the elongation model, the whole state of the system is represented by the set of Phasefields $\{\phi_i\}$.
The *polar model* uses both Phasefields $\{\phi_i\}$ and polarization fields $\{\mathbf{P}_i\}$ to describe cell shapes and orientations. The evolution is given by

$$\begin{aligned}\partial_t\phi_i + v_0\left(\mathbf{v}_i^{pol}\cdot\nabla\phi_i\right) &= M\Delta\mu_i\,,\\ \mu_i = \frac{1}{Ca}\left(-\epsilon\Delta\phi_i + \frac{1}{\epsilon}W'(\phi_i)\right) &+ \frac{1}{Pa}\left(-\frac{1}{2}\|\mathbf{P}_i\|^2 - \beta\nabla\cdot\mathbf{P}_i\right)\\ &+ \frac{1}{In}\left(B'(\phi_i)\sum_{j\neq i}w_E(d_j) + w_E'(d_i)d_i'(\phi_i)\sum_{j\neq i}B(\phi_j)\right),\\ \partial_t\mathbf{P}_i = -\frac{1}{Pa}&\Big(-\phi_i\mathbf{P}_i + \|\mathbf{P}_i\|^2\mathbf{P}_i - \Delta\mathbf{P}_i + \beta\nabla\phi_i\Big).\end{aligned}$$

with propulsion defined by $\mathbf{v}_i^{pol} = \mathbf{P}_i$.
For the *nematic model*, we use Phasefields $\{\phi_i\}$ and Q-tensor fields $\{\mathbf{Q}_i\}$ to describe the cell shape and intracellular dynamics. To describe the evolution, we use partial differential equations

$$\begin{aligned}\partial_t\phi_i + v_0\left(\mathbf{v}_i^{nem}\cdot\nabla\phi_i\right) &= M\Delta\mu_i\,,\\ \mu_i = \frac{1}{Ca}\left(-\epsilon\Delta\phi_i + \frac{1}{\epsilon}W'(\phi_i)\right) &+ \frac{1}{Ne}\left(-\frac{1}{2}\,\mathrm{tr}\mathbf{Q}_i^2 + \gamma\nabla\cdot(\mathbf{Q}_i\nabla\phi_i)\right)\\ &+ \frac{1}{In}\left(B'(\phi_i)\sum_{j\neq i}w_E(d_j) + w_E'(d_i)d_i'(\phi_i)\sum_{j\neq i}B(\phi_j)\right),\\ \partial_t\mathbf{Q}_i = -\frac{1}{Ne}&\Big(-\phi_i\mathbf{Q}_i + \mathrm{tr}\mathbf{Q_i}^2\mathbf{Q_i} - \Delta\mathbf{Q}_i + \gamma\left(\nabla\phi_i\nabla\phi_i^T - ||\nabla\phi_i||^2 Id\right)\Big)\end{aligned}$$

and the propulsion

$$\mathbf{v}_i^{nem} = \nabla\cdot\mathbf{Q}_i.$$

We simulate the evolution equations in $\Omega\times[0,T]$ for a finite end time $T > 0$ and a two-dimensional rectangular domain Ω. In this chapter, we only consider periodic boundary conditions. For the simulation we use AMDiS with the cell-based parallelization as explained in Section 3.6. For the initial conditions, we always use the most simple configuration presented in Subsection 3.6.2, namely the brick-wall structure that was depicted in Figure 3.17 (Left). Additionally, we use the typical

setup for step size in time and space, in particular $h \approx 0.2\epsilon$ in the diffuse interface, $h \leq \epsilon$ in the interior and $h \leq 10\epsilon$ in the exterior while $\tau = 0.1$ is constant after a few relaxation steps with smaller time step. Just like in the previous chapters, we keep the parameter set constant. The values for all parameters, except the self-propulsion v_0, can be found in Table 6.1.

Ω	ϵ	M	In	Pa	Ne	β	γ	Ca
$[0,100] \times [0,100]$	0.15	1	0.025	1	1	0.01	0.1	0.0148/0.018

TABLE 6.1: Numerical parameters used in all simulations throughout Chapter 6.

In particular, for the deformability parameter Ca, two different values are given as there is a strong interplay with the activity v_0, leading to the solid-liquid transition studied in Section 5.2. For the activity levels, we choose two different general setups, similar to Chapter 5. If a dependence on the activity is required for the experimental setup, we again use the levels low, medium and high that have been already introduced in Chapter 5 alongside $Ca = 0.0148$, in order to ensure a liquid state. If, on the other hand, we require only a single level of activity with a setup as close as possible to experimental data, we use the value v_0^* derived in Subsection 5.3.2 according to the reported values in [Bla+06] in combination with $Ca = 0.018$. All considered levels of activity with their corresponding deformability parameter can be found in Table 6.2, for the four models.

	random	elongation	polar	nematic	Ca
v_0^*	1.3	0.6	1.3	19.0	0.018
low	1.2	1.0	1.2	21.0	0.0148
medium	2.4	2.0	2.4	24.0	
high	3.6	3.0	3.6	30.0	

TABLE 6.2: Activity levels v_0 for the four models with their corresponding deformability parameter Ca used throughout Chapter 6.

6.2 METHODS

An investigation of nematic order structure is usually an investigation of the topological defects in the orientation field. How a nematic ordering can be identified in cellular structures and, in particular, how it is possible to identify and track defects, is not a trivial question. We will use this chapter to present a robust set of methods, relying solely on cell shapes - in the modeling approach of this thesis represented by Phasefields but easily transferrable to experimental setups.

6.2.1 GLOBAL ORIENTATION FIELD

The first step in the investigation of tissue from a nematic perspective is the definition of the global orientation field, i.e. a field of rod-like particles with head-tail symmetry. We will follow the concepts introduced in Section 2.3 and describe the system using a Q-tensor, see Definition 2. In particular, we will use the deformation tensor $\mathbf{S}_i$ for each Phasefield ϕ_i that was introduced in (3.19), leading to propulsion driven by cell shape in the elongation model.

To define the global field $\mathbf{Q}$, we use the same approach as in the elongation-based activity mechanism, namely the smooth, piecewise combination of individual deformations involving the rescaled Phasefield $\tilde{\phi}_i$ given by

$$\mathbf{Q} = \sum_i \tilde{\phi}_i \mathbf{S}_i = \sum_i \tilde{\phi}_i \begin{bmatrix} \int_\Omega \frac{1}{2}\left((\partial_y\phi_i)^2 - (\partial_x\phi_i)^2\right) & \int_\Omega -(\partial_x\phi_i)(\partial_y\phi_i) \\ \int_\Omega -(\partial_x\phi_i)(\partial_y\phi_i) & \int_\Omega \frac{1}{2}\left((\partial_x\phi_i)^2 - (\partial_y\phi_i)^2\right) \end{bmatrix},$$

which was already defined in (3.22). The director field is then given by the eigenvectors of $\mathbf{Q}$ corresponding to the positive eigenvalues and denoted by η^+. We observe that this approach defines a global director field, representing alignment in the tissue given by individual cell deformations.
Although this approach already creates a well-defined global quantity, it is usually appropriate to apply a smoothing filter, e.g. of Gaussian type, to create more regular transitions between individual cell deformations and thus also visualize topological defects more easily. The process of defining local deformation tensors $\mathbf{S}_i$ with eigenvector η_i^+ and the corresponding global quantities is visualized in Figure 6.1.

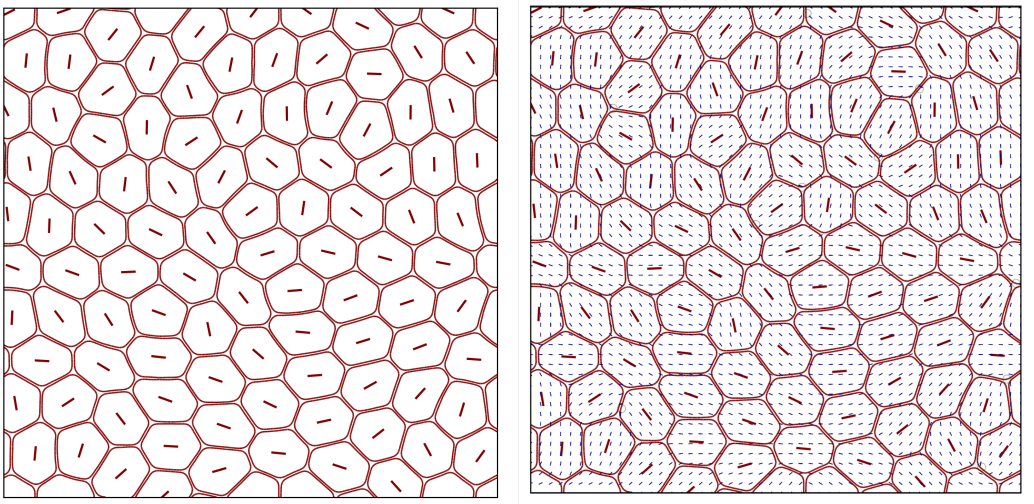

FIGURE 6.1: Definition of $\mathbf{Q}$ as continuos, smoothed combination of Phasefields ϕ_i and local deformation tensors $\mathbf{S}_i$. Visualized are the $\phi_i = 0$ levelsets, the local elongation of each Phasefield ϕ_i represented by the eigenvector η_i^+ (red) and the resulting global field of eigenvectors η^+ (blue).

Even though the approach is perfectly suited for Phasefield type descriptions and was developed for those, it also transfers straight forward to experimental data. For example in epithelial tissue, a pre-processing is necessary, e.g. using image segmentation methods like the one proposed in [LK11] for the transformation of real cell shapes into a Phasefield formulation.

6.2.2 | IDENTIFICATION AND TRACKING OF TOPOLOGICAL DEFECTS

To identify topological defects in the orientation fields of nematic structures, two main components play a role, namely the position and the topological charge (winding number). We will now construct a robust method, capable of finding those topological defects and afterwards determining their topological charge.

In order to find the positions of topological defects, it is crucial to recall [DH94] that they are singular points of the underlying tensor field

$$\mathbf{Q} = \begin{bmatrix} Q_0 & Q_1 \\ Q_1 & -Q_0 \end{bmatrix}.$$

As a consequence, a method to identify defect locations, can be constructed from the condition

$$Q_0 = Q_1 = 0,$$

which can be efficiently evaluated in a variety of implementations for post-processing, e.g. the filter CONTOUR in MATPLOTLIB for PYTHON.

Much more interesting is the identification of the topological charge q, sometimes also called winding number. It represents the number of rotations a director performs upon a full 2π rotation around the defect core. Defining the orientation angle

$$\Theta = \tanh\left(\frac{Q_0}{Q_1 + \sqrt{Q_0^2 + Q_1^2}}\right),$$

the winding number II is mathematically given as the contour integral

$$\mathrm{II} = \frac{1}{2\pi} \oint_C \mathrm{d}\Theta$$

for any closed curve C around the defect core.
In Figure 6.2, the rotation of the director for the two most common charges in two-dimensional nematic systems, namely $+\frac{1}{2}$ and $-\frac{1}{2}$, is visualized. It is, however, numerically sometimes problematic as the definition of a contour integral is not optimal for discrete data.
Different alternative approaches to determine the topological charge have been proposed. We have, for example, successfully implemented and tested an algorithm involving an artificial neural network to deal with this problem, details can be found in [Wen+20]. For this thesis, we will however focus on a more physical approach inspired by the work in [DH94]. Keeping in mind that the defects are singular or degenerate points in the field $\mathbf{Q}$, we can compute the sign of the degeneracy by

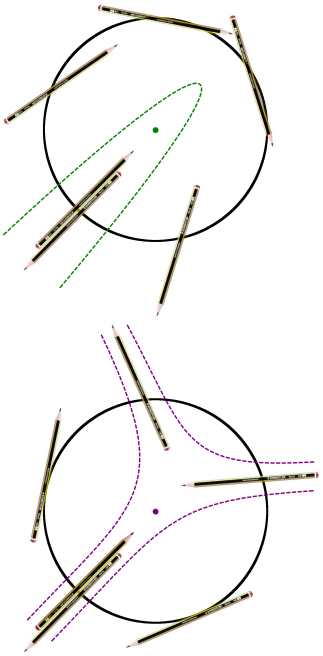

FIGURE 6.2: Schematic visualization of a director rotating around a defect core with $+\frac{1}{2}$ (top) and $-\frac{1}{2}$ (bottom) charge. Taken from [Wen+20].

$$\delta = \frac{\partial Q_0}{\partial x}\frac{\partial Q_1}{\partial y} - \frac{\partial Q_0}{\partial y}\frac{\partial Q_1}{\partial x} \tag{6.1}$$

and then use the result in [Del95] to conclude

$$\mathrm{II} = \frac{1}{2}\mathrm{sign}\,(\delta)\,. \tag{6.2}$$

This approach has a variety of advantages, the most relevant one being the uncomplicated numerical realization. With this, we are able to locate the positions of defects and also identify the topological charge, both easily computable from the components of $\mathbf{Q}$. The process of detection and identification is visualized in Figure 6.3.

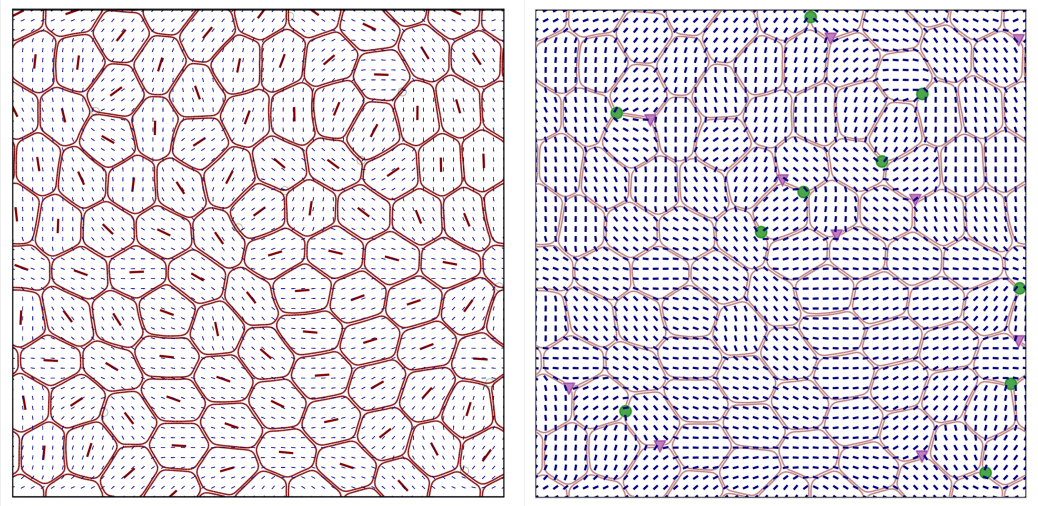

FIGURE 6.3: Detection and identification of topological defects in the alignment of Multi-Phasefield structures. Visualized are the $\phi_i = 0$ levelsets, the local elongation of each Phasefield ϕ_i represented by the eigenvector η_i^+ (red), the resulting global field of eigenvectors η^+ (blue) and the resulting $+\frac{1}{2}$ (green) and $-\frac{1}{2}$ (purple) defects.

With known defect positions and charges in each time frame, we have to connect them from frame to frame. Dozens of software tools have been developed for this task in the context of particle tracking, see e.g. [MDS12] for a review. For a more detailed comparison of these methods, we refer to [Che+14]. We here use an approach described in [SK05]. It involves finding a set of associations between the defect locations in subsequent frames such that a cost functional is minimized. It is based on a particle matching algorithm using a graph theory technique. We use the algorithm for $+\frac{1}{2}$ and $-\frac{1}{2}$ defects individually, treating them as independent particle types to avoid associations between defects of different charge. The tool is available as a plugin for ImageJ and Fiji (www.imagej.net), see [Sch+12].

6.2.3 | DEFECT-ALIGNED AVERAGING

It is common for active nematic systems to express significant patterns for different physical quantities in the vicinity of topological defects. For example, the average velocity fields and resulting strain rates but also the average isotropic stresses have been observed to express significant structure close to $+\frac{1}{2}$ and $-\frac{1}{2}$ defects, see e.g. [Doo+18]. These patterns are usually aligned with the orientation of the topological defects, for example tail-to-head flow in MDCK monolayers has been observed in [Bal+21], indicating extensile behavior.
For these investigations, it is crucial to have efficient methods for an averaging that takes the orientation of the defect into account. In review of Figure 6.4, we recall that $+\frac{1}{2}$ defects have exactly one orientation while the directors form a tri-fold for defects with $-\frac{1}{2}$ charge. For the sake of simplicity, we will from here on out restrict the averaging of physical properties to $+\frac{1}{2}$ defects to overcome this difficulty.

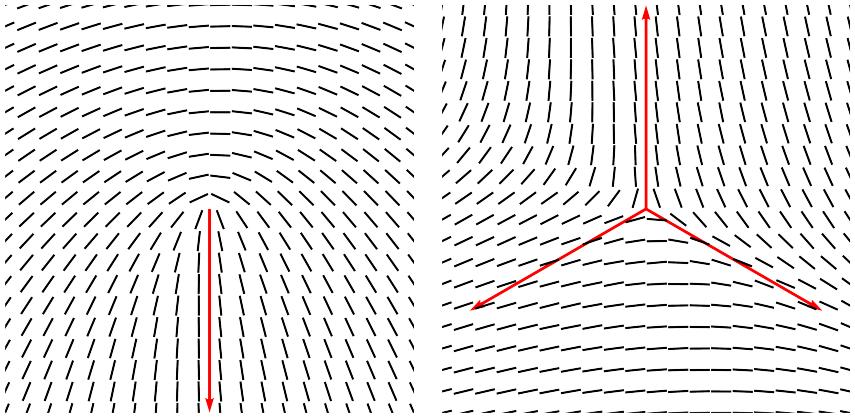

FIGURE 6.4: Schematic visualization of $+\frac{1}{2}$ (left) and $-\frac{1}{2}$ (right) defects with corresponding orientations indicated by red arrows.

The orientation of each defect can then be computed from the director field, in our case the eigenvectors η^+ of $\mathbf{Q}$. In particular, we define the quantity

$$\mathbf{p} = \frac{\nabla \cdot (\eta^+ \otimes \eta^+)}{|\nabla \cdot (\eta^+ \otimes \eta^+)|}.$$

At the position of a $+\frac{1}{2}$ defect, and also in its vicinity, the vector $\mathbf{p}$ represents the defect orientation, pointing from defect core to its tail. It is sufficient to compute this quantity locally, in a small box around every $+\frac{1}{2}$ defect. Given $\mathbf{p} = (p_1, p_2)$ for each defect k, the orientation angle ρ_k can be computed by

$$\rho_k = \arctan\left(\frac{\mathbf{p}_2}{\mathbf{p}_1}\right).$$

The most crucial step in the design of our algorithm for the averaging procedure with respect to every individual angle ρ_k, is the definition of a new coordinate system for each defect. In a continuos formulation, the coordinate system can be seen as rotated polar coordinates. For a point (x, y) in Cartesian coordinates, the radius variable $r(x, y) = x^2 + y^2$ is computed just as usual while the angular variable $\tilde{\theta}(\rho_k; x, y) = \tanh \frac{y}{x} + \rho_k$ is shifted by the angle of the current defect. The ρ_k-aligned averaging of a quantity $\mathbf{v}_k$ over N defects, given in this coordinate system, is then simply given by

$$\overline{\mathbf{v}} = \frac{1}{N} \sum_{k=1}^{N} \mathbf{v}_k(r, \tilde{\theta}).$$

To generate the discrete set of points with respect to this coordinate system, we have chosen to use an arrangement of points in multiple circles of increasing radii while the number of points in each circle also depends on the radius. This neglects the box corners, but for an appropriate choice of the box, this is far enough from the defect core.
Figure 6.5 visualizes the definition of the round coordinate for two exemplary orientation angles, indicated by the red arrow in analogy with Figure 6.4. We observe that points of equal position, with respect to the defect orientation $\mathbf{p}$, have the same color coding, i.e. the same index. For any quantity interpolated on this set of points, the ρ_k-aligned averaging is then given by a simple summation.

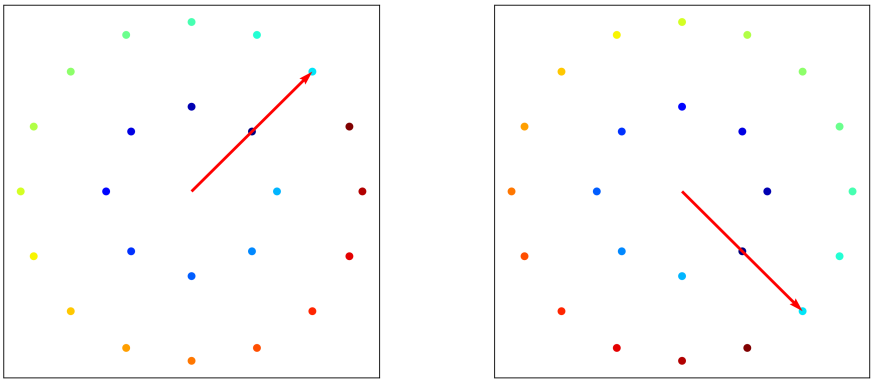

FIGURE 6.5: Visualization of round coordinates for a given defect orientation with $\rho_k = \frac{\pi}{2}$ (left) and $\rho_k = -\frac{\pi}{2}$ (left). The arrow represents $\mathbf{p}$ while the dots are the grid points. The color scheme for the dots represents their index from dark blue to dark red.

In this section, we have derived a powerful set of methods for the efficient identification and tracking of topological defects in the nematic alignment of cellular structures, that can also be transferred to experimental setups. Furthermore, we have invented a simple method to compute defect-aligned averages. We will use the rest of this chapter to apply these methods to different setups, in order to gain a deeper understanding into the nematic structure of Multi-Phasefield models for cellular structures. In particular, we want to analyze how the mechanism of activity influences these alignments.

6.3 | DENSITY, CREATION AND MOVEMENT OF TOPOLOGICAL DEFECTS

Having introduced a set of methods for the location, identification and tracking of topological defects in the nematic alignment structure of tissue, we want to investigate their dynamics. In particular, it is of interest to analyze the density and creation rates of topological defects, depending on the level of activity. Furthermore, we want to investigate their movement speed and direction, as this can give strong indications on the nematic structure of the system in general, e.g. if contractile or extensile behavior dominates.
It has been observed in [Saw+17] how the defect dynamics depend on the levels of activity in epithelial structures. In particular, a monolayer of Madine Darby Canine Kidney (MDCK) cells was treated with blebbistatin to reduce the activity. A clear correlation, validated by washout of the blebbistatin to increase restore wild-type activity, between activity and the density of defects has been observed.
We compute both the density of topological defects and the related creation rate for the three levels of activity named low, medium and high that are given in Table 6.2. The density is defined as the average number of defects per time frame while the creation rate measure the number of defects that occur for the first time in a given frame. The results are shown in Figure 6.6, averaged over many timesteps. The experimentally predicted increase in the defect density is qualitatively reproduced by the random, elongation and polar model. The nematic model shows slight deviations with no consistent slope. The behavior correlates with the defect creation

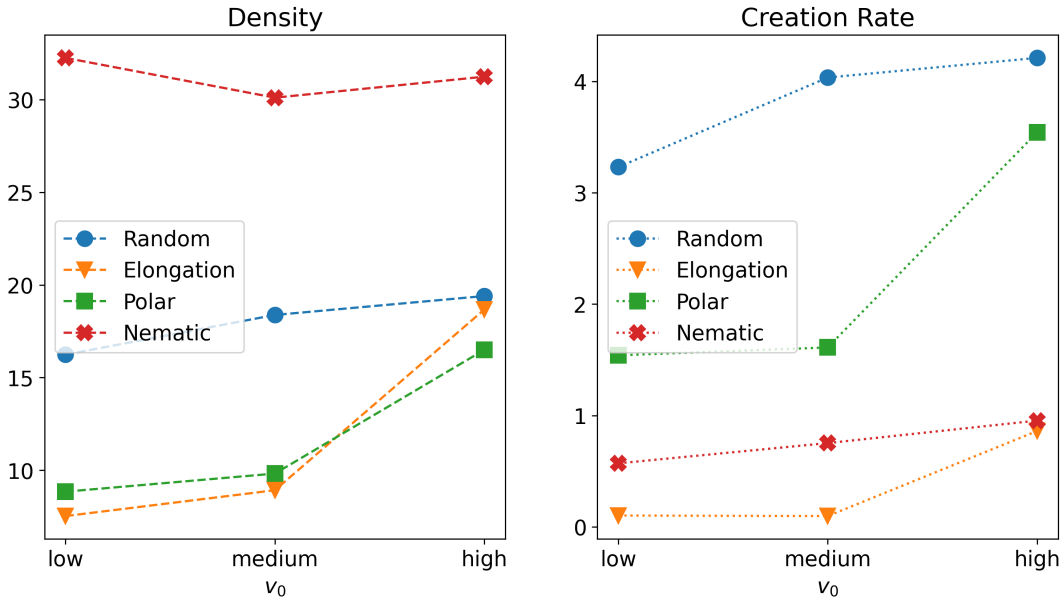

FIGURE 6.6: Average density (left) and creation rate (right) of topological defects for all four models and the levels of activity found in Table 6.2.

rate. Comparing the absolute values, the nematic model leads to significantly larger defect densities but lower creation rates, which indicates stronger persistence of defects. On the contrary, the random model leads to significantly larger creation rates, which might be explained by the random component of the model.
While we observe slight deviations between the mechanisms of activity in terms of the density and creation rate of topological defects, the overall qualitative behavior is quite similar. To isolate the dependence on mechanism of propulsion from the level of activity, given by v_0, we now go one step further and concentrate on the significant value v_0^* given also in Table 6.2. This creates a topologically equivalent setup for all four models based on experimental data, see Subsection 5.3.2.
We start with an examination of the velocity distributions for topological defects. To do this, we perform long time simulations, identify and track the topological defects with the methods presented in Section 6.2 and then analyze defect trajectories. The velocity is then simply defined as a backward difference between the positions of a single defect in two consecutive time frames.
In Figure 6.8, we have visualized histogram data on the defect velocities gathered from long time simulations for all four models. We can observe similarities in the overall distribution, for example a higher number of low velocities which is not surprising. It is, however, obvious from these results that significant differences are present, for example the average velocities which we have printed in Table 6.3 for easier access to the quantitative results.

	random	elongation	polar	nematic
$+1/2$	0.975	0.748	0.635	0.276
$-1/2$	0.930	0.673	0.671	0.312

TABLE 6.3: Average velocities for $+\frac{1}{2}$ and $-\frac{1}{2}$ defects for all 4 models.

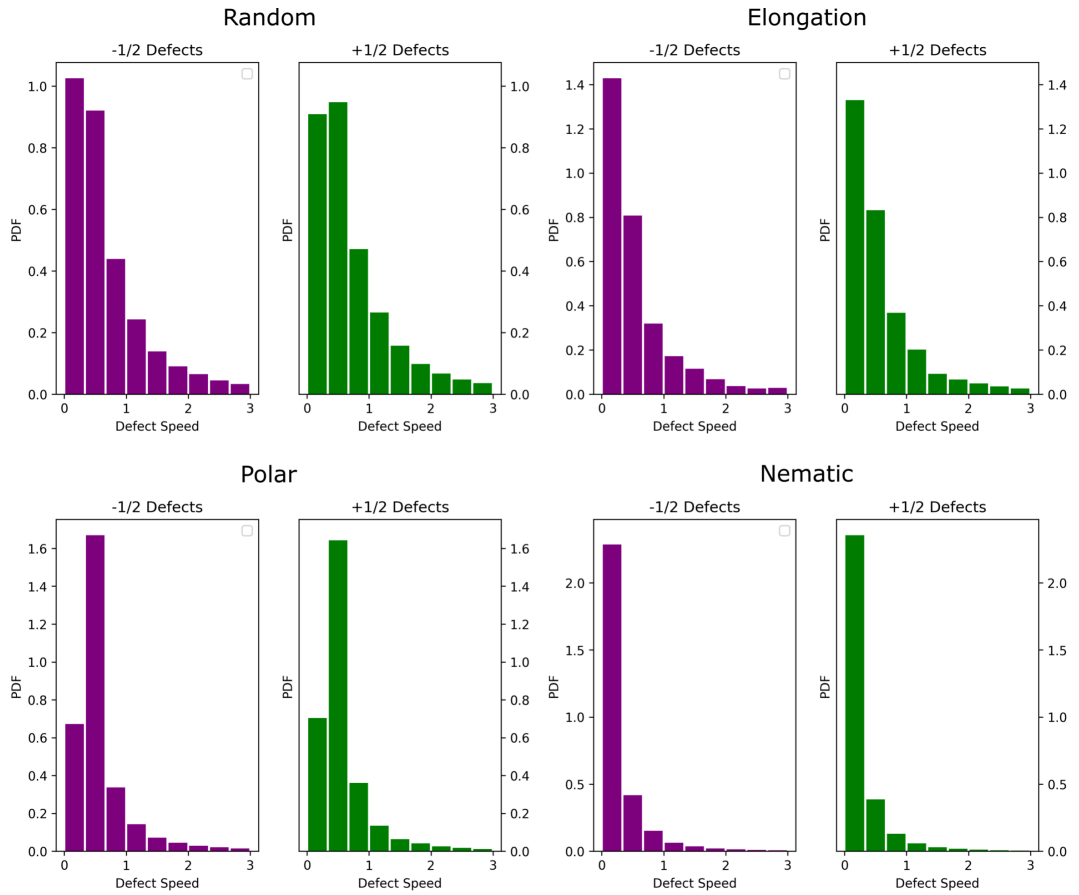

FIGURE 6.7: Velocity distribution of $+\frac{1}{2}$ (green) and $-\frac{1}{2}$ (purple) topological defects for all four models: random, elongation, polar and nematic, from top-left to bottom-right.

While the average velocities of topological defects strongly differ between the four models, the velocity distribution of $+\frac{1}{2}$ and $-\frac{1}{2}$ defects is always quite similar. This shows a qualitative difference to coarse grained active nematodynamics and experimental data, e.g. for active microtubule networks, see [DeC+15] or [OD16]. Detailed data on the velocity distribution of $+\frac{1}{2}$ and $-\frac{1}{2}$ defects for epithelia cell cultures are not separately available. However, for HBECs, [BM+18] indicates no apparent quantitative differences between both types of defects in terms of their trajectories on long time scales, which might support the simulation results. However, differences between $+\frac{1}{2}$ and $-\frac{1}{2}$ defects become evident if the direction of the defect velocity is correlated with the local properties of the defect. Figure 6.8 shows the distribution of directions with respect to symmetry properties of $+\frac{1}{2}$ and $-\frac{1}{2}$ defects. While the velocity of $-\frac{1}{2}$ defects does not show any preferred orientation for all models, which supports the passive (diffusive) role of these defects, the velocity of $+\frac{1}{2}$ defects is strongly correlated with the head or the tail of the defect. Only the random model does not show this property. All other models support the active role of $+\frac{1}{2}$ defects in active nematic systems [Doo+18]. The elongation model shows a strong correlation of the direction of movement with the head of the defect, indicating extensile behaviour. The polar and nematic model show a stronger correlation with the tail of the defect, indicating contractile behaviour. For a detailed discussion of these relations in active nematics we refer to [GD14].

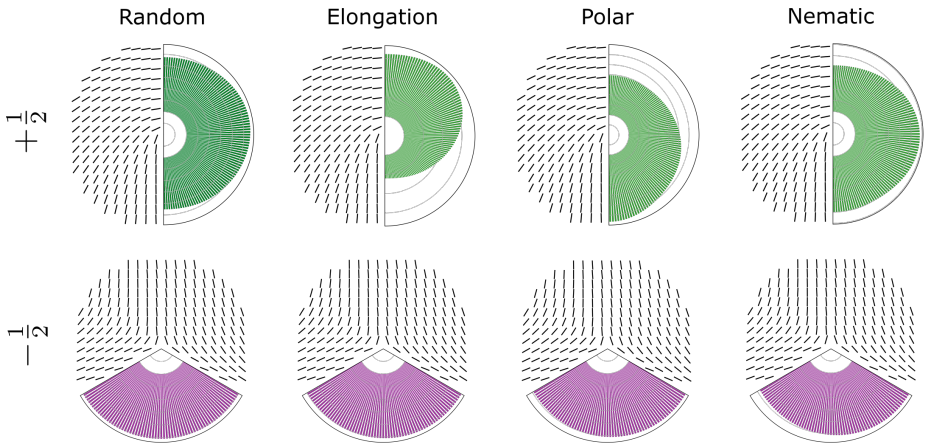

FIGURE 6.8: Distribution of direction of motion with respect to symmetry properties of $+\frac{1}{2}$ (top, green) and $-\frac{1}{2}$ (bottom, purple) defects for all four models. A schematic description of the defects defines the considered symmetry.

The observation of extensile behavior in the elongation model and contractile behavior for polar and nematic model is in agreement with the results in Table 6.3. In [Bal+21] the average velocity in monolayers is compared between extensile and contractile systems at similar density, with larger velocities for the extensile system. This is represented by the fact that the elongation model has higher average defect velocities than the polar and nematic model. The even higher number for the random model results from the large velocity fluctuations in this model.
The studies in this chapter have given a first deep insight into the dynamics of topological defects in the nematic alignment of cellular structures. We have observed strong similarities in the density and creation rate and at least qualitatively similar behavior in terms of the velocity distribution. The absolute values of the velocity have shown significant differences between the four models, even more strongly visible when taking the alignment with the head-tail direction of the defect into account. The results have indicated that the elongation model produces extensile behavior while the polar and nematic model show contractile movement patterns. We will use the rest of this chapter to investigate this difference more in depth by analyzing patterns in physical quantities, close to topological defects.

6.4 | MECHANICAL PROPERTIES IN THE VICINITY OF TOPOLOGICAL DEFECTS

On the single-cell level, contractile behavior is very common and extensively studied, e.g. in [SS02]. This property was also reproduced in computational models for single cells, for example in [MV14a]. On the tissue scale, however, the behavior is less clear and has only started to be a focus of interest in recent years. While fibroblasts have been observed in [Duc+17] to behave as a contractile system, the results for epithelial systems show the opposite behavior. Extensile behavior has been observed for MDCK in [Saw+17], for HBEC in [BM+18] and for neural progenitor cells in [KKS17].
The particular mechanism behind the emergence of contractile or extensile behavior on the large scale is still not fully understood. However, experimental results in [Bal+21] have strongly contributed to a deeper understanding. Occurring patterns

in the strain and stress in the vicinity of topological defects have been measured for two experimental setups using MDCK tissue, one with wild-type cells and the other one using E-cadherin knockout, effectively removing intercellular forces. Interestingly, while the experiments in the wild-type culture have confirmed prior observations of an extensile behavior, the E-cad knockout has led to strain and stress patterns known for contractile systems. Furthermore, the experimental results were validated using a Phasefield model, involving essentially two different contributions to activity, namely an elongation-based approach similar to the one used in this thesis and a polar force from contact inhibition with neighboring cells. In the presence of both contributions, the simulation results have shown extensile behavior while a contractile behavior was observed upon removal of the elongation-based activity.
We want to clarify the dependence of the emerging behavior on the underlying mechanism of activity with the four models introduced before. For this, we consider the strain rate tensor

$$\mathbf{E} = \frac{1}{2}(\nabla \mathbf{v} + (\nabla \mathbf{v})^T), \tag{6.3}$$

depending on the tissue velocity $\mathbf{v}$. As before, in Section 5.4, we define $\mathbf{v}$ as a global interpolant of $(\mathbf{x}_i, \mathbf{v}_i)$ onto a globally equidistant grid with 1000×1000 points where $\mathbf{x}_i$ is the center of mass and $\mathbf{v}_i$ the individual velocity of ϕ_i, computed using a backward difference.
We run simulations for the significant propulsion values v_0^* in all models over a long time and identify the topological defects in each time instance. For the purpose of identifying the clear patterns in the strain rate, we focus solely on defects of charge $+\frac{1}{2}$, in order to compare with the results in [Bal+21]. For every defect, we compute the orientation $\mathbf{p}$ and a $\mathbf{p}$-aligned coordinate system, see Section 6.2. With respect to this coordinate system, we compute an average of $\mathbf{v}$ in the vicinity of the defect, over a large number of individual defects, and the resulting average of the strain field $\mathbf{E}$ defined in (6.3).
With the exception of the random model, which does not show any significant pattern, the other models support our hypothesis. The elongation model leads to patterns characteristic for extensile systems, while the polar and nematic model show patterns characteristic for contractile systems. The strain rate along the tail-to-head direction (yy-strain) shows negative (positive) values at the head indicating the presence of compression (extensional deformation). The extensile behavior of the elongation model has already been found in [MYD19]. The model is constructed to elongate the cell further along its long axis, see definition of $\mathbf{v}_i^{elo}$ and Figure 3.12. Due to the interaction of cells, this behaviour leads to extensional deformations. Furthermore, it is the only of the four models that actively incorporates contributions from neighboring cells into the activity, given by the global deformation tensor defined in (3.22). For the polar model the contractile stress on the single cell level also generates contractile behavior at the collective level. In the nematic model the behavior on the single cell level strongly depends on the shape of the cell. However, the collective behavior shows contractile patterns. For the random model there is neither coupling of the activity with the individual shape nor with the neighboring cells, explaining why no significant patterns can be observed.

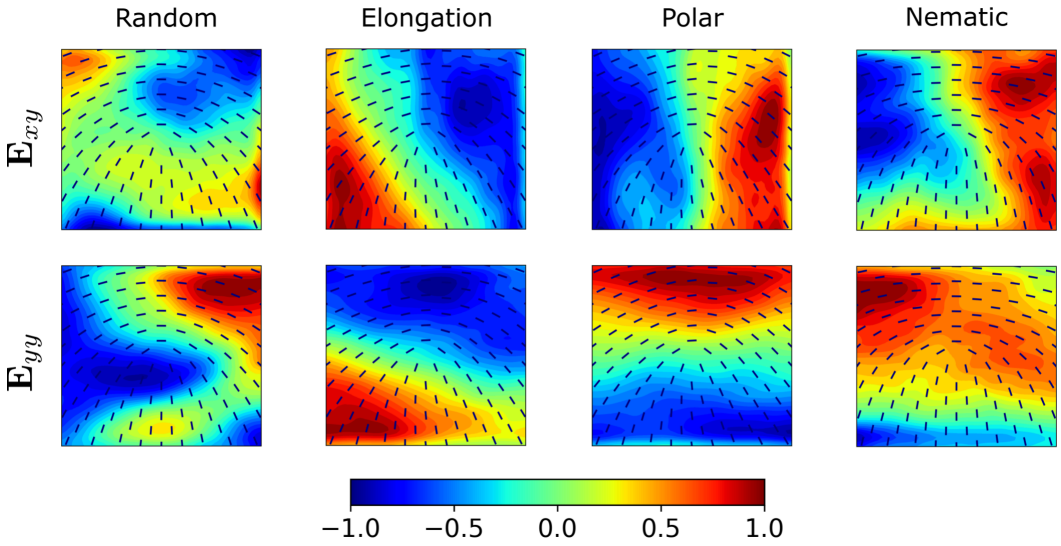

FIGURE 6.9: Average fields for both the xy component (top) and the yy component (bottom) of the strain rate tensor $\mathbf{E}$ in the vicinity of $+\frac{1}{2}$ defects for all models: random, elongation, polar, nematic from left to right. Each plot shows a box of dimension 8×8 centered at the defect core. The averaged is taken over data of more than 3000 defects for each model.

The findings are in good agreement with [Bal+21], strengthening the claim that intercellular forces are required for extensile behavior while a purely local propulsion mechanism, involving only the individual shape, propagates to a large scale contractile behavior. Furthermore, the studies are in perfect agreement with the findings in Section 6.3 about both the movement speed and direction of the topological defects. While for the random model large fluctuations and uncoordinated movement of defects is dominating, the elongation model shows clear extensile behavior. The polar and nematic model, on the other hand, show patterns resembling contractile systems, both in the directions of motion for topological defects and the strain rates in their vicinity.

6.5 | CONCLUSIONS

The investigation of cellular structures, in both experimental studies and simulations, from the viewpoint of nematic alignment patterns, has been growing interest over the last years. From large scale observations like flow patterns in HBEC as investigated in [BM+18] to local phenomena like apoptosis in MDCK, as found in [Saw+17], different phenomena have been identified to correlate with the dynamics of topological defects in the nematic order. In [Bal+21], it has been investigated how intercellular forces, regulated by E-Cadherins, influence the mechanical properties of the tissue and in particular switch the overall behavior between extensile and contractile.

In this chapter, we have investigated how these properties are reproduced in Multi-Phasefield models with different sources of activity. We have observed that certain generic features like the occurrence of topological defects can be observed in all setups, given a liquid state of matter. Furthermore, both the density and creation rate of the defects have been observed to increase with the level of activity, which is typical for active nematic structures.

Investigating, on the other hand, the movement patterns of topological defects, we were able to observe significant differences in both the velocities and the directions. For the random model, large velocities and no correlations between defect orientation and movement have been observed which can be explained by the stochastic driving mechanism. Interestingly, while the elongation model was also showing large velocities, the direction of movement for $+\frac{1}{2}$ defects was strongly correlated with the defect head, indicating an extensile behavior. For both the polar and the nematic model, observed velocities were lower and a preferred movement towards the defect tail was found for $+\frac{1}{2}$ defects, a behavior common in contractile systems. By analyzing the emerging patterns of the strain rate in the vicinity of $+\frac{1}{2}$ defects, these observations were confirmed - no significant structures was visible for the random model while the elongation model resembled extensile behavior and both polar and nematic model have shown patterns known for contractile systems.
In conclusion, we have found that the elongation model, effectively increasing elongations of individual cells, produces extensile behavior on the multicellular level. In the polar model the contractile behavior on the single cell level carries over to the multicellular level and also the nematic model, where the properties on the single cell level depend on shape, leads to contractile behavior on the multicellular level. As suggested by the experiments in [Bal+21], these observations might be influenced by changing the cell-cell interaction potential, for example to include adhesive forces.

7 | Conclusions, Extensions and Outlook

Understanding cells, the essential building blocks in the creation of life, and their arrangement in complex multi-cellular structures is one of the greatest puzzles of modern time. From the question how life in its current form has developed to the design of groundbreaking methods for therapy and treatment, a variety of fields in modern research is circled around cells and their dynamics. While much of the mystery has been revealed until today, just as much is still unknown.
Simulation methods for *in silico* experiments on cellular structures have been grown in interest over the past decades, with a huge increase in most recent years, due to rapidly increasing computational resources. These types of model based experiments can give significant insight into the dynamics, as individual aspects like intercellular bonds or the mechanisms for propulsion can be investigated, isolated from other effects at very low effort. A variety of approaches has been proposed, with individual up- and downsides, different levels of detail and varying computational effort.

7.1 | Conclusions

We have introduced a set of Multi-Phasefield methods with different mechanisms of propulsion, in order to analyze confluent monolayers of deformable cells. The advantage of such a modeling approach has been pointed out in various recent contributions like [Non12; Cam+14; Pal+15; MYD19; Loe+20]. Cell deformations and detailed cell-cell interactions, as well as subcellular details to resolve the mechanochemical interactions underlying cell migration, can naturally be handled. Furthermore, topological changes, such as T1 transitions, follow naturally in a Multi-Phasefield framework. Using an efficient, highly parallelized implementation and appropriate computing power, we have analyzed the emerging macroscopic behavior in such models and compared the results with known universal features of cell monolayers and epithelia tissue.
All models follow the same methodology and only differ at microscopic details on the incorporation of activity: The random model [Loe+20] determines the direction of motion on the single cell level by a stochastic process, the elongation model [MYD19] aligns the direction of motion with the long axis of the cell and both the polar [MV16] and the nematic model use subcellular details determining strength and direction of motion for each individual cell.
Firstly, we have investigated only the polar model, which has been observed to develop collective motion, depending on the shape-activity coupling strength. In particular, we have analyzed the alignment structures, depending on the degree of

orientational order. We have found that typical arrangements, for example quantified by Lewis' law and Aboav-Weaire's law, are fulfilled in situations where the cells are collectively moving. The fact that these purely geometrical laws are fulfilled in the Multi-Phasefield models, without the presence of any external guidance, e.g. concentration gradients in certain surrounding chemicals, indicates that cellular arrangement is strongly driven by geometrical and topological order structure.
Afterwards, we have concentrated all considerations on the emerging phenomena in dependence of the propulsion mechanism, as it is still not fully understand how cell movement is generated, an open question that was recently reviewed in [Bod+20]. We have shown that all four considered mechanisms experience a solid-liquid transition, which is relevant for example in tumor spreading, depending on activity and deformability. The distribution of cell shapes, experimentally predicted in [Ati+18] to be universal across a variety of organisms, was qualitatively found in all four models, with quantitative agreement only for the polar and the elongation model. We have found that multicellular rosettes, which have been observed to play a crucial role in developmental processes like Drosophila eye development [EBF07], occur in all models but the ratio of occurrence depends on the mechanism of propulsion. Regarding the cell flow in the simulated tissue structure, we were able to observe the occurrence of vortices with a significant length scale, almost identical for all models, and oscillatory movements in confined environments as known to occur for example for MDCK cells in [Dox+13].
Finally, we have focused on the perspective of nematic alignment in cellular structures. This viewpoint has become a stronger focus of research interest most recently, for example driven by observations in [Saw+17], indicating that cell death and extrusion in MDCK monolayers correlates with the occurrence of $+\frac{1}{2}$ topological defects. We have found that all models show topological defects, with both density and creation rate increasing for higher activity, while the absolute values of these quantities differ between the propulsion mechanisms. Striking differences have been found investigating the alignment of $+\frac{1}{2}$ defect orientations and their movement directions: strong correlations with the defect head have been found for the elongation model and similarly clear alignment in defect tail direction were observed for the polar model. In the nematic model, a slightly preferred movement towards the defect tail was seen, while no patterns were observed in the random model. For $-\frac{1}{2}$ defects all models have shown an almost equal distribution of movement directions. In combination with the observed defect velocities and an investigation of the strain rate tensor, aligned with the defect direction, we were able to conclude that the elongation model creates extensile behavior on the large scale, while both polar and nematic model resemble contractile systems. For the random model, no significant patterns were found, likely due to the activity mechanism that is fully decoupled from shape and alignment.
The comprehensive comparison of different Multi-Phasefield models for confluent cell monolayers shows the strong effect of the single cell activity mechanism. Furthermore, it highlights the importance of this modeling aspect for predictive simulation results at the multicellular level, significantly influencing features like occurring patterns in shape and flow or the dynamics of topological defects in the nematic structure. However, the results also show the robustness of these models in producing generic qualitative features for cell monolayers and epithelia tissue. The flexibility of Multi-Phasefield models, not only in terms of cell deformability and topological changes, such as T1 transitions, but also when incorporating mechanochemical effects on a single cell level and for cell-cell interactions, gives this modeling approach a huge potential for multiscale simulations of multicellular dynamics.

7.2 | EXTENSIONS OF THE MODELS

Even though the results in this thesis give a comprehensive study of Multi-Phasefield models for cellular structures, countless extensions are possible due to certain restrictions of the models. At this point, we want to focus on two particular aspects - tissue growth and geometrical changes of the domain - that have been investigated in student research projects during the work on this thesis. While the methods and studies presented in both 7.2.1 and 7.2.2 have been developed in close collaboration, the author of this thesis does by no means claim ownership of the results. However, we want to use this section to summarize the ideas, in order to emphasize how powerful the Multi-Phasefield approach in general is, but for any detailed insight into the models and results we refer to the respective master thesis mentioned in each subsection.

7.2.1 | GROWTH AND DIVISION OF CELLS

It is well-known that tissue structures, for example epithelial monolayers, undergo multiple changes before a state of confluence - which was a general assumption in all previous studies of this thesis - is reached. Of crucial importance is the growth and division of individual cells, happening multiple times, successively increasing both cell number and density. How this can be included in a Multi-Phasefield model was investigated by Harish P Jain during his time as student researcher at the Institute of Scientific Computing, which led to the writing of his master thesis [Jai21] and a joint publication [JWV21].
The approach is, for the sake of simplicity, based on the random model used throughout this thesis. The evolution equation for each Phasefield ϕ_i is, in strong resemblance of (5.2), given by

$$\partial_t \phi_i + v_0 \left(\mathbf{v}_i^{ran} \cdot \nabla \phi_i\right) = M\Delta \frac{\delta \mathcal{E}}{\delta \phi_i} + k_i(\phi_i + 1) \tag{7.1}$$

where $\mathbf{v}_i^{ran}$ is the usual advection vector following the random walk and

$$\mathcal{E} = \frac{1}{Ca}\mathcal{E}_{DCH}\{\phi_i\}) + \frac{1}{In}\mathcal{E}^{\phi}_{INT}\{\phi_i\}) + \frac{1}{Con}\mathcal{E}^{\phi}_{CON}\{\phi_i\})$$

with $\mathcal{E}_{DCH}$ a degenerate Cahn-Hilliard energy resulting from (3.5) by adding a stabilizing degeneracy according to [SVW20], $\mathcal{E}^{\phi}_{INT}$ the quantitative Phasefield-based interaction defined in (3.14) and $\mathcal{E}^{\phi}_{CON}$ the confinement energy given in (3.30). For the interaction now the quantitative Phasefield-based approach introduced in 3.3.3 is used, with the parameter $a = 1.5$ in the interaction potential chosen such that adhesive forces are included.
The most striking difference, compared to the random model used before is, however, given by the reactive term $k_i(\phi_i + 1)$, actively adding cellular mass to each Phasefield. The growth factor k_i is chosen according to a normal distribution

$$k_i \sim \mathcal{N}(r_g f_i \eta_i, r_g f_i \eta_i)$$

where r_g is constant. The inhibition factors $f_i \in [0, 1]$ and $\xi_i \in [0, 1]$ are introduced to inhibit contact with other cells or the confinement. This limits cell growth to regions of free space, which is a well-known phenomenon, usually called *contact inhibition of proliferation*, see [Abe70] for details.
In order to reproduce the behavior of real tissue better, it is not sufficient to include

only growth, but a mechanism for cell division is also required. This is, however, a highly complex mechanism which requires several simplification steps. For example, we have used the axis of contraction for the division, as indicated in [Wya+15]. In terms of the numerical treatment with the Multi-Phasefield model, an additional difficulty is given by the changing number of equations after a new cell was created. The process is summarized by the following steps:

1. Consider a Multi-Phasefield $\{\phi_i\}_{i=1}^N$ and assume ϕ_i crosses a certain volume threshold $V_{max} > 0$

2. Compute the axis of contraction, given by the eigenvector η_i^-, corresponding with the negative eigenvalue, of the elongation tensor $\mathbf{S}_i$ introduced in (3.19). Divide ϕ_i into two equal sized daughter Phasefields ϕ_{d1}, ϕ_{d2}, separated by η_i^-.

3. Replace $\phi_i := \phi_{d1}$ and assign a new variable $\phi_{N+1} := \phi_{d2}$.

In practical, we have found that it is recommended to remove some material close to the cutting edge, in order to have large enough distances between the two daughter cells. Furthermore, due to the parallelization approach similar to the one presented in Subsection 3.6.1, computational resources have to be reserved for possible cell division events and thus a sophisticated system of assigning new Phasefields to CPU cores is required. We will not go into any details here and simply refer to the work in [Jai21].

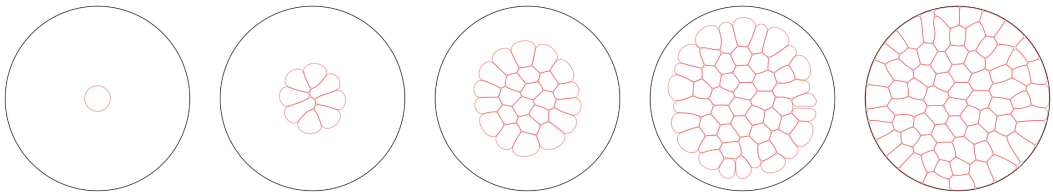

FIGURE 7.1: Visualization of a growing cell colony in the Multi-Phasefield description. From left to right (increasing time) the number of cells and as a consequence the size of the tissue grows. Taken and adapted from [Jai21].

In Figure 7.1 a typical evolution of the tissue in round confinement is shown. Starting with a single cell, a series of multiple divisions leads to an eventual space filling of the whole confinement area.
In [Jai21], many interesting features were observed. T1 transitions and rosettes occur naturally, similar to the previous simulations in confluent setups. The influence of both activity and inhibition strength on the colony growth was investigated, indicating in general a linear growth of the colony radius over time. Furthermore, the probability distribution of the coordination number has revealed similar results to the studies on confined systems in Section 5.5 and the emergence of a confluent state can be observed, as initially high velocities converge towards a fixed, parameter-independent value as the density increases.
The possibility to include cellular growth - and shrinkage / apoptosis which can be modeled in the same way - in Multi-Phasefield models offers the possibility to represent a much wider range of phenomena, for example the evolution of the tissue towards the confluent state. Furthermore, it underlines the huge flexibility of the general modeling approach, as these features can be added or removed on request.

7.2.2 | CELLULAR STRUCTURES ON CURVED MANIFOLDS

Biological tissue, even though many important structures like epithelium are comparably thin, is in general three-dimensional and every $2D$ method is just an approximation to the real geometry. One of the goals in future modeling of cellular structures, is the extension towards full $3D$ descriptions, usually limited by computational resources.
A first step in this direction, is to generalize the computational domain from flat geometries towards curved $2D$ manifolds $\Gamma \subset \mathbb{R}^3$. This case of semi-threedimensional cellular structures plays crucial role during a variety of morphogenetic processes, as reported for example in [Dav12] and [KS11b]. The extension of Multi-Phasefield models towards curved surfaces was performed by Lea Happel during her time as student researcher at the Institute of Scientific Computing and is explained in detail in her master thesis [Hap21].
The generalization of partial differential equations to curved surfaces features different mathematical and numerical challenges. To keep things simple, we have started with the random model, effectively circumventing vector- and tensor-valued differential equations, as required for the intracellular dynamics in the polar or nematic model. The evolution equation for ϕ_i is given by

$$\partial_t \phi_i + v_0 \left(\mathbf{v}_i^{ran,\Gamma} \cdot \nabla_\Gamma \phi_i \right) = M \Delta_\Gamma \frac{\delta \mathcal{E}}{\delta \phi_i} \tag{7.2}$$

with surface gradient ∇_Γ and surface Laplacian Δ_Γ. Note that, in the case of scalar-valued functions, no distinction between the different surface differential operators is required. The energy of the system is given by

$$\mathcal{E} = \frac{1}{Ca} \mathcal{E}_{DCH,\Gamma}\{\phi_i\}) + \frac{1}{In} \mathcal{E}^{\phi}_{INT,\Gamma}\{\phi_i\})$$

with $\mathcal{E}_{DCH,\Gamma}$ a degenerate Cahn-Hilliard energy resulting from (3.5) by including the stabilization proposed in [SVW20] and $\mathcal{E}^{\phi}_{INT,\Gamma}$ the quantitative Phasefield-based interaction defined in (3.14), where have introduced the additional subscript Γ to underline that the computational domain is the manifold Γ.
The definition of the advection vector $\mathbf{v}_i^{ran,\Gamma}$ is slightly more complicated, compared to flat structures. $\mathbf{v}_i^{ran,\Gamma}$ should be chosen in the tangent plane of the computational domain, which could be realized by simply choosing a random vector in $\mathbb{R}^3$ and projecting afterwards. This does, however, cause different numerical problems, especially if the random vector is (almost) normal and thus the projection would have magnitude close to 0. We have introduced the more sophisticated approach

$$\left[\mathbf{v}_i^{ran,\Gamma}\right]_{new} = \cos\alpha \left[\mathbf{v}_i^{ran,\Gamma}\right]_{old} + \sin\alpha \mathbf{b}$$

with $\alpha \sim \eta \mathcal{N}(0,1)$ and $\mathbf{b}$ chosen such that

$$\left\{ \left[\mathbf{v}_i^{ran,\Gamma}\right]_{old}, \mathbf{b} \right\}$$

forms an orthonormal basis of the tangent plane. This differs from typical definitions of a random walk but ensures sufficiently small changes in each timestep, independent of changing tangent spaces.
All studies in [Hap21] are performed for the surface of the sphere, i.e. a closed surface with constant positive curvature. A Surface Finite Element Method is used with

an explicit surface grid. The parallelization approach is very similar to the one introduced in Subsection 3.6.1. For the initialization a dense packing, similar to the one for circular confinements introduced in Subsection 3.6.2, was developed.

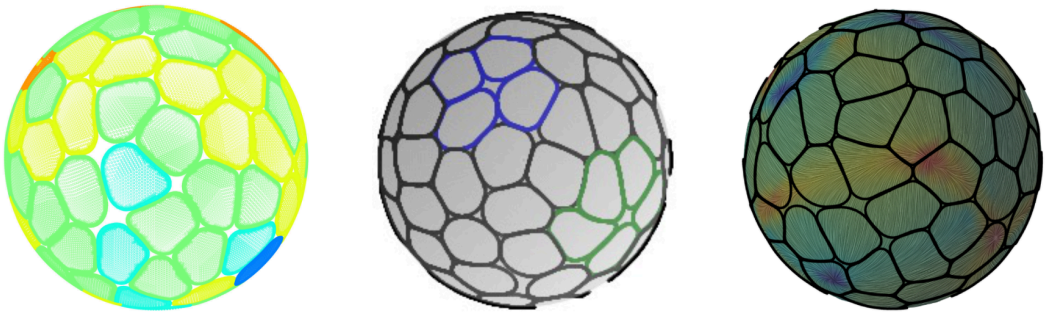

FIGURE 7.2: Visualization of Multi-Phasefield model on the sphere surface. Shown are the $\phi_i = 0$ contours with (Left) color according to coordination number, (Middle) rosettes with 4/5 cells highlighted with blue/green color and (Right) LIC visualization of tissue velocity with color according to vorticity. Taken and adapted from [Hap21].

One important aspect of the study is inspired by the visualization in Figure 7.2 (Left), regarding the coordination number probability that we have studied extensively in Section 5.2. Depending on the number of cells, the energetically optimal packing - closely related to the solution of the Thomson problem - includes different numbers of neighboring cells. Furthermore, it was studied how the occurrence of rosettes depends on the level of activity and the chosen interaction potential - purely repulsive or also adhesive, represented by the choice of the parameter a in the definition of the interaction energy $\mathcal{E}^{\phi}_{INT,\Gamma}$. Additionally, the flow behavior was investigated similar to Section 5.4, identifying vortices in the tissue velocity field.
The generalization of the Multi-Phasefield model towards curved surfaces marks an important first step towards more complex computational domains, even closer to biological systems. Furthermore, it emphasizes the versatility of the model, capable of including significant generalizations with just minor adaptions.

7.3 | OUTLOOK

Even though this thesis was devoted to a detailed investigation of Multi-Phasefield models for cellular structures, many aspects are still open.
For the future research, a very important goal would be to fit the model parameters more closely to experimental data for living tissue, in order to make the model more easily usable in applications. This is not trivial and requires a set of observables that can be handled for both experimental systems and simulation results, like that standard deviation of the coordination number distribution used to create equivalent setups for all four models in Subsection 5.3.2.
Furthermore, it would be interesting to include the topological defects, observed in the nematic alignment in Chapter 6, as contributions to the evolution of the system. One example would be to force apoptosis in the vicinity of $+\frac{1}{2}$ defects, as indicated by the findings in [Saw+17]. Also the strain rate patterns observed in Section 6.4 could contribute to a deformation of the surface, using the generalized geometry setting introduced in Subsection 7.2.2.

The occurrence of multicellular rosettes was observed for both the flat geometry and the curved surfaces, but has not been included in the dynamics of the tissue evolution. They have, however, been observed to play a crucial role in organogenesis, for example in the Drosophila eye development as investigated in [EBF07] and could thus be coupled more closely into the system dynamics, for example to deform the geometry of the domain.
In general, the extension of the models to more complex domains, either deformable manifolds or possibly also three-dimensional geometries, is desirable. In order to describe the early stage developmental processes like organogenesis in a variety of organisms, it is required for cells to form complex $3D$ structures, which can not be captured with the current state of the models.
Due to the high level of flexibility that the Multi-Phasefield approach provides, highlighted for example by the extensions in Section 7.2, it offers incredible potential as an important tool in the future of biomathematical modeling. The field of research and in particular this type of model is still in the earliest stages, yet still observably powerful and so it may one day give even more significant contributions on the way to understanding life.

BIBLIOGRAPHY

[Abe70] M. ABERCROMBIE. Contact inhibition in tissue culture. In: *In Vitro* 6.2 (1970), 128–142.

[Abo70] D. A. ABOAV. The arrangment of grains in a polycrystal. In: *Metallography* 3 (1970), pp. 383–390.

[ACR07] A. R. A. ANDERSON, M. R. A. CHAPLAIN, and K. A. REJNIAK. Single-Cell-Based Models in Biology and Medicine. In: *Mathematical Medicine and Biology - a Journal of The Ima* 25 (2007), pp. 185–186.

[AE07] R. ANANTHAKRISHNAN and A. EHRLICHER. The Forces Behind Cell Movement. In: *International Journal of Biological Sciences* 3 (2007), pp. 303 –317.

[AGS17] S. ALT, P. GANGULY, and G. SALBREUX. Vertex models: from cell mechanics to tissue morphogenesis. In: *Philosophical Transactions of the Royal Society B: Biological Sciences* 372 (2017).

[Aig+10] B. AIGOUY et al. Cell Flow Reorients the Axis of Planar Polarity in the Wing Epithelium of Drosophila. In: *Cell* 142 (2010), pp. 773–786.

[AMR88] R. ABRAHAM, J. E. MARSDEN, and R. RATIU. *Manifolds, Tensor Analysis, and Applications: 2nd Edition*. Berlin, Heidelberg: Springer-Verlag, 1988. ISBN: 0387967907.

[APV16] F. ALAIMO, S. PRAETORIUS, and A. VOIGT. A microscopic field theoretical approach for active systems. In: *New Journal of Physics* 18.8 (2016), p. 83008.

[Asi+03] M. ASIPAUSKAS et al. A texture tensor to quantify deformations: the example of two-dimensional flowing foams. In: *Granular Matter* 5 (2003), pp. 71–74.

[Ati+18] L. ATIA et al. Geometric constraints during epithelial jamming. In: *Nature Physics* 14 (2018), pp. 613 –620.

[Bal+21] L. BALASUBRAMANIAM et al. Investigating the nature of active forces in tissues reveals how contractile cells can form extensile monolayers. In: *Nature Materials* (2021), pp. 1 –11.

[Ban+21] S. BANAVAR et al. Mechanical control of tissue shape and morphogenetic flows during vertebrate body axis elongation. In: *Scientific Reports* 11 (2021).

[Bas+11] M. BASAN et al. Dissipative particle dynamics simulations for biological tissues: rheology and competition. In: *Physical Biology* 8 (2011).

[Bea93] E. L. BEARER. Role of actin polymerization in cell locomotion: molecules and models. In: *American journal of respiratory cell and molecular biology* 8 (1993), pp. 582–582.

[Bel+07] J. B. BELTMAN et al. Lymph node topology dictates T cell migration behavior. In: *Journal of Experimental Medicine* 204.4 (2007), pp. 771–780.

[Bi+14] D. BI et al. Energy barriers and cell migration in densely packed tissues. In: *Soft Matter* 10 12 (2014), pp. 1885–90.

[Bi+15] D. BI et al. A density-independent rigidity transition in biological tissues. In: *Nature Physics* 11 (2015), pp. 1074–1079.

[Bi+16] D. BI et al. Motility-driven glass and jamming transitions in biological tissues. In: *Physical Review X* 6 2 (2016).

[Bie+16] C. BIELMEIER et al. Interface Contractility between Differently Fated Cells Drives Cell Elimination and Cyst Formation. In: *Current Biology* 26 (2016), pp. 563 –574.

[BK13] L. BERTHIER and J. KURCHAN. Non-equilibrium glass transitions in driven and active matter. In: *Nature Physics* 9 (2013), pp. 310–314.

[Bla+06] J. T. BLANKENSHIP et al. Multicellular rosette formation links planar cell polarity to tissue morphogenesis. In: *Developmental Cell* 11 4 (2006), pp. 459–470.

[BM+18] C. BLANCH-MERCADER et al. Turbulent dynamics of epithelial cell cultures. In: *Physical Review Letters* 120 (2018), p. 208101.

[Bod+20] D. BODOR et al. Of Cell Shapes and Motion: The Physical Basis of Animal Cell Migration. In: *Developmental Cell* 52 5 (2020), pp. 550–562.

[BSD07] M. BLOCK, E. SCHÖLL, and D. DRASDO. Classifying the expansion kinetics and critical surface dynamics of growing cell populations. In: *Physical Review Letters* 99 (2007).

[BT09] L. BERTHIER and G. TARJUS. Nonperturbative effect of attractive forces in viscous liquids. In: *Physical Review Letters* 103 (2009), p. 170601.

[Cam+14] B. A. CAMLEY et al. Polarity mechanisms such as contact inhibition of locomotion regulate persistent rotational motion of mammalian cells on micropatterns. In: *Proceedings of the National Academy of Sciences* 111 (2014), pp. 14770–14775.

[CC92] G. CAGINALP and Xinfu CHEN. "Phase field equations in the singular limit of sharp interface problems". In: *On the Evolution of Phase Boundaries*. Springer New York, 1992, pp. 1–27.

[CH58] J. W. CAHN and J. E. HILLIARD. Free Energy of a Nonuniform System. I. Interfacial Free Energy. In: *The Journal of Chemical Physics* 28.2 (1958), pp. 258–267.

[CH89] R. COURANT and D. HILBERT. *Methods of Mathematical Physics*. Vol. 1. New York: Wiley, 1989.

[Cha92] S. CHANDRASEKHAR. *Liquid Crystals*. 2nd ed. Cambridge University Press, 1992.

[Che+14] N. CHENOUARD et al. Objective comparison of particle tracking methods. In: *Nature Methods* 11 (2014), pp. 281–290.

[Chi95] S. N. CHIU. Aboav-Weaire's and Lewis' laws - review. In: 34 (1995), pp. 149–165.

[Dav12] L. DAVIDSON. Epithelial machines that shape the embryo. In: *Trends in Cell Biology* 22 2 (2012), pp. 82–7.

[DBV11] J. DUPLAT, B. BOSSA, and E. VILLERMAUX. On two-dimensional foam aging. In: *Journal of Fluid Mechanics* 673 (2011), pp. 147–179.

[DD05] A. DEUTSCH and S. DORMANN. "Cellular Automaton Modeling of Biological Pattern Formation - Characterization, Applications, and Analysis". In: *Modeling and simulation in science, engineering and technology*. 2005.

[DDBW12] S. DOUEZAN, J. DUMOND, and F. BROCHARD-WYART. Wetting transitions of cellular aggregates induced by substrate rigidity. In: *Soft Matter* 8 (2012), pp. 4578–4583.

[DDL01] S. DORMANN, A. DEUTSCH, and A. LAWNICZAK. Fourier analysis of Turing-like pattern formation in cellular automaton models. In: *Future Generation Computer Systems* 17 (2001), pp. 901–909.

[DeC+15] S. J. DECAMP et al. Orientational order of motile defects in active nematics. In: *Nature Materials* 14.11 (2015), pp. 1110–1115.

[Def+14] M. DEFORET et al. Emergence of collective modes and tri-dimensional structures from epithelial confinement. In: *Nature Communications* 5 (2014), 3747.

[Del+18] D. DELL'ARCIPRETE et al. A growing bacterial colony in two dimensions as an active nematic. In: *Nature Communications* 9 (2018).

[Del95] T. DELMARCELLE. "The Visualization of Second-Order Tensor Fields". PhD Thesis. Stanford University, 1995.

[DH05] D. DRASDO and S. HÖHME. A single-cell-based model of tumor growth in vitro: monolayers and spheroids. In: *Physical Biology* 2 (2005).

[DH94] T. DELMARCELLE and L. HESSELINK. "The topology of symmetric, second-order tensor fields". In: *Proceedings Visualization '94*. 1994, pp. 140–147.

[Doo+18] A. DOOSTMOHAMMADI et al. Active nematics. In: *Nature Communications* 9 (2018), p. 3246.

[Dox+13] K. DOXZEN et al. Guidance of collective cell migration by substrate geometry. In: *Integrative Biology* 5 8 (2013), pp. 1026–35.

[Duc+17] G. DUCLOS et al. Topological defects in confined populations of spindle-shaped cells. In: *Nature Physics* 13 (2017), pp. 58–62.

[EBF07] L. M. ESCUDERO, M. BISCHOFF, and M. FREEMAN. Myosin II regulates complex cellular arrangement and epithelial architecture in Drosophila. In: *Developmental Cell* 13.5 (2007), 717—729.

[EM13] S. ETIENNE-MANNEVILLE. Microtubules in cell migration. In: *Annual Review of Cell and Developmental Biology* 29 (2013).

[Esc+11] L. M. ESCUDERO et al. Epithelial organisation revealed by a network of cellular contacts. In: *Nature Communications* 2 (2011), pp. 526 –526.

[ET+18] G. ERDEMCI-TANDOGAN et al. Tissue Flow Induces Cell Shape Changes During Organogenesis. In: *Biophysical Journal* 115 11 (2018), pp. 2259–2270.

[Far+07] R. FARHADIFAR et al. The Influence of Cell Mechanics, Cell-Cell Interactions, and Proliferation on Epithelial Packing. In: *Current Biology* 17 (2007), pp. 2095–2104.

[FG09] P. FRIEDL and D. GILMOUR. Collective cell migration in morphogenesis, regeneration and cancer. In: *Nature Reviews Molecular Cell Biology* 10 (2009), 445–457.

[FHP86] U. FRISCH, B. HASSLACHER, and Y. POMEAU. Lattice-gas automata for the Navier-Stokes equation. In: *Physical Review Letters* 56 14 (1986), pp. 1505–1508.

[FKF93] R. FURUKAWA, R. KUNDRA, and M. FECHHEIMER. Formation of liquid crystals from actin filaments. In: *Biochemistry* 32 46 (1993), pp. 12346–52.

[Fle+14] A. FLETCHER et al. Vertex models of epithelial morphogenesis. In: *Biophysical Journal* 106 11 (2014), pp. 2291–2304.

[Fly93] H. FLYVBJERG. Model for coarsening froths and foams. In: *Physical Review E* 47 (1993), pp. 4037–4054.

[FRA07] R. FARHADIFAR, J.-C. RÖPER, and S .and Jülicher F. AIGOUY B .and Eaton. The influence of cell mechanics, cell-cell interactions, and proliferation on epithelial packing. In: *Current Biology* 17 (2007), pp. 2095–2104.

[GD14] L. GIOMI and A. DESIMONE. Spontaneous division and motility in active nematic droplets. In: *Physical Review Letters* 112 14 (2014), p. 147802.

[GG92] F. GRANER and J. A. GLAZIER. Simulation of biological cell sorting using a two-dimensional extended Potts model. In: *Physical Review Letters* 69 13 (1992), pp. 2013–2016.

[Gia+18] F. GIAVAZZI et al. Flocking transitions in confluent tissues. In: *Soft Matter* 14 18 (2018), pp. 3471–3477.

[GKY92] C. GODRECHE, I. KOSTOV, and I. YEKUTIELI. Topological correlations in cellular structures and planar graph theory. In: *Physical Review Letters* 69 (1992), pp. 2674–2677.

[GL17] Tong GAO and Zhaorui LI. Self-Driven Droplet Powered By Active Nematics. In: *Physical Review Letters* 119 10 (2017).

[GLD05] J. GALLE, M. LOEFFLER, and D. DRASDO. Modeling the effect of deregulated proliferation and apoptosis on the growth dynamics of epithelial cell populations in vitro. In: *Biophysical Journal* 88 1 (2005), pp. 62–75.

[GP93] P. G. DE GENNES and J. PROST. *The Physics of Liquid Crystals*. International Series of Monographs on Physics. Clarendon Press, 1993.

[GS19] Clare L. GARCIN and A. STRAUBE. Microtubules in cell migration. In: *Essays in Biochemistry* 63 (2019), pp. 509 –520.

[Hap21] L. HAPPEL. "Multi Phase Field Models for Cellular Structures on the Sphere". Masters Thesis. Technische Universität Dresden, 2021.

[Hav+09] D. HAVA et al. Apical membrane maturation and cellular rosette formation during morphogenesis of the zebrafish lateral line. In: *Journal of Cell Science* 122 (2009), 687–695.

[HG06] P. HAAS and D. GILMOUR. Chemokine signaling mediates self-organizing tissue migration in the zebrafish lateral line. In: *Developmental Cell* 10.5 (2006).

[HMN14] M. J. HARDING, H. F. MCGRAW, and A. NECHIPORUK. The roles and regulation of multicellular rosette structures during morphogenesis. In: *Development* 141 (2014), pp. 2549–2558.

[HN12] M. J. HARDING and A. V. NECHIPORUK. Fgfr-Ras-MAPK signaling is required for apical constriction via apical positioning of Rho-associated kinase during mechanosensory organ formation. In: *Development* 139.17 (2012), pp. 3130–3135.

[HS17] V. HAKIM and P. SILBERZAN. Collective cell migration: a physics perspective. In: *Reports on Progress in Physics* 80 (2017), 076601.

[IS13] D. IQBAL and M. SAMIULLAH. Photo-Responsive Shape-Memory and Shape-Changing Liquid-Crystal Polymer Networks. In: *Materials* 6 (2013), pp. 116 –142.

[Jai21] H. P JAIN. "Phase Field Modelling of Active Interacting Cells that Grow and Divide". Masters Thesis. Technische Universität Dresden, 2021.

[JB02] B. JEUNE and D. BARABÉ. The Use of the Aboav-Weaire Law to Estimate a Biological Constraint. In: *Journal of Biological Systems* 10 (2002), pp. 33–45.

[Jon24] J. E. JONES. On the determination of molecular fields. —II. From the equation of state of a gas. In: *Proceedings of the Royal Society of London A: Mathematical, Physical and Engineering Sciences* 106.738 (1924), pp. 463–477.

[JWV21] H. P JAIN, D. WENZEL, and A. VOIGT. *The impact of contact inhibition on collective cell migration and proliferation*. 2021. arXiv: 2108.04743.

[Kal18] S. KALIMAN. "Morphological analysis of epithelial cells". PhD Thesis. Friedrich-Alexander-Universität Erlangen-Nürnberg (FAU), 2018.

[Kar+12] J. R. KARR et al. A Whole-Cell Computational Model Predicts Phenotype from Genotype. In: *Cell* 150 (2012), pp. 389–401.

[KJ00] K. KRUSE and F. JÜLICHER. Actively contracting bundles of polar filaments. In: *Physical Review Letters* 85.8 (2000), pp. 1778–1781.

[KKS17] K. KAWAGUCHI, R. KAGEYAMA, and M. SANO. Topological defects control collective dynamics in neural progenitor cell cultures. In: *Nature* 545 (2017), pp. 327–331.

[Kok+19] M. KOKIC et al. Minimisation of surface energy drives apical epithelial organisation and gives rise to Lewis' law. In: *bioRxiv* (2019).

[KP61] F. E. KARASZ and J. POPLE. A theory of fusion of molecular crystals—II: Phase diagrams and relations with solid state transitions. In: *Journal of Physics and Chemistry of Solids* 20 (1961), pp. 294–306.

[Kra20] M. KRAJNC. Solid-fluid transition and cell sorting in epithelia with junctional tension fluctuations. In: *Soft Matter* (2020).

[Kru+04] K. KRUSE et al. Asters, vortices, and rotating spirals in active gels of polar filaments. In: *Physical Review Letters* 92 (2004), p. 78101.

[KS11a] I. KAVERINA and A. STRAUBE. Regulation of cell migration by dynamic microtubules. In: *Seminars in Cell & Developmental Biology* 22 9 (2011), pp. 968–74.

[KS11b] R. KELLER and D. SHOOK. The bending of cell sheets - from folding to rolling. In: *BMC Biology* 9 (2011), pp. 90 –90.

[KV21] V. KRAUSE and A. VOIGT. *Deformable active nematic particles and emerging edge currents in circular confinements*. 2021. arXiv: 2102.02108.

[Lew28] F. T. LEWIS. The correlation between cell division and the shapes and sizes of prismatic cells in the epidermis of cucumis. In: *The Anatomical Record* 38 (1928), pp. 341–376.

[Lie+15] P. V. LIEDEKERKE et al. Simulating tissue mechanics with agent-based models: concepts, perspectives and some novel results. In: *Computational Particle Mechanics* 2 (2015), pp. 401–444.

[LK11] Yibao LI and Junseok KIM. Multiphase image segmentation using a phase-field model. In: *Computers & Mathematics with Applications* 62 (2011), pp. 737–745.

[LM17] B. LADOUX and R. MÈGE. Mechanobiology of collective cell behaviours. In: *Nature Reviews Molecular Cell Biology* 18 (2017), pp. 743–757.

[LN98] A. J. LIU and S. NAGEL. Nonlinear dynamics: Jamming is not just cool any more. In: *Nature* 396 (1998), pp. 21–22.

[Loe+20] B. LOEWE et al. Solid-Liquid Transition of Deformable and Overlapping Active Particles. In: *Physical Review Letters* 125 3 (2020).

[LZA15a] J. LÖBER, F. ZIEBERT, and I. ARANSON. Collisions of deformable cells lead to collective migration. In: *Scientific Reports* 5 (2015), p. 9172.

[LZA15b] J. LOEBER, F. ZIEBERT, and I. S. ARANSON. Collisions of deformable cells lead to collective migration. In: *Scientific Reports* 5 (2015), p. 9172.

[MAL19] K. A. MOATS, E. ASADI, and M. LARADJI. Phase field crystal simulations of the kinetics of Ostwald ripening in two dimensions. In: *Physical Review E* (2019), p. 012803.

[MDS12] E. MEIJERING, O. DZYUBACHYK, and I. SMAL. "Methods for cell and particle tracking". In: *Imaging and spectroscopic analysis of living cells: Optical and specrroscopic techniques*. Ed. by CONN, P.M. Vol. 504. Methods in Enzymology. 2012, pp. 183–200.

[MK09] A. MOGILNER and K. KEREN. The Shape of Motile Cells. In: *Current Biology* 19 (2009), R762–R771.

[MO96] A. MOGILNER and G. OSTER. Cell motility driven by actin polymerization. In: *Biophysical Journal* 71 6 (1996).

[Mon+18] A. MONGERA et al. A fluid-to-solid jamming transition underlies vertebrate body axis elongation. In: *Nature* 561 (2018), pp. 401 –405.

[MPV15] W. MARTH, S. PRAETORIUS, and A. VOIGT. A mechanism for cell motility by active polar gels. In: *Journal of The Royal Society Interface* 12 (2015), p. 20150161.

[MV14a] W. MARTH and A. VOIGT. Signaling networks and cell motility: a computational approach using a phase field description. In: *Journal of Mathematical Biology* 69 (2014), pp. 91–112.

[MV14b] E. MÉHES and T. VICSEK. Collective motion of cells: from experiments to models. In: *Integrative Biology* 6.9 (July 2014), pp. 831–854.

[MV16] W. MARTH and A. VOIGT. Collective migration under hydrodynamic interactions: a computational approach. In: *Interface Focus* 6 (2016).

[MVD90] J. C. M. MOMBACH, M. VASCONCELLOS, and R. M. C. DEALMEIDA. Arrangment of cells in vegetable tissues. In: *Journal of Physics D: Applied Physics* 23 (1990), pp. 600–606.

[MYD19] R MUELLER, J M YEOMANS, and A DOOSTMOHAMMADI. Emergence of active nematic behavior in monolayers of isotropic cells. In: *Physical Review Letters* 122 (2019), p. 48004.

[NH01] T. NAGAI and H. HONDA. A dynamic cell model for the formation of epithelial tissues. In: *Philosophical Magazine B* 81 (2001), pp. 699 –719.

[NH09] T. NAGAI and H. HONDA. Computer simulation of wound closure in epithelial tissues: cell-basal-lamina adhesion. In: *Physical Review E* 80(6 Pt 1) (2009).

[Non12] M. NONOMURA. Study on multicellular systems using a phase field model. In: *PLoS ONE* 7 (2012), e33501.

[OD16] A. U. OZA and J. DUNKEL. Antipolar ordering of topological defects in active liquid crystals. In: *New Journal of Physics* 18.9 (2016), p. 93006.

[Osw+17] L. OSWALD et al. Jamming transitions in cancer. In: *Journal of physics D: Applied Physics* 50 (2017).

[Pal+15] B. PALMIRI et al. Multiple scale model for cell migration in monolayers: Elastic mismatch between cells enhances motility. In: *Scientific Reports* 5 (2015), p. 11745.

[Par+15] J.-A. PARK et al. Unjamming and cell shape in the asthmatic airway epithelium. In: *Nature Materials* 14 10 (2015), pp. 1040–8.

[Pet+10] L. PETITJEAN et al. Velocity fields in a collectively migrating epithelium. In: *Biophysical Journal* 98 9 (2010), pp. 1790–1800.

[Pey+19] G. PEYRET et al. Sustained oscillations of epithelial cell sheets. In: *Biophysical Journal* 117 (2019), pp. 464–478.

[Pou+07] M. POUJADE et al. Collective migration of an epithelial monolayer in response to a model wound. In: *Proceedings of the National Academy of Sciences* 104.41 (2007), pp. 15988–15993.

[Pra+] S. PRAETORIUS et al. *AMDiS*. URL: `https://gitlab.mn.tu-dresden.de/iwr/amdis`. (accessed: 01.07.2021).

[PSR91] M. A. PESHKIN, K. J. STRANDBURG, and N. RVIER. Entropic predictions for cellular networks. In: *Physical Review Letters* 67 (1991), pp. 1803–1806.

[PV18] S. PRAETORIUS and A. VOIGT. "Collective cell behavior - a cell-based parallelization approach for a phase field active polar gel model". In: *NIC Symposium 2018*. Ed. by K. BINDER, M. MÜLLER, and A. TRAUTMANN. 2018, pp. 369–376.

[Rad+09] M. RADSZUWEIT et al. Comparing the growth kinetics of cell populations in two and three dimensions. In: *Physical Review E* 79 (2009).

[Rob+12] F. ROBERTSON et al. Atonal and EGFR signalling orchestrate rok- and Drak-dependent adherens junction remodelling during ommatidia morphogenesis. In: *Development* 139.18 (2012), 3432—3441.

[Ror09] P. RORTH. Collective cell migration. In: *Annual Review of Cell and Developmental Biology* 25 (2009), 407–429.

[Rup+17] J.-F. RUPPRECHT et al. Geometric constraints alter cell arrangements within curved epithelial tissues. In: *Molecular Biology of the Cell* 28.25 (2017), 3582–3594.

[San+12] T. SANCHEZ et al. Spontaneous motion in hierarchically assembled active matter. In: *Nature* 491 (2012), pp. 431–434.

[Sat+10] Y. SATO et al. Dynamic Analysis of Vascular Morphogenesis Using Transgenic Quail Embryos. In: *PLoS ONE* 5.9 (2010).

[Saw+17] T. B. SAW et al. Topological defects in epithelia govern cell death and extrusion. In: *Nature* 544 (2017), pp. 212–216.

[Sch+12] J. E. SCHINDELIN et al. Fiji: an open-source platform for biological-image analysis. In: *Nature Methods* 9 (2012), pp. 676–682.

[Sep+13] N. SEPÚLVEDA et al. Collective Cell Motion in an Epithelial Sheet Can Be Quantitatively Described by a Stochastic Interacting Particle Model. In: *PLoS Computational Biology* 9 (2013).

[Set96] J. A. SETHIAN. A fast marching level set method for monotonically advancing fronts. In: *Proceedings of the National Academy of Sciences* 93.4 (1996), pp. 1591–1595.

[SG+16] D. SÁNCHEZ-GUTIÉRREZ et al. Fundamental physical cellular constraints drive self-organization of tissues. In: *The EMBO Journal* 35 (2016), pp. 77–88.

[SK05] I. F. SBALZARINI and P. KOUMOUTSAKOS. Feature point tracking and trajectory analysis for video imaging in cell biology. In: *Journal of Structural Biology* 151 (2005), 182–195.

[SM16] E. SCARPA and R. MAYOR. Collective cell migration in development. In: *Journal of Cell Biology* 212 (2016), 143–155.

[SMS94] M. SEUL, N. Y. MORGAN, and C. SIRE. Domain coarsening in a two-dimensional binary mixture: growth dynamics and spatial correlations. In: *Physical Review Letters* 73 (1994), pp. 2284–2287.

[SN59] S. SAITŌ and T. NAKAJIMA. Glass transition in polymers. In: *Journal of Applied Polymer Science* 2 (1959), pp. 93–99.

[Spe+14] T SPECK et al. Effective Cahn-Hilliard equation for the phase separation of active Brownian particles. In: *Physical Review Letters* 112 (2014), p. 218304.

[SS02] U. SCHWARZ and S. SAFRAN. Elastic interactions of cells. In: *Physical Review Letters* 88 4 (2002), p. 048102.

[SS95] C. SIRE and M. SEUL. Maximum entropy analysis of disordered droplet patterns. In: 5 (1995), pp. 97–109.

[Sta+10] D. STAPLE et al. Mechanics and remodelling of cell packings in epithelia. In: *The European Physical Journal E* 33 (2010), pp. 117–127.

[Ste62] M. S. STEINBERG. On the mechanism of tissue reconstruction by dissociated cells. I. Population kinetics, differential adhesiveness. and the absence of directed migration. In: *Proceedings of the National Academy of Sciences of the United States of America* 48 (1962), pp. 1577–82.

[SVW20] M. SALVALAGLIO, A. VOIGT, and S. M. WISE. Doubly degenerate diffuse interface models of surface diffusion. In: *Mathematical Methods in the Applied Sciences* 44.7 (2020), 5385–5405.

[Szi+18] B. SZIGETI et al. A blueprint for human whole-cell modeling. In: *Current Opinion in Systems Biology* 7 (2018), pp. 8–15.

[TMC12] E. TJHUNG, D. MARENDUZZO, and M. CATES. Spontaneous symmetry breaking in active droplets provides a generic route to motility. In: *Proceedings of the National Academy of Sciences* 109 (2012), pp. 12381–12386.

[TT98] J. TONER and Y. TU. Flocks, herds, and schools: A quantitative theory of flocking. In: *Physical Review E* 58.4 (1998), pp. 4828–4858.

[TTR05] J. TONER, Y. TU, and S. RAMASWAMY. Hydrodynamics and phases of flocks. In: *Annals of Physics* 318.1 (2005), pp. 170–244.

[Vet+19] R. VETTER et al. Aboave-Weaire's law in epithelia results from an angle constraint in contiguous polygonal lattices. In: *bioRxiv* (2019).

[Vic+95] T. VICSEK et al. Novel type of phase transition in a system of self-driven particles. In: *Physical Review Letters* 75 6 (1995), pp. 1226–1229.

[Voo85] P. W. VOORHEES. The theory of Ostwald ripening. In: *Journal of Statistical Physics* 38 (1985), pp. 231–252.

[VV07a] S. VEY and A. VOIGT. Adaptive full domain covering meshes for parallel finite element computations. In: *Computing* 81 (2007), pp. 53–75.

[VV07b] S. VEY and A. VOIGT. AMDiS: adaptive multidimensional simulations. In: *Computing and Visualization in Science* 10 (2007), pp. 57–67.

[VW12] A. VOIGT and T. WITKOWSKI. A multi-mesh finite element method for Lagrange elements of arbitrary degree. In: *Journal of Computational Science* 3 (2012), pp. 420–428.

[Wea74] D. WEAIRE. Some remarks on the arrangement of grains in a polycrystal. In: *Metallography* 7 (1974), pp. 157–160.

[Wen+20] D. WENZEL et al. Defects in Active Nematics – Algorithms for Identification and Tracking. In: *Computational Methods in Applied Mathematics* 21 (2020), pp. 683 –692.

[Wit+14] R. WITTKOWSKI et al. Scalar ϕ^4 field theory for active-particle phase separation. In: *Nature Communications* 5 (2014), p. 4351.

[Wit+15] T. WITKOWSKI et al. Software concepts and numerical algorithms for a scalable adaptive parallel finite element method. In: *Advances in Computational Mathematics* 41 (2015), pp. 1145–1177.

[WPV19] D. WENZEL, S. PRAETORIUS, and A. VOIGT. Topological and geometrical quantities in active cellular structures. In: *The Journal of Chemical Physics* 150 (2019), p. 164108.

[WR84] D. WEAIRE and N. RIVIER. Soap, cells and statistics – random patterns in two dimensions. In: *Contemporary Physics* 25 (1984), pp. 59–99.

[WV21] D. WENZEL and A. VOIGT. *Multiphase field models for collective cell migration*. 2021. arXiv: 2106.10552.

[Wya+15] T. WYATT et al. Emergence of homeostatic epithelial packing and stress dissipation through divisions oriented along the long cell axis. In: *Proceedings of the National Academy of Sciences* 112 (2015), pp. 5726 –5731.

[Yan+17] X. YANG et al. Correlating cell shape and cellular stress in motile confluent tissues. In: *Proceedings of the National Academy of Sciences* 114 (2017), pp. 12663 –12668.

[YB18] L. YAN and D. BI. Multicellular Rosettes Drive Fluid-solid Transition in Epithelial Tissues. In: *Physical Review X* 9 (2018), p. 011029.

[YB19] L. YAN and D. BI. Multicellular Rosettes Drive Fluid-solid Transition in Epithelial Tissues. In: *Physical Review X* 9 (2019), 011029.